AARHUS
UNIVERSITY
DEPARTMENT OF PHYSICS AND ASTRONOMY

T. Vibel

Statistical Analysis of Atom Number Fluctuations in Q. Degenerate Bose Gases

PhD Thesis

Statistical Analysis of Atom Number Fluctuations
in Quantum Degenerate Bose Gases

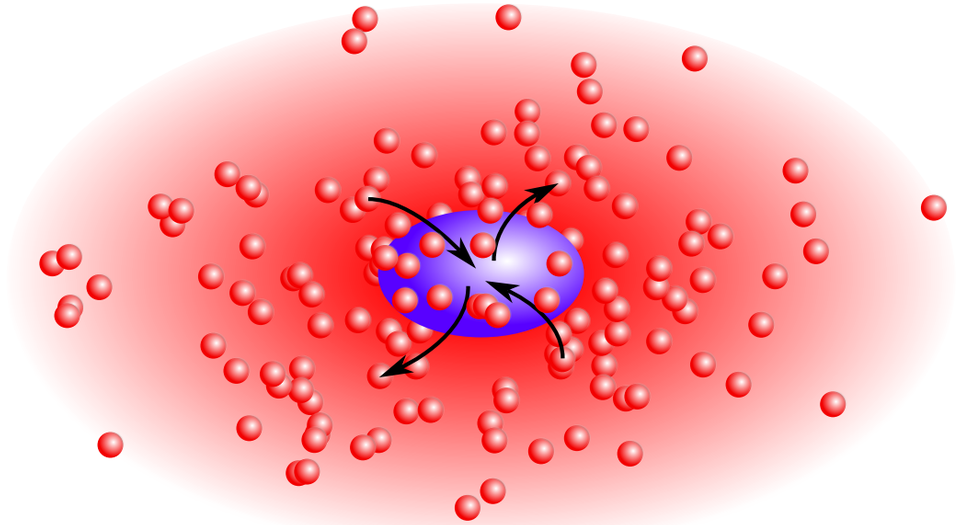

Toke Vibel
PhD Thesis

Statistical Analysis of Atom Number Fluctuations in Quantum Degenerate Bose Gases

Toke Vibel
Department of Physics and Astronomy
Aarhus University, Denmark

PhD thesis
February 2024

Front cover illustration: Conceptual depiction of atom exchange dynamics between the central Bose-Einstein condensate (BEC) and the surrounding thermal cloud in a partially condensed Bose gas, resulting in fluctuations in the BEC atom number.

Abstract

Bose-Einstein condensation (BEC) in dilute gases stands as a fascinating phenomenon of quantum mechanics. In this state, hundreds of thousands of atoms occupy the lowest energy level, establishing a collective macroscopic quantum state, with numerous intriguing properties. BEC has become a fundamental tool for the exploration of quantum physics and it may facilitate further advancements in quantum technology, for instance, in quantum simulation and sensing applications. Due to the potential of BECs in both basic research and technology, a fundamental understanding of this phenomenon is essential to guarantee the precision and reliability of its applications.

Atom number fluctuations in BECs stand as an unresolved fundamental problem that has posed significant theoretical challenges for nearly eight decades. The experimental observation of this effect has recently become feasible. However, a direct comparison between theoretical predictions and experimental results remains outstanding. In particular, technical challenges persist in the accurate detection of the BEC, and a thorough understanding of estimation errors is lacking.

This PhD thesis addresses some of these challenges in the field. Firstly, it introduces an enhanced calibration method for time-of-flight absorption images of ultracold atomic clouds, improving the accuracy of such measurements. Additionally, a thorough statistical analysis of uncertainties in the preparation and parameter estimation of partially condensed Bose gases is presented, leading to an improved understanding of atom number fluctuations in BEC.

Finally, this thesis presents the experimental advances toward a new project within the research group: Electromagnetically induced transparency (EIT). EIT is a concept where an otherwise opaque cloud can be made transparent through manipulation of its quantum states. Notably, these advancements include the construction of setups for an optical dipole trap and a hybrid trap, along with the development of systems enabling precise control of magnetic fields. This laid the groundwork for recent demonstrations of EIT within the group.

Resumé
Danish Abstract

Bose-Einstein kondensation (BEC) i atomare gasser er et fascinerende fænomen inden for kvantemekanikken. I denne tilstand befinder hundredtusinder af atomer sig i det laveste energiniveau og etablerer en kollektiv makroskopisk kvantetilstand med adskillige interessante egenskaber. BEC er blevet et helt grundlæggende redskab til udforskning af kvantefysik og er med til at drive yderligere fremskridt inden for kvanteteknologi, f.eks. inden for kvantesimulering og sensorteknologi. På grund af BEC's potentiale inden for både grundforskning og teknologi er det afgørende med en fundamental forståelse af fænomenet for at sikre præcisionen og pålideligheden af dets anvendelser.

Atomantalsfluktuationer i BEC'er udgør et sådant fundamentalt problem, og har været en stor teoretisk udfordring i næsten otte årtier. Dette er for nyligt blevet bekræftet eksperimentelt, men en direkte sammenligning mellem teoretiske forudsigelser og eksperimentelle resultater er stadig udestående. Desuden er der fortsat tekniske udfordringer med nøjagtig detektion af BEC'er og en grundig forståelse af estimeringsfejl mangler.

Denne ph.d.-afhandling adresserer nogle af disse udfordringer. For det første introducerer den en forbedret kalibreringsmetode til absorptionsafbildning af ultrakolde atomskyer, hvilket forbedrer nøjagtigheden af disse målinger. Derudover præsenteres en grundig statistisk analyse af usikkerheder i produktion af BEC'er samt af estimeringsfejl for delvist kondenserede Bose-gasser: Dette har ført til en forbedret forståelse af atomantalsfluktuationer i BEC'er.

Endelig præsenterer denne afhandling de eksperimentelle fremskridt mod et nyt projekt inden for forskningsgruppen: Elektromagnetisk induceret gennemsigtighed (EIT). EIT er et koncept, hvor en ellers uigennemsigtig sky kan gøres transparent ved manipulation af atomernes kvantetilstande. Disse fremskridt involverer især udviklingen af en opstilling til en optisk dipolfælde og en hybridfælde samt udviklingen af systemer, der muliggør præcis kontrol af magnetfelter. Dette har bidraget til de pågående demonstrationer af EIT inden for gruppen.

Preface

This thesis presents the most significant outcomes of my last 5 years of study. In February 2019, I joined Jan Arlt's Ultracold Quantum Gases Group, specifically the Lattice Lab, following the completion of my bachelor's degree. This opportunity placed me in a 3.5+4.5 scheme. Over the course of my studies, I was fortunate to become a parent twice, with two periods of parental leave extending the duration of my study to five years.

In the beginning, the group comprised Jan Arlt, postdoc Mick Kristensen, and PhD student Mikkel Berg Christensen. The initial focus, up until the onset of and during the first coronavirus lockdown in spring 2020, was primarily on refining an imaging calibration technique [1] and characterizing atom number fluctuations [2].

Following the initiation of the Center for Complex Quantum Systems (CCQ) in the autumn of 2020, the aim of the project was divided in two. Experimentally, we aimed to establish the setup for studying electromagnetically induced transparency (EIT), while simultaneously ensuring that we extracted all essential results from the extensive dataset of fluctuation measurements.

During this period, Claus Normann Madsen joined the lab for a year, after which I continued as the sole PhD student in the lattice lab until the arrival of Laurits Nikolaj Stokholm and Rasmus Malthe Fiil Andersen in 2022. As of autumn 2022, my primary focus shifted towards finalizing the analysis of atom number fluctuations [3], with my role also transitioning toward supporting the two new PhD students in their ongoing path toward EIT.

This project owes its success to the wonderful individuals who have

supported me throughout. I would like to take this opportunity to show my gratitude to several people.

A big thank you goes to my supervisor, Jan Arlt, for guiding and supporting me in my academic journey. I am grateful for your trust in me and the freedom you've granted me in shaping my project. Further, I appreciate that you always keep your door open and are ready for discussion.

A special thanks to Mikkel and Mick for your invaluable mentorship and guidance at the beginning of my PhD. Not only did you teach me how to run the lab, but you've also been exceptional colleagues in every regard.

To the remaining of the original squad — Jens, Carrier, Robert, Otto, Claus, Nils, Magnus, and Thomas — it was a pleasure discussing science, news, and trivial topics with you. You have been fantastic colleagues.

I would also like to thank Maximillian Baron for the brief overlap between your master's project and my PhD (brief due to my first parental leave). I appreciated our personal conversations and also your valuable input on my analysis of atom number fluctuations.

My thank yous also extend to the new MIX team, Søren and Andreas, for engaging in both scientific and non-scientific discussions with me. At present, MIX is for sure performing well, but I remain confident that the Lattice lab[1] will once again become the flagship lab of Jan Arlt's group in the future. ;)

A special thank you to Laurits and Malthe for the close collaboration during the final part of my PhD. It has been truly inspirational to work with you and observe how quickly you became familiar with and were able to run the lab independently. I am confident you now taking the helm, and I look forward to following your research on EIT in the future.

[1] with the foundation laid by this project

To all in the "new" generation, Søren, Andreas, Laurits, and Malthe, I would like to express my appreciation for your contribution to cultivating a pleasant and academically secure atmosphere in which no question is deemed stupid. Often, the best ideas are generated through discussions on basic concepts that everyone "should" be knowledgeable about. This special atmosphere has made it enjoyable and inspiring to work with you, and I hope that you, as the next generation of senior PhD students, will continue to uphold this culture.

Thanks to Jakob, Søren, Andreas, Ilja, Malthe, and Jan for proofreading parts of the thesis and providing honest and valuable feedback.

Finally, I would like to express my deepest gratitude to my wife, Ditte, for supporting me unconditionally throughout my entire PhD project. Thank you for being patient with me during exam periods and after late homecomings, and for teaching me how to disconnect from work and be present as a father when I get home. During the writing phase, you went above and beyond by taking special care of our children and the household, allowing me to focus on writing the PhD I wanted. I couldn't have done it without you.

Toke Vibel
Aarhus, February 13th, 2024

Note After submitting this thesis, I added a paragraph on imaging frequency uncertainty in Section 3.5.6, highlighting its significant impact on estimating errors in absorption imaging. Furthermore, I rectified the reference to the article presented in Chapter 5, which is now available in preprint.

List of publications

[1] T. Vibel, M. Christensen, R. Andersen, L. Stokholm, K. Pawłowski, K. Rzążewski, M. Kristensen and J. Arlt, 'Atom number fluctuations in Bose gases – statistical analysis of parameter estimation', arXiv, 2403.15047 (2024).

[2] T. Vibel, M. Christensen, M. Kristensen, J. Thuesen, L. Stokholm, C. Weidner and J. Arlt, 'Spatial calibration of high-density absorption imaging', arXiv, 2402.06514 (2024).

[3] M. Kruk, D. Hryniuk, M. Kristensen, T. Vibel, K. Pawłowski, J. Arlt and K. Rzążewski, 'Microcanonical and canonical fluctuations in atomic Bose-Einstein condensates – Fock state sampling approach', SciPost Phys. **14**, 036 (2023).

[4] M. Kruk, T. Vibel, J. Arlt, P. Kulik, K. Pawłowski and K. Rzążewski, 'Fock state sampling method - characteristic temperature of maximal fluctuations for interacting bosons in box potentials', Acta Phys. Pol. A **143**, S171–S178 (2023).

[5] M. Christensen, T. Vibel, A. Hilliard, M. Kruk, K. Pawłowski, D. Hryniuk, K. Rzążewski, M. Kristensen and J. Arlt, 'Observation of microcanonical atom number fluctuations in a Bose-Einstein condensate', Phys. Rev. Lett. **126**, 153601 (2021).

Contents

Chapter 1

Introduction

Quantum mechanics, the fundamental theory describing the physical laws relevant to atomic and subatomic systems, emerged at the beginning of the last century, as a revolutionary correction of classical physics. It dates back to the work of Max Planck in 1900, who introduced the concept of quantized energy to explain the spectral distribution of blackbody radiation [4]. Another cornerstone for quantum mechanics was provided by Albert Einstein's work on the photoelectric effect in 1905, proposing that light consists of discrete packets of energy, or photons [5]. Niels Bohr's model of the atom, introduced in 1913, was another pivotal development in quantum theory, suggesting that electrons orbit the nucleus in discrete, quantized energy levels [6].

Subsequent contributions by Louis de Broglie, Werner Heisenberg, Paul Dirac, Erwin Schrödinger, and many others further refined quantum theory, leading to, for instance, the development of the Schrödinger equation and the uncertainty principle. This collective effort among many physicists laid the groundwork for modern quantum mechanics. Over the decades, quantum mechanics has proven to be one of the most successful and accurate theories in the history of physics, providing explanations for phenomena ranging from the behavior of subatomic particles to the core of stars.

Quantum mechanics has not only revolutionized our understand-

ing of the fundamental nature of reality but has also had a profound impact on technology. Transistors [7] and lasers [8], among others, are direct products of quantum mechanics, which lay the foundation of the information age.

Looking ahead, the beginning of this millennium was marked by the onset of a second quantum revolution [9]. This revolution is formed by advancements in quantum sensing [10], quantum cryptography [11], quantum simulation [12] as well as quantum computing [13]. These upcoming technologies present the potential for another transformation of our world.

One of the most fascinating phenomena in quantum mechanics is Bose-Einstein Condensation (BEC), first predicted by Albert Einstein in 1925 [14] based on work by Satyendra Bose on statistics of photons [15]. BEC occurs when a dilute gas of bosonic particles is cooled to temperatures near absolute zero and is characterized by a macroscopic fraction of the particles occupying the lowest energy level of the system. This forms a collective macroscopic quantum state known as a Bose-Einstein condensate, which is large enough to be probed by optical means, rendering it a relatively accessible quantum phenomenon. The remaining atoms, distributed across excited states, collectively form what is known as the thermal cloud.

The experimental realization of BEC occurred approximately 70 years after its theoretical prediction. This milestone was achieved almost simultaneously by three groups [16–18], who successfully created the first Bose-Einstein condensates (BECs) in dilute alkali gases. Since then, the field of ultracold atoms has rapidly expanded, and BECs have become a routine experimental achievement, with over a hundred groups worldwide capable of producing them [19].

BECs are utilized in various fields, such as atom interferometry [20], quantum simulation [12, 21], and for enhancing atomic clocks and precision time measurements [22]. Moreover, they hold potential for applications in quantum information processing [23].

Given the significant prospects of BECs in both basic research and technology, a fundamental understanding of the phenomenon is crucial to ensure the reliability and accuracy of results obtained from its applications. The results of this PhD contribute to enhancing the detection of BECs and the interpretation of these measurements, thereby advancing our understanding of a fundamental characteristic of the phenomenon: atom number fluctuations.

1.1 Spatial calibration of absorption imaging

One of the primary outcomes of this PhD project is an improved calibration technique for time-of-flight absorption images of ultracold atomic clouds [1]. Absorption imaging, a resonant detection technique like fluorescence imaging [24, 25], stands as one of the most widely employed imaging techniques in the field of cold atoms. This technique involves illuminating the atoms with a laser beam and measuring the reduction of the light intensity by the cloud with a camera. While it has the drawback of being a destructive measurement, there exists a minimally destructive version known as partial-transfer absorption imaging [26]. Absorption imaging can also be configured in a *dark-ground* setting, where unscattered imaging light is blocked at an intermediate focus in the imaging setup [27, 28].

Accurate detection relies on the correct determination of the saturation intensity I_{sat}, which will generally differ from the result of the two-level atom due to the complex multi-level structure of the internal states of real atoms and imperfect polarization states of the probe beam. Additionally, the probing light imparts momentum to the atoms, which can lead to an effective detuning for typical probing durations. At higher densities, additional effects such as re-absorption

processes and coherent many-body scattering come into play [29, 30]. This, however, can, to some extent, be addressed by the calibration as presented in [31] , wherein an effective saturation intensity is introduced and calibrated.

Additional systematic effects include the presence of fringes in images caused by vibrations, which pose a significant challenge. This issue can be addressed by incorporating short pauses between the probe and reference images or through the utilization of fringe removal algorithms [32–34]. Another source of fringes, astigmatism, is addressed through centered optics and the avoidance of tilted lenses. Diffraction fringes arising from out-of-focus effects can be reduced using precise focusing techniques for the center of the cloud [35].

The gradual acceleration of atoms during imaging, induced by momentum kicks from the probe beam and spontaneous emission, gives rise to various effects. First, it introduces yet another out-of-focus effect by pushing the cloud out of the focus plane. Further, the recoil kicks from spontaneously emitted photons, cause a random walk of atoms and diffusion of the cloud during imaging [36]. The effective detuning of the imaging light caused by the Doppler shift accelerated atoms can be compensated by chirping the imaging laser frequency during the imaging [37].

On the electronic front, systematic effects arising from camera noise, encompassing photo response non-uniformity, dark current effects, sense node reset noise, source follower noise, and ADC quantization noise, contribute to the complexity of absorption imaging [38].

The work in this thesis presents an improved calibration technique for time-of-flight images of large samples of atoms. It is shown that the calibration depends on the optical density, *od*, by conducting separate calibrations for regions of identical *od* on a Gaussian-shaped cloud. Thus, a linear dependence between the calibration and the optical density is obtained, which can be directly implemented in absorption imaging. The spatial calibration technique results in corrections to

the detected atom number of approximately $\approx 12\%$ and temperature adjustments of around $\approx 14\%$ for typical ultracold atom clouds, as compared to earlier calibration methods.

1.2 Statistical analysis of atom number fluctuations

The second primary outcome of this PhD project is a comprehensive statistical analysis of uncertainties in the preparation and parameter estimation of partially condensed Bose gases, aimed at extending our understanding of atom number fluctuations in Bose-Einstein condensates [3]. While BEC finds use in research and applications as outlined above, there remain numerous fundamental unanswered questions. One such example is the phenomenon of atom number fluctuations in ultracold Bose gases.

The problem of the fundamental atom number fluctuations in ultracold Bose gasses is a complex issue that led to a long-standing debate started by E. Schrödinger and continued by the next generation of physicists [39–41]. Notably, the theoretical prediction of atom number fluctuation turns out to depend on the choice of statistical ensemble [41]. Initially, predictions based on the grand canonical ensemble indicated divergent fluctuations [42, 43]. Later, the leading contribution to atom number variance in the canonical ensemble, free from such divergence, was found in thermodynamic limit [40]. Moreover, the variance of the atom number calculated in the microcanonical ensemble is shown to be less than half of the one obtained in the canonical ensemble even in the limit of infinitely many atoms [44, 45]. Thus, to correctly describe the phenomenon, one has to invoke the statistical ensemble, which is closest to the experimental reality. For the nearly perfectly isolated system of the current BEC experiments,

the microcanonical ensemble seems to be the most appropriate [2]. As the total number of atoms is conserved, the number of the Bose condensed atoms is, therefore, perfectly anti-correlated with the number of the thermal ones.

This understanding of the fundamental atom number fluctuations guides the investigation of a direct characteristic of the fluctuations in a partially condensed Bose gas – namely, the anticorrelation between the atom number in the BEC and the thermal cloud. Simply put, one expects atoms leaving the BEC to enter the thermal component and vice versa. This motivated our analysis of the thermal cloud atom number variance and, consequently, the complete noise analysis of the system.

Prior investigations of errors in experiments with ultracold quantum gases have focused on systematic errors in absorption imaging and optimization strategies to mitigate them. These include the calibration of the effective saturation intensity [1, 29, 31, 37], the appropriate choice of fitting region for the thermal cloud [46], and the effect of increased cloud width due to recoil heating and defocusing [36, 47]. Correction techniques for the Doppler shift during imaging have also been explored [37, 48]. Experimental techniques have been developed to precisely determine the optimal focus for the imaging setup [35].

The statistical errors that occur in the preparation and parameter extraction of traditional absorption images have only received relatively little attention. In experiments aiming at accurate atom number determination the optimal settings for imaging power, pulse duration, and cloud size to minimize the impact of photon shot noise [27, 49, 50] have been explored. Techniques in imaging processing, aiming to reduce the effects of photon shot noise and eliminate fringes due to vibrations, have also been investigated [32–34, 51]. Statistical effects might not have received much attention in the past, since preparation errors often exceeded estimation errors. However, we have now reached a regime where experiments are becoming stable enough for es-

timation errors to become relevant. It is worth noting that for relative measurements, it is often feasible to mitigate the effects of preparation noise.

Measurement of fundamental atom number fluctuations is particularly challenging since technical noise arising from preparation and estimation directly competes with the main experimental result. Previous measurements detected the fluctuations [52] and characterized their dependence on atom number and trap geometry [2]. Here, we develop a detailed model of the technical noise sources based on Monte Carlo simulations of the estimation method, which allows us to subtract their contribution from the observed variances and isolate the fundamental atom number fluctuations.

1.3 Electromagnetically induced transparency

In the final part of this thesis, the initial steps towards an entirely new range of experiments are presented. Electromagnetically induced transparency (EIT) [23, 53, 54] stands as a fascinating phenomenon, demonstrating the remarkable ability to render an otherwise opaque medium transparent through the manipulation of its quantum states using laser light. Associated characteristics of EIT include the capability to slow down, halt, and even trap light within the medium [55].

It was first experimentally realized in BECs by Lene Hau et al. in 1999 [56], who is famous for slowing down light to the speed of a bicycle. Since then, interest in EIT has remained high due to its potential applications, ranging from the realization of quantum memory for light [57, 58] to quantum information processing [59, 60] and the exploration of strong light-atom coupling through collective enhancement [55, 57].

Inspired by the collaboration with theoretical groups in Aarhus [61, 62] the research focus of our group has now shifted towards realizing EIT. In our pursuit to measure this phenomenon, we became aware that even simple characteristics of EIT, such as the dependence of the width of the transparency window on optical density, have not been thoroughly explored. Consequently, this has become the current focus of the group's research.

1.4 Thesis outline

This thesis is structured as follows:

Chapter 2: Bose-Einstein condensation and atom number fluctuations
Key theoretical concepts of ultracold quantum gases are introduced, including fundamental principles such as Bose-Einstein condensation, the Gross-Pitaevskii equation, spatial distributions of Bose gases following free expansion, and an overview of atom number fluctuations in Bose-Einstein condensates.

Chapter 3: Experimental techniques
The apparatus and experimental techniques used to produce and detect ultracold atomic clouds are presented in this chapter, with particular emphasis placed on the experimental techniques and analyses developed within this project for absorption imaging.

Chapter 4: Spatial calibration of high-density absorption imaging
The spatial calibration technique for time-of-flight absorption images of ultracold atomic clouds is presented.

Chapter 5: Atom Number Fluctuations in BECs
A comprehensive statistical analysis is presented to assess uncertainties in the preparation and parameter estimation of partially con-

densed Bose gases, aimed at extending our understanding of atom number fluctuations in Bose-Einstein condensates.

Chapter 6: Experimental advances towards EIT

Experimental advancements aimed at measuring electromagnetically induced transparency are presented, focusing on the setup for a crossed optical dipole trap and a hybrid trap, as well as techniques for magnetic field control.

Chapter 7: Conclusion and Outlook

The thesis wraps up with a summary of the key findings and insights gained, followed by an outlook on potential paths for future research.

Chapter 2

Bose-Einstein condensation and atom number fluctuations

This chapter presents the main theoretical results essential for understanding the experimental and analytical techniques employed in this thesis. It contains fundamental theoretical concepts of the phenomenon of Bose-Einstein condensation (BEC) of harmonically trapped atomic bosons and an introduction to atom number fluctuations in BECs. Additionally, a description of spatial distribution functions of ultracold Bose gases after free expansion is presented. Finally, this chapter incorporates a section on statistical techniques relevant to this thesis.

2.1 Quantum Bose Gases

This section describes some fundamental theoretical results for Bose-Einstein Condensation, primarily based on [43, 63, 64]. A particular focus are results relevant to our laboratory's specific research, which involves weakly interacting repulsively interacting bosons (^{87}Rb) confined in anisotropic harmonic potentials given by

$$V_{\text{ext}}(x, y, z) = \frac{1}{2} m(\omega_x^2 x^2 + \omega_y^2 y^2 + \omega_z^2 z^2). \tag{2.1}$$

For most of the results presented in this thesis, the potential is of a prolate geometry (cigar-shaped), where the radial trapping frequency, $\omega_\rho = \omega_x = \omega_y$ is much greater than the axial ω_z. The aspect ratio, $\lambda = \omega_\rho/\omega_z$, is an essential geometric parameter for these traps.

2.1.1 Bose-Einstein statistics

The distribution function for a system of non-interacting particles in thermodynamical equilibrium can be derived from the grand canonical ensemble and reads [43, 63]

$$f^0(\varepsilon_i) \equiv \overline{n}_i = \frac{1}{e^{(\varepsilon_i - \mu)/k_\mathrm{B}T} \pm 1}, \tag{2.2}$$

where $\overline{n}_i$ denotes the mean occupation number of the single-particle state i, ε_i is the energy of the single-particle state, μ is the chemical potential, k_B is the Boltzmann constant, and T is temperature. The $(\pm)$ sign distinguishes between Fermi-Dirac $(+)$ and Bose-Einstein $(-)$ statistics, which apply to fermions and bosons, respectively. The latter will be the focus of this chapter.

It is clear from the Fermi-Dirac distribution that $\overline{n}_i < 1$ for any single-particle state. The limiting value occurs when $\mu \gg k_\mathrm{B}T$ and $\varepsilon_i \leq \mu$, and reflects the Pauli exclusion principle, that no identical fermions simultaneously occupy the same quantum. For the Bose-Einstein distribution, μ must be less than ε_0 for the ground state occupation $\overline{n}_0$ to be a positive number. By choosing the zero of the energy scale to be the ground state energy, $\varepsilon_0 = 0$, the chemical potential must be negative, $\mu < 0$. In stark contrast to Fermi-Dirac statistics, Eq. (2.2) shows that the Bose-Einstein distribution can lead to an anomalously large occupation of the ground state when $\mu \to 0^-$. This fascinating phenomenon is called Bose-Einstein condensation and is the focal point of this thesis.

For very high temperatures $\mu \to -\infty$ and the ± 1 in the denominator becomes insignificant, and both distribution functions reduce to the Maxwell-Boltzmann distribution

$$f^0_{\mathrm{MB}}(\varepsilon_i) = e^{-(\varepsilon_i - \mu)/k_{\mathrm{B}}T}, \tag{2.3}$$

which is applicable when quantum statistics is negligible.

To apply Eq. (2.2) to a particular system – in our case, harmonically trapped atomic bosons - one needs to calculate the energy of all states, which is generally difficult. Additionally, for a system with a finite number of particles like ours, the chemical potential should be determined as the value that ensures that the sum of the Bose-Einstein distribution adds up to the total number of atoms, N

$$N = \sum_{all\ i} \frac{1}{e^{(\varepsilon_i - \mu)/k_{\mathrm{B}}T} - 1}. \tag{2.4}$$

It is usually easier, to approximate Eq. (2.4) with a quasi-continuous Bose-Einstein distribution function

$$N_{\mathrm{th}} = \int_0^\infty g(\varepsilon) f^0(\varepsilon) d\varepsilon. \tag{2.5}$$

This is valid when the number of states involved is large, i.e. when $k_{\mathrm{B}}T$ is much larger than the energy level splitting. Here, the density of states, $g(\varepsilon)$, has been introduced, which is the number of single-particle states per unit of energy. This depends on the geometry of the confining potential. For a three-dimensional anisotropic harmonic trap, the density of states is given by [63]

$$g(\varepsilon) = \frac{\varepsilon^2}{2(\hbar\overline{\omega})^3}, \tag{2.6}$$

where $\overline{\omega} = (\omega_x \omega_y \omega_z)^{1/3}$ is the geometric mean of the trapping frequencies. Equation (2.5) fails to account for the ground state properly

but provides a good approximation for the number of atoms in the excited states. This explains the subscript *th* for the atom number in Eq. (2.5).

2.1.2 Critical temperature and condensate fraction

Before using Eq. (2.5) to determine μ, it will here be used to determine the critical temperature, T_c, of Bose-Einstein Condensation. The chemical potential is set to $\mu = 0$ (its limiting value) and Eq. (2.5) is evaluated [63]

$$N_{\text{th}}(T, \mu = 0) = \int_0^\infty \frac{\varepsilon^2}{2(\hbar\overline{\omega})^3} \frac{1}{e^{\varepsilon/k_B T} - 1} d\varepsilon = \frac{\zeta(3)(k_B T)^3}{(\hbar\overline{\omega})^3}. \tag{2.7}$$

Here, $\zeta(x)$ is the Riemann zeta function. Then, all atoms are required to be in the excited states at the critical temperature and one finds

$$N = N_{\text{th}}(T_c, \mu = 0) = \frac{\zeta(3)(k_B T_c)^3}{(\hbar\overline{\omega})^3} \quad \Longrightarrow \tag{2.8}$$

$$k_B T_c = \frac{\hbar\overline{\omega}}{\zeta(3)^{1/3}} N^{1/3}. \tag{2.9}$$

This is the critical temperature for a non-interacting gas of bosonic atoms confined in a 3D dimensional harmonic potential. Corrections to this temperature due to interactions and finite size effects are discussed, for instance, in [65].

Below the critical temperature, the atoms not in the excited states must be in the ground state. Thus, the BEC number is found by subtracting Eq. (2.7) from Eq. (2.8)

$$N_0 = N - N_{\text{th}}(T) = N \left[1 - \left(\frac{T}{T_c} \right)^3 \right]. \tag{2.10}$$

More accurate models when including interactions are available like, for instance, the semi-ideal model [66], where the BEC atom number is given by the following equation

$$\frac{N_0}{N} = 1 - \left(\frac{T}{T_c}\right)^3 - \eta\frac{\zeta(2)}{\zeta(3)}\left(\frac{T}{T_c^0}\right)^2\left(\frac{N_0}{N}\right)^{2/5}. \tag{2.11}$$

Here, the scaling parameter is defined as

$$\eta = \frac{1}{2}\zeta(3)^{1/3}\left(15N^{1/6}a\right)^{2/5} \tag{2.12}$$

where the scattering length a is scaled in units of $\sqrt{\hbar/m\overline{\omega}}$. Equation (2.11) can be solved numerically. This result agrees reasonably well with experimental results [52, 67, 68].

2.1.3 Chemical potential above critical temperature

Above the critical temperature, the chemical potential, μ, can be determined using Eq. (2.5), allowing for negative values of μ. The condition for the chemical potential becomes

$$N = \int_0^\infty d\varepsilon\, g(\varepsilon)\frac{1}{\tilde{z}^{-1}e^{\varepsilon/k_BT} - 1} = \left(\frac{k_BT}{\hbar\overline{\omega}}\right)^3 g_3(\tilde{z}). \tag{2.13}$$

Here, the fugacity

$$\tilde{z} = \exp(\mu/k_BT) = \exp(\overline{\mu}) \tag{2.14}$$

has been introduced with $\overline{\mu} = \mu/k_BT$ being the reduced chemical potential. $g_\gamma(x)$ is called the Bose function or the Polylogarithm function and is defined as

$$g_\gamma(x) = \sum_{j=1}^{\infty}\frac{x^j}{j^\gamma}. \tag{2.15}$$

Equation (2.13) can be solved numerically for μ, which is a function of N, T and the trap potential. This will become important when considering spatial distributions of atom clouds in Section 2.3.

2.1.4 Gross-Pitaevskii equation

At this point, Bose-Einstein condensates have been discussed as a statistical phenomenon for non-interacting particles, which is often a good approximation for the thermal cloud. But, in real-life scenarios atoms interact, and the ideal gas results do not apply to BECs in this case. Thus, this section examines the ground state wave function of a Bose-Einstein condensate in the presence of these interactions for which the Gross-Pitaevskii equation (GPE) is essential.

Consider a bosonic gas of neutral atoms at zero temperature ($T = 0$) confined by an external potential $V_{\text{ext}}(\mathbf{r})$, and assume that the interatomic potential has a short range and may be approximated by a contact potential

$$\mathcal{V}(\mathbf{r}_i, \mathbf{r}_j) = U_0 \delta(\mathbf{r}_i - \mathbf{r}_j) \tag{2.16}$$

with the effective interaction given by

$$U_0 = \frac{4\pi\hbar^2 a}{m} \tag{2.17}$$

which is described using a single parameter denoted the *scattering length*, a.

If one further uses a mean-field approach and assumes that each particle in the system interacts with an average or mean-field created by all other particles, neglecting detailed information about individual particle-particle interactions, the wave function of the condensate can be simplified to a description by a single spatial variable $\Psi(\mathbf{r}_1, \mathbf{r}_2, ...\mathbf{r}_N,) \rightarrow \psi(\mathbf{r})$. The condensate function is defined as

$$\psi(\mathbf{r}) = \sqrt{N_0}\phi(\mathbf{r}), \tag{2.18}$$

where $\phi(\mathbf{r})$ is the single-particle ground-state wave function. The density of the condensate mirrors the form of the ground-state wave function

$$\tilde{n}(\mathbf{r}) = |\psi(\mathbf{r})|^2 = N_0|\phi(\mathbf{r})|^2. \tag{2.19}$$

Under these assumptions, one can derive the well-known equation that describes the structure of the condensate wave function - namely the Gross-Pitaevskii equation [63]

$$\left(-\frac{\hbar^2}{2m}\nabla^2 + V_{\text{ext}}(\mathbf{r}) + U_0|\psi(\mathbf{r})|^2\right)\psi(\mathbf{r}) = \mu\psi(\mathbf{r}). \tag{2.20}$$

This is a Schrödinger-like equation, but, importantly, it contains a non-linear term due to the mean-field interaction, and the energy is replaced by the chemical potential.

An important solution of Eq. (2.20) is obtained by applying the Thomas-Fermi approximation. It can be applied when dealing with a sufficiently large condensate, where the Gross-Pitaevskii equation's mean field interaction term becomes large due to its non-linearity. If the scattering length is positive, it results in a repulsive effective interaction between the particles, leading to a broader density distribution as the high-density center particles try to decrease their energy. In such cases, the kinetic energy term becomes relatively small in comparison to the potential and mean-field terms and, hence, can be neglected. In this case Eq. (2.20) has the simple solution

$$n(\mathbf{r}) = |\psi(\mathbf{r})|^2 = \frac{\mu - V_{\text{ext}}(\mathbf{r})}{U_0}. \tag{2.21}$$

Equation (2.21) applied to harmonic traps will be explored in Section 2.3.

2.2 Atom number fluctuations of BECs

When describing the atom number in the Bose-Einstein condensate as a statistical phenomenon, the primary focus has often been the mean value, as given in Eq. (2.10). However, it is equivalently interesting to study higher moments of BEC number, with the next one being the variance. This is likewise sensitive to the physics of the interacting Bose gas. Thus, it is an excellent test of our understanding of many-body quantum systems, to check if the theoretical expectation of the atom number fluctuations matches the experimental measured one.

The theoretical prediction of atom number fluctuation turns out to depend on the choice of statistical ensemble [39, 69]. Thus, here is a brief exploration of the three commonly employed idealized statistical ensembles in statistical mechanics. The grand canonical ensemble characterizes a system of particles within a fixed volume, reaching thermodynamic equilibrium with a reservoir, allowing for the exchange of heat and particles [70]. Consequently, the energy and particle number of the system varies while the temperature and chemical potential are fixed. In the canonical ensemble, the particle number is fixed, yet the system can exchange energy with a reservoir, thereby fixing the temperature according to the reservoir. On the other hand, the microcanonical ensemble represents a fully isolated system of particles with fixed total energy and particle number. Despite this ensemble closely resembling conditions in typical experiments with ultracold Bose gases, computations within the microcanonical ensemble pose greater challenges compared to those in the canonical and, especially, the grand canonical ensemble [69].

Thus, it is somewhat surprising that the results derived within the grand canonical ensemble fairly accurately predict the BEC fraction and critical temperature. On the other hand, the different ensembles are usually expected to be equivalent for large systems, where the energy and particle number distributions become narrow, erasing the

differences between the ensembles [70].

2.2.1 Grand canonical fluctuations

All theoretical results shown so far have been achieved by applying the grand canonical ensemble to a non-interacting Bose gas and using the chemical potential as a normalization parameter to ensure, that the average total particle number is fixed. Already very early, however, E. Schröding found that in this model the atom number fluctuations diverge [42, 43]

$$\Delta N_0^2 = N_0(N_0 + 1). \tag{2.22}$$

Here ΔN_0 denotes the standard deviation and ΔN_0^2 the variance. Thus, the grand canonical model predicts the fluctuations to reach a magnitude identical to the mean value of the BEC. Such a scenario raises questions about the very existence of the BEC, as it suggests a state where the condensate appears and disappears abruptly. Also, in the limit of zero temperature, $T \to 0$, where all atoms are in the ground state $N_0 \to N$ any non-zero fluctuation will be unphysical. The failure of the grand canonical ensemble to determine the fluctuations of the BEC was further disclaimed in [39], where it was also shown that the grand canonical and canonical predictions differ for the atom number fluctuations. The inadequacy of the grand canonical ensemble is by some referred to as the grand canonical fluctuations catastrophe [41, 45]. An example of the fluctuations as a function of temperature is shown in Fig. 2.1.

2.2.2 Canonical fluctuations

Later, H. D. Politzer found the leading contribution to atom number variance in the canonical ensemble in the thermodynamic limit of $N \to \infty$ [40]. He treated the condensate as a particle reservoir for all the

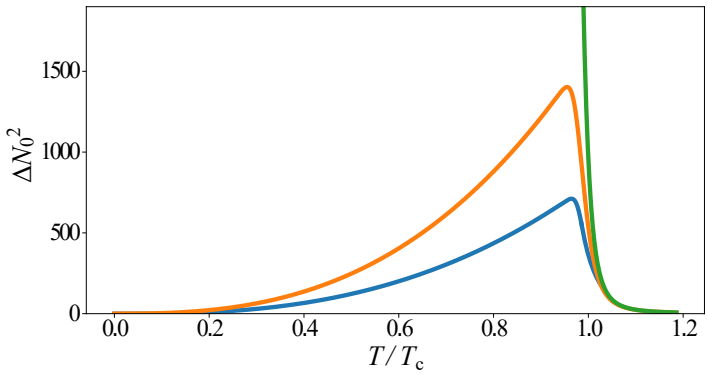

FIGURE 2.1: Comparison of the atom number fluctuations of the BEC calculated in the grand canonical ensemble (green), the canonical ensemble (orange), and the microcanonical ensemble (blue). The results are exact calculations for systems of $N = 1000$ atoms trapped in a spherical harmonic trap. The figure is reprinted from [69].

excited states which is the condition of the grand canonical description. This is valid for very low temperatures when most of the particles are in the ground state. Further, the total atom number was fixed making the result canonical. The result for the 3-dimensional spherical trap is

$$\Delta N_0^2 = \frac{\zeta(2)}{\zeta(3)} N \left(\frac{T}{T_c} \right)^3 . \tag{2.23}$$

Subsequently, it was demonstrated that exact numerical calculations of fluctuations in the non-interacting trapped gas within the canonical ensemble can be accomplished through a recurrence relation [71] for the entire temperature range (see Fig. 2.1). These predictions are possible for traps with anisotropic geometry as well.

2.2.3 Microcanonical fluctuations

The microcanonical result in the low-temperature limit for a spherical harmonic trap and for large atom numbers was obtained using the Maxwell's demon ensemble (or the fourth ensemble) [44]. Similarly to [40] the condensate is treated as the reservoir of particles, allowing for the exchange of particles but without exchanging heat. The term Maxwell's demon is used to emphasize the action of an intelligent creature required to facilitate this behaviour. For instance, when a thermal atom transitions to the BEC, its energy must be redistributed among the remaining thermal atoms to prevent heat exchange between the BEC and the thermal cloud. The result is

$$\Delta N_{0,\mathrm{MC}}^2 = \left(\frac{\zeta(2)}{\zeta(3)} - \frac{3\zeta(3)}{4\zeta(4)}\right) N \left(\frac{T}{T_\mathrm{c}}\right)^3 . \tag{2.24}$$

Thus, the fluctuations in the microcanonical ensemble are expected to be smaller than in the canonical ensemble. For small atom numbers, an exact recursion relation can also be employed [69, 71] (see Fig. 2.1). Further attempts to treat microcanonical fluctuations in finite size systems were made in [72] using the so-called saddle point method.

2.2.4 The Fock state sampling method

The fluctuation results presented so far are valid for non-interacting bosons. Studies on fluctuation in interacting bosons have also been conducted extensively using different methods and with validity in different regimes [41, 69]. However, the results are varied and contradictory with respect to whether interactions increase or decrease the magnitude of the fluctuations.

A lot of these issues were solved by the Fock state sampling (FSS) method [69]. In this method, the collective state of the entire atom cloud is represented in the multimode Fock states basis $|\theta\rangle = |N_0, N_1, ...\rangle$

where N_j are occupations of the j's eigenstate of a single-particle trapped in a potential $V_{\text{ext}}(\mathbf{r})$ and the total atom number is fixed, $N = \sum_j N_j$. The Monte Carlo technique called the Metropolis algorithm is used to sample the Fock state configurations under the constraint of the canonical ensemble. For a sufficiently high number of repetitions, the ensemble should be well-represented and the variances of the BEC number can be evaluated directly. This method effectively predicts the atom number fluctuations in the canonical ensemble for non-interacting particles for various aspect ratios and total atom numbers up to $N = 10^5$.

Importantly, it is possible to post-select the configurations with a total energy within a certain interval. For intervals narrow enough the remaining configurations effectively represent the microcanonical ensemble with its fixed energy. Since this can also be calculated for systems of up to $N = 10^5$ this technique is a major advancement as it can be used much closer to the experimental regime [69].

Finally, since single-particle eigenstates are used the results primarily represent the non-interacting case. However, it is possible to include the effect of weak interactions where the state of the condensate does not differ significantly from the lowest harmonic oscillator state. Since all of these results can be carried out in the full temperature range of the condensate, this approach solved various controversial issues in the understanding of atom number fluctuations in the microcanonical ensemble and the role of interactions.

Focusing on the harmonic trap in 3 dimensions, it was confirmed that the microcanonical fluctuations (Fig. 2.2) are lower than the canonical (Fig. 2.3). The role of interactions, however, turns out to be dependent on the trap geometry. In both the canonical and the microcanonical case, it was found that interactions cause the peak fluctuations to increase for an elongated trap, $\lambda = 7$, while decreasing (or being unaffected in the microcanonical case) for a spherical trap, $\lambda = 1$. The shift of the temperature for the peak fluctuations has

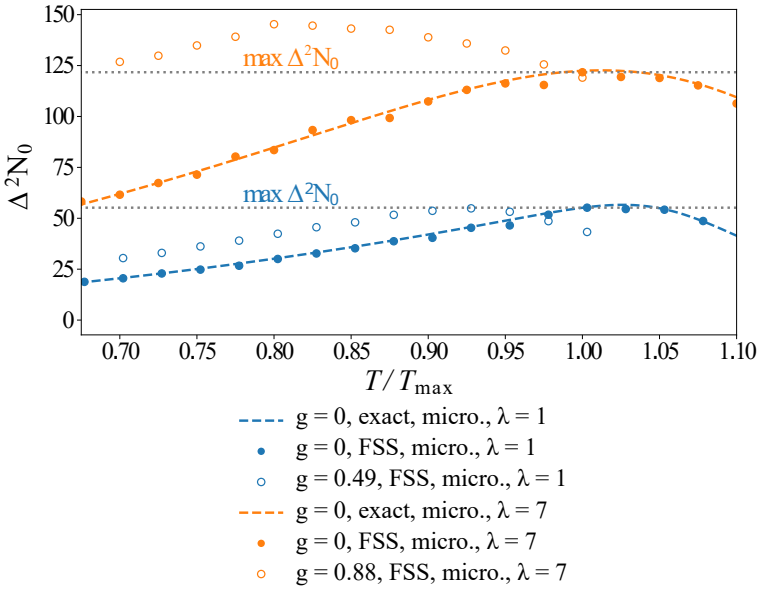

FIGURE 2.2: Microcanonical fluctuations of the atom number, both with and without interactions, within a harmonically trapped gas consisting of $N = 100$ atoms. The spherical case is shown in blue, and the elongated case $\lambda = 7$ is shown in orange. The results for the non-interacting case is both calculated exactly (dashed lines) and using Fock State Sampling method (solid circles). The interacting cases (open circles) have also been calculated using the FSS method. The interaction parameter g is the interaction strengths in units of $\sqrt{\hbar^5/m^3\overline{\omega}}$. The reference temperature $T_{\max}$ is the temperature of maximal fluctuations of the non-interacting gas in the canonical ensemble. The figure is reprinted from [69]

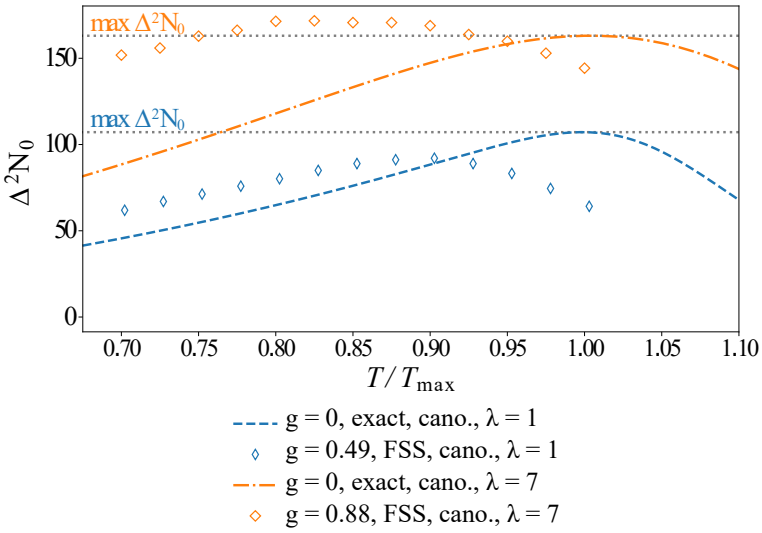

FIGURE 2.3: Canonical fluctuations of the atom number, both with and without interactions, within a harmonically trapped gas consisting of $N = 100$ atoms. The spherical case is shown in blue, and the elongated case ($\lambda = 7$) is shown in orange. The results for the non-interacting case (dashed lines) are exact while the the results for the interacting case (diamonds) were calculated using the Fock State Sampling method. The interaction parameter g is the interaction strengths in units of $\sqrt{\hbar^5/m^3\overline{\omega}}$. The reference temperature T_{max} is the temperature of maximal fluctuations of the non-interacting gas in the canonical ensemble. The figure is reprinted from [69]

the following consequence. When investigating fluctuations at a fixed, low temperature, interactions result in an increase in the fluctuations. Thus, it is not possible to provide a single answer regarding the effect of interactions on the atom number fluctuations in a Bose-Einstein condensate.

It should be mentioned that the fluctuations, of course, also depend on the total atom number and the limiting value for large numbers is obtained by dividing Eq. (2.24) with Eq. (2.23)

$$S_{\mathrm{lim}} = 1 - \frac{3\zeta(3)^2}{4\zeta(4)\zeta(2)} \approx 0.39 \tag{2.25}$$

is approached, confirming the difference in the canonical and microcanonical fluctuations in the thermodynamical limit.

Although the FFS method is an important tool towards predicting the fluctuation of atom numbers in realistic experimental systems, it is currently not practically feasible to estimate the fluctuations for systems with $N > 10^5$ in elongated geometries with $\lambda > 1$ [69]. Additionally, using the lowest harmonic oscillator state for the condensate wavefunction does not allow for interactions with the magnitude typically found in experiments. As a result, it is still not possible to directly compare theoretical predictions with experimental results.

2.3 Density profiles and momentum distribution

For cold clouds of atoms, the most important way to gain information about the system is through measurements of the density profile. This can be done in-trap or, alternatively, by abruptly turning off the trap and allowing the cloud to expand freely during some time-of-flight (TOF). The final spatial distribution of particles following a

cloud's expansion depends on the initial density and momentum distribution. Thus, it is important to account for both the density and momentum distributions. The experimental techniques used to extract density profiles will be treated in detail in Section 3.5. For now, it is important to note that instead of the actual density profile, the column densities, represented by $\tilde{n} = \int \mathrm{d}r_i \, n(r_i)$, are observed, where the density has been integrated along the line of sight of the imaging. In the following section, the most important theoretical distributions for harmonic traps will be presented, as they constitute the important fittings function for the experimentally obtained density profiles.

2.3.1 Thermal cloud distributions

Determination of the in-trap distribution of the thermal cloud is typically done using a semi-classical approach. By inserting the energy of a single classical particle

$$\varepsilon_0(\mathbf{r}, \mathbf{p}) = \frac{\mathbf{p}^2}{2m} + V(\mathbf{r}) \tag{2.26}$$

in Eq. (2.2) the Bose distribution function can be written as

$$f(\mathbf{r}, \mathbf{p}) = \frac{1}{e^{(\varepsilon_0(\mathbf{r},\mathbf{p})-\mu)/k_\mathrm{B}T} - 1}. \tag{2.27}$$

Semi-classically, the number of quantum states within the phase-space volume $\mathrm{d}\mathbf{r}\mathrm{d}\mathbf{p}$ is $\mathrm{d}\mathbf{r}\mathrm{d}\mathbf{p}/(2\pi\hbar)^3$. Thus, $f(\mathbf{r}, \mathbf{p})\mathrm{d}\mathbf{r}\mathrm{d}\mathbf{p}/(2\pi\hbar)^3$ is the mean number of particles within $\mathrm{d}\mathbf{r}\mathrm{d}\mathbf{p}$. The Bose distribution function in Eq. (2.27) is valid as long as information about the particle distribution at the length scale Δl and momentum scale Δp is not required, which violates Heisenberg's uncertainty principle $\Delta l \Delta p \geq \hbar/2$. Further, it is required that the characteristic length at which momentum changes

significantly is much larger than the thermal de Broglie wavelength

$$\lambda_{\mathrm{T}} = \sqrt{\frac{2\pi\hbar^2}{m k_{\mathrm{B}} T}}, \tag{2.28}$$

which can be interpreted as the extent of the wave packets within which the atoms are localised. When integrating over the entire phase space, it is again required that it adds up to the thermal atom number

$$N_{\mathrm{th}} = \frac{1}{(2\pi\hbar)^3} \int \frac{1}{e^{(\varepsilon_0(\mathbf{r},\mathbf{p})-\mu)/k_{\mathrm{B}}T} - 1} \mathrm{d}\mathbf{r}\mathrm{d}\mathbf{p}. \tag{2.29}$$

Note the equivalence to Eq. (2.4) and (2.5). Integrating solely over the momentum distribution provides the density of the thermal cloud

$$n_{\mathrm{th}}(\mathbf{r}) = \int \frac{d\mathbf{p}}{(2\pi\hbar)^3} \frac{1}{e^{(p^2/2m + V_{\mathrm{ext}}(\mathbf{r})-\mu)/k_{\mathrm{B}}T} - 1}, \tag{2.30}$$

with the solution [63]

$$n_{\mathrm{th}}(\mathbf{r}) = g_{3/2}\left(e^{(\mu - V_{\mathrm{ext}}(\mathbf{r}))/k_{\mathrm{B}}T)}\right). \tag{2.31}$$

For a 3D harmonic potential (Eq. (2.1)) this becomes a Bose-enhanced Gaussian distribution [73]

$$n_{\mathrm{th}}(\mathbf{r}) = \frac{N}{(2\pi)^{3/2}\sigma_x\sigma_y\sigma_z g_3(\tilde{z})} g_{3/2}\left(\tilde{z} e^{-\sum_{i=x,y,z} r_i^2/2\sigma_i^2}\right), \tag{2.32}$$

with the in-trap cloud widths $\sigma_i = \sqrt{\frac{k_{\mathrm{B}}T}{m\omega_i^2}}$. In the high-temperature limit, where $\mu \to -\infty$ and the $\tilde{z} \to 0$ only the first terms in the Bose functions $g_{3/2}$ and g_3 are relevant, and the expression reduces to a Gaussian distribution, which is expected for a gas at high temperature, where the Maxwell-Boltzmann distribution is applicable

$$n_{\mathrm{th}}^{\mathrm{MB}}(\mathbf{r}) = \frac{N}{(2\pi)^{3/2}\sigma_x\sigma_y\sigma_z} e^{-\sum_{i=x,y,z} r_i^2/2\sigma_i^2}. \tag{2.33}$$

To calculate the spatial distribution after time-of-flight, it may be assumed that the atoms, after the trap is abruptly turned off, travel ballistically according to the in-trap initial momentum, such that position after time of flight can be written as $\mathbf{r} = \mathbf{r}_0 + \mathbf{p}t/m$. Substituting this into the distribution function $f(\mathbf{r}_0, \mathbf{p}) = f_0(\mathbf{r} - \mathbf{p}t/m, \mathbf{p})$ modifies Eq. (2.30) to

$$n_{\mathrm{th}}(\mathbf{r}, t) = \int \frac{d\mathbf{p}}{(2\pi\hbar)^3} \frac{1}{e^{(p^2/2m + V_{\mathrm{ext}}(\mathbf{r} - \mathbf{p}t/m) - \mu)/k_{\mathrm{B}}T} - 1}. \tag{2.34}$$

For the anisotropic harmonic potential, this has the solution [73]

$$n_{\mathrm{th}}(\mathbf{r}) = \frac{N}{(2\pi)^{3/2} w_x w_y w_z g_3(\tilde{z})} g_{3/2}\left(\tilde{z} e^{-\sum_{i=x,y,z} r_i^2/2w_i^2}\right), \tag{2.35}$$

with a cloud width after expansion given by

$$w_i = \sqrt{\frac{k_{\mathrm{B}}T}{m}\left(\frac{1}{\omega_i^2} + t^2\right)} = \sigma_i \sqrt{1 + \omega_i^2 t^2}. \tag{2.36}$$

The Bose-enhanced distribution becomes gradually more peaked compared to a Gaussian distribution when lowering the temperature and the reduced chemical potential, $\overline{\mu}$. The upper panel of Fig. 2.4 shows examples of Eq. (2.35) for different choices of $\overline{\mu}$.

The column density $\tilde{n}(x, y) = \int \mathrm{d}z\, n(x, y, z)$ after TOF is obtained by integrating Eq. (2.35) along the imaging line of sight yielding

$$\tilde{n}_{\mathrm{BE}}(x, y) = \frac{N_{\mathrm{th}}}{2\pi w_x w_y g_3(\tilde{z})} g_2\left[\tilde{z} \exp\left(-\frac{(x - c_x)^2}{2w_x^2} - \frac{(y - c_y)^2}{2w_y^2}\right)\right]. \tag{2.37}$$

Here, the center coordinates of the cloud c_x, c_y have been included explicitly to make it clear that these are fitting parameters in an

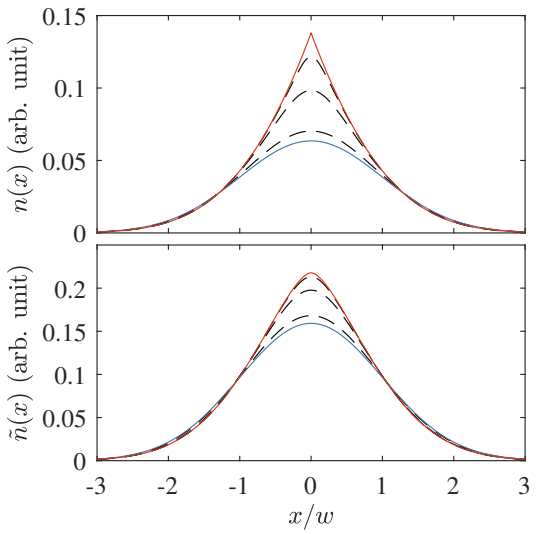

FIGURE 2.4: Density (upper panel) and column density (lower panel) along a cut through the center of thermal cloud profiles in the x direction. In both figures, the blue profile is the Maxwell-Boltzmann distribution ($\overline{\mu} = \mu/k_{\mathrm{B}}T = -\infty$), and the red distribution is the maximally peaked Bose-Enhanced Gaussian distribution ($\overline{\mu} = 0$). For the three intermediate distributions marked with dashed black lines $\overline{\mu} = -1, -0.1, -0.01$.

experiment. In the high-temperature limit, this again reduces to a Maxwell-Boltzmann distribution

$$\tilde{n}_{\mathrm{MB}}(x,y) = \frac{N_{\mathrm{th}}}{2\pi w_x w_y} \exp\left(-\frac{(x-c_x)^2}{2w_x^2} - \frac{(y-c_y)^2}{2w_y^2}\right). \tag{2.38}$$

In the low-temperature limit, it reduces to the maximally peaked Bose-

enhanced Gaussian distribution

$$\tilde{n}_{\mathrm{BE},0}(x,y) = \frac{N_{\mathrm{th}}}{2\pi w_x w_y \zeta(3)} g_2 \left[\exp\left(-\frac{(x-c_x)^2}{2w_x^2} - \frac{(y-c_y)^2}{2w_y^2}\right)\right]. \tag{2.39}$$

Figure 2.4 shows a comparison of Eq. (2.38) and (2.39) as well as intermediate distributions of Eq. (2.37) with different choices for $\overline{\mu}$. Note, that the difference between the maximally peaked Bose-Enhanced and the Gaussian distribution decreases when studying column densities instead of actual densities.

In experiments Eq. (2.38) and (2.39) are typically used instead of Eq. (2.37) because introducing another fitting parameter, e.g. $\overline{\mu} = \mu/k_{\mathrm{B}}T$, typically over-parametrizes the fitting procedure. The fitting parameters of the limiting distributions are N_{th}, c_x, w_x, c_y, and w_y.

However, since the $w_i(T)$ are functions of, T, and the fugacity $\tilde{z}(\mu, T)$ is a function of T and the chemical potential, $\mu(N_{\mathrm{th}}, T)$, which is a function of N_{th} and T, Eq. (2.37) can actually be considered a fitting model with the parameters, N_{th}, T, c_x, c_x. This is a slow fitting process since Eq. (2.13) needs to be solved numerically for each function call. But the speed and the robustness can be improved by determining N_{th}, c_x, c_x separately and letting T be the only fitting parameter. This technique is exploited in Section 3.5.5.

2.3.2 BEC distribution

The density profile of the condensate in a harmonic trap is obtained by inserting Eq. (2.1) into Eq. (2.21)

$$n(\mathbf{r}) = \frac{15}{8\pi} \frac{N_0}{R_x R_y R_z} \max\left(0, 1 - \frac{x^2}{R_x^2} - \frac{y^2}{R_y^2} - \frac{z^2}{R_z^2}\right). \tag{2.40}$$

Here, the Thomas-Fermi radius is $R_i = \sqrt{\frac{2\mu}{m\omega_i^2}}$, and the *max* function ensures that the density is zero outside the condensate. Thus, the BEC

is an inverted paraboloid. The chemical potential is determined by the normalization criterion, resulting in the following relation between N_0 and μ

$$\mu = \frac{15^{2/5}}{2}\left(\frac{N_0 a}{a_{\text{ho}}}\right)^{2/5}\hbar\overline{\omega}, \tag{2.41}$$

where $a_{\text{ho}} = \sqrt{\frac{\hbar}{m\overline{\omega}}}$ is the harmonic oscillator length.

The density profile for the interacting BEC after some time-of-flight is not purely ballistic but driven initially by the repulsion between the atoms. It can be shown, however, that the condensate in the Thomas-Fermi regime remains the parabolic shape once it has been released from the trap [74, 75].

For an anisotropic trap cigar-shaped trap where the radial trapping frequency, $\omega_\rho = \omega_y = \omega_z$ is much greater than the axial ω_x, the expansion of the cloud can be determined by scaling the in-trap Thomas-Fermi radius of the condensate according to [74]:

$$\begin{aligned} R_\rho(t) &= R_\rho(0)\sqrt{1+\tau^2} \\ R_x(t) &= R_x(0)\left(1+\varepsilon^2\left[\tau\arctan\tau - \ln\sqrt{1+\tau^2}\right]\right) \end{aligned} \tag{2.42}$$

with $\tau = \omega_\rho t$ and $\varepsilon = \omega_x/\omega_\rho$ and $R_y(t) = R_z(t) = R_\rho(t)$.

The column density after TOF is obtained by integrating out the z dimension of Eq. (2.40) [47] is then

$$\tilde{n}(x,y) = \tilde{n}(0)\max\left(0, 1 - \frac{x^2}{R_x^2} - \frac{y^2}{R_y^2}\right)^{3/2} \tag{2.43}$$

where $\tilde{n}(0) = 4/3R_\rho n(0) = 5N/(2\pi R_\rho R_x)$. Here, the R_i are to be understood as fitting parameters, but they should follow the dynamics described by Eq. (2.42).

2.4 Statistical analysis methods

Statistical analysis and the understanding of measurement errors are essential for scientific research. As my PhD work heavily relies on statistical analysis, this section introduces some fundamental statistical methods [76].

2.4.1 Data condensation

Data analysis involves condensing information, to gain an understanding of a large dataset using a minimal set of parameters. The fundamental methods for data condensation are the mean value, and the data spread, often quantified by variance. For a dataset of n measurements $\{x_1, x_2, ..., x_n\}$, the sample mean value is given by

$$\bar{x} = \frac{1}{n}\sum_{i=1}^{n} x_i. \tag{2.44}$$

The sample variance is given by

$$\Delta x^2 = s_x^2 = \frac{1}{n-1}\sum_{i=1}^{N}(x_i - \bar{x})^2, \tag{2.45}$$

where delta Δx and s_x are two equivalent notations of the sample standard deviation. These are measures of the spread of the data. The variance is the second central moment with the general expression for higher orders

$$m_k = \frac{1}{n-1}\sum_{i}^{n}\left(x_i - \bar{x}\right)^k. \tag{2.46}$$

The third and fourth moments (apart from normalization and some constants) are called *skewness* and *curtosis*, respectively.

An alternative measure of the variance is the two-sample variance [77] given by

$$\Delta x^2 = \frac{1}{2}\left\langle (x_{i+1} - x_i)^2 \right\rangle . \tag{2.47}$$

Here, x_{i+1} and x_i represent two adjacent measurements (in time). The two-sample is especially relevant for experimental data as it is equivalent to the variance but excludes slow temporal drift.

Standard error and spread of the sample variance

It is crucial to know the precision with which the mean or variance is estimated. The spread of the mean value is termed the *standard error*, denoted by α, and is given by

$$\alpha_x = \frac{s_x}{\sqrt{n}}. \tag{2.48}$$

This formula emphasizes the importance of minimizing statistical error by increasing the number of independent measurements.

The spread of the variances can be quantified by the formula [50, 78]

$$e(\Delta x^2) = \sqrt{n\frac{m_4(n-1)^2 - m_2^2(n^2-3)}{(n-3)(n-2)(n-1)^2}} \tag{2.49}$$

where m_k are the central moments (Eq. (2.46)). This result is of particular importance in this thesis as it is used to calculate the error of a fluctuations measurement in Chapter 5.

Covariance

In a statistical problem involving m variables $x_1, x_2, ...x_m$, recorded for each measurement, one will obtain m interconnected sets $\left\{x_j^1, x_j^2, ..., x_j^n\right\}$

of n measurements. The dependence between each of the m variables can be quantified using the covariance given by

$$\mathrm{cov}(x_i, x_j) = \sigma_{ij} = \frac{1}{n-1} \sum_{k=1}^{n} \left(x_i^{(k)} - \overline{x_i} \right) \left(x_j^{(k)} - \overline{x_j} \right). \tag{2.50}$$

Information about the variances and covariances are often given in the symmetric covariance matrix, $\mathbf{\Sigma}_x$ with the components given by Eq. (2.50)

$$\mathbf{\Sigma}_x = \begin{bmatrix} \sigma_1^2 & \sigma_{12} & \dots & \sigma_{1m} \\ \sigma_{21} & \sigma_2^2 & \dots & \sigma_{2m} \\ \vdots & \vdots & \ddots & \vdots \\ \sigma_{m1} & \sigma_{m2} & \dots & \sigma_m^2 \end{bmatrix}. \tag{2.51}$$

Since the covariance has units, it can often be difficult to interpret. A more intuitive measure of the relation between variables is offered by the *correlation coefficient* given by

$$\rho_{ij} = \frac{\sigma_{ij}}{\sigma_i \sigma_j} \tag{2.52}$$

which is a number between -1 and 1. If ρ_{ij} is 1 (-1) the variables are completely correlated (anti-correlated). If ρ is 0 the variables are uncorrelated. The *correlation coefficients* are like the covariances often collected in a symmetric matrix, $\mathbf{R}$.

2.4.2 Theoretical distributions

In statistical analysis, understanding the probability distributions of measured data is essential for interpreting and drawing meaningful conclusions from data. Idealized statistical distributions serve as mathematical models that capture the primary patterns observed in various phenomena. In this section, the three primary distributions is explored, each modelling distinct types of data.

Gaussian Distribution

The Gaussian distribution, also known as the normal distribution, holds a central position in statistical theory. The probability density function (pdf) of the Gaussian distribution is defined as

$$P(x|\mu,\sigma) = \frac{1}{\sqrt{2\pi\sigma^2}} \exp\left(-\frac{(x-\mu)^2}{2\sigma^2}\right), \tag{2.53}$$

where μ is the mean, σ is the standard deviation, and the variance is given by σ^2. Its significance is stressed by the **Central Limit Theorem** (CLT), stating that the sum (or average) of a large number of independent, identically distributed random variables, regardless of their original distribution, tends to follow a Gaussian distribution. In practice, this means that when measuring a physical quantity repetitively the mean value can be approximated with a Gaussian distribution.

Poisson Distribution

The Poisson distribution models the number of events that occur within a fixed interval of time or space, given a known average rate of occurrence. It is particularly relevant in situations involving counting, such as the number of photons detected by a CCD camera. The probability mass function (pmf) of the Poisson distribution is expressed as

$$P(k|\lambda) = \frac{e^{-\lambda}\lambda^k}{k!}, \tag{2.54}$$

where k is a non-negative integer, and λ is the average rate of occurrence. The mean and variance of a Poisson distribution are both equal to λ. When λ is large (rule of thumb, $\lambda \gtrsim 30$) the Poisson distribution can be approximated with a Gaussian. It is standard procedure to approximate the error of a measurement of k' events by $\Delta k \approx \sqrt{k'}$.

Binomial Distribution

The Binomial distribution models the number of successes in a fixed number of independent Bernoulli trials - that is a random experiment with exactly two possible outcomes: *success* and *failure*. For the fixed probability of success, p, the probability mass function is given by

$$P(k|n,p) = \binom{n}{k} p^k (1-p)^{n-k}, \tag{2.55}$$

where n is the number of trials, k is the number of successes, and

$$\binom{n}{k} = \frac{n!}{k!(n-k)!} \tag{2.56}$$

is the binomial coefficient. The mean value is np, and the variance is $np(1-p)$. For large n and near $p \approx 0.5$, the Binomial distribution can be approximated by a Gaussian distribution.

2.4.3 Combination of errors

In many experimental scenarios, the outcomes involve analytical functions derived from measurable quantities. If a set of functions, denoted as $f_k(x_1, x_2, ..., x_m)$, depends on m distinct variables x_i, the covariance matrix for the function values, $\mathbf{\Sigma}_f$, can be computed using the matrix formula

$$\mathbf{\Sigma}_f = \mathbf{G}\mathbf{\Sigma}_x\mathbf{G}^T \tag{2.57}$$

with

$$G_{ki} = \left(\frac{\partial f_k}{\partial x_i}\right)\Bigg|_{\overline{x_1},\overline{x_2},...,\overline{x_m}}. \tag{2.58}$$

The resulting matrix $\mathbf{\Sigma}_f$ contains the variance of the results (function values) on the diagonal and the covariances between the results on the

off-diagonal elements. This is commonly referred to as *combination of errors* or *error propagation*. As an example, if a single function, $f(x, y)$, depends on two variables, x, y, the error on the function value is

$$\Delta f = \sqrt{\left(\frac{\partial f}{\partial x}\right)^2 \Delta x^2 + \left(\frac{\partial f}{\partial y}\right)^2 \Delta y^2 + 2\left(\frac{\partial f}{\partial x}\right)\left(\frac{\partial f}{\partial y}\right) \mathrm{cov}(x, y)}, \tag{2.59}$$

which is the commonly used notation for the combination of errors. The described method is valid for Gaussian errors and functions exhibiting weak curvature, allowing for a reliable approximation of the function as a line within the error intervals. If this is not the case, Monte Carlo simulations offer more accurate results.

2.4.4 Monte Carlo methods

Monte Carlo methods constitute a versatile and powerful class of computational techniques that rely on repeated random sampling to obtain numerical results. They are often used when analytical solutions are challenging or impossible [79] this approach is extensively used in statistics.

In this thesis, Monte Carlo simulations have played a crucial role in replicating the process of absorption imaging of quantum gases, which is discussed in Chapter 5. These simulations are used to estimate the technical noise contribution to the cloud parameters, such as the total atom number, the BEC atom number, the thermal atom number, and the temperature in situations where no analytical results are available.

Chapter 3

Experimental techniques

This chapter outlines the apparatus and experimental techniques used to produce and detect ultracold atomic clouds. The experimental setup described here reflects the configuration used to obtain the primary results of this PhD presented in Chapter 4 and Chapter 5. Experimental developments aimed at realizing EIT are treated in Chapter 6. The experimental setup was originally constructed by Jesper Fevre Bertelsen and Henrik Kjær Andersen under the supervision of Michael Budde starting in the spring of 2003, and the first BEC was produced in the spring of 2006. Much of the equipment from this period remains in use today, and thorough explanations of the design and the implementation are available in their respective theses from 2007 and 2008 [80, 81]. Subsequent modifications made up to the beginning of my own PhD are documented in the theses of

- Poul Lindholm Pedersen (2014) [82]
- Miroslav Gajdacz (2015) [83]
- Mick Althoff Kristensen (2018) [73]
- Mikkel Berg Christensen (2020) [84]

The chapter offers an overview of equipment already described in detail in the aforementioned theses while it delves deeper into aspects explored during this PhD, particularly focusing on absorption imaging.

The chapter is structured as follows: it begins with an overview of the setup and the experimental sequence. Following this, there is an introduction to the use of ^{87}Rb and a presentation of the laser setup. Next, techniques for cooling and trapping are examined. The chapter is rounded out by a comprehensive section on detection, with a focus on the setup, experimental techniques, and analysis of absorption imaging.

3.1 Experimental overview

The experiment is organized on two optical tables: a *laser table* and a *science table*. The laser table's primary function is to generate laser light with distinct frequencies essential for cooling and detecting atomic clouds. It is treated in more detail in Section 3.3. To prevent any undesired resonant light that might interact with the atoms and potentially disrupt the production of ultracold clouds, the laser table is physically separated from the *science table*, where the actual experiments on atom clouds are carried out.

To produce and study ultracold atomic clouds, it is crucial to isolate them from the environment using a vacuum setup, which is displayed in Fig. 3.1. Our setup contains two chambers, namely a MOT (magneto-optical trap) chamber consisting of a cylindrical glass cell and a science chamber, that are interconnected with tubes. Both chambers are continuously pumped using ion pumps.

The MOT chamber is used for the initial cooling and trapping of atoms. In this chamber, a magneto-optical trap captures clouds of approximately 10^9 ^{87}Rb atoms from a background vapor. The vapor

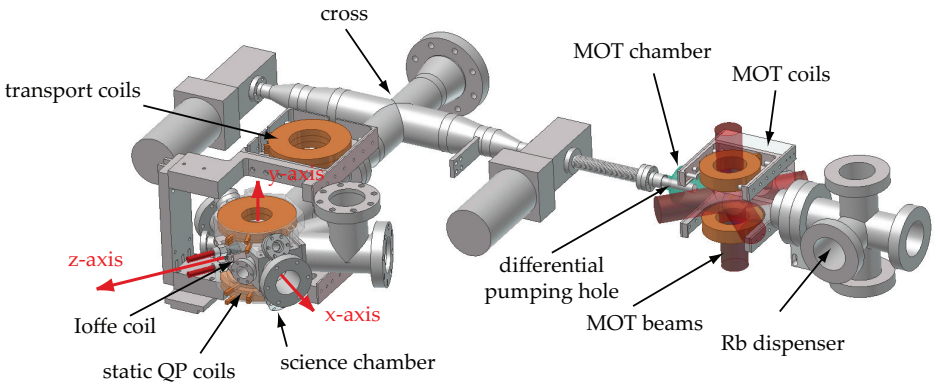

FIGURE 3.1: Overview of the vacuum chamber. Reprintet from [80].

is produced by passing a current through an alkali metal dispenser containing rubidium.

The atoms are transferred to a purely magnetic trap and transported to the science chamber using magnetic traps mounted on translational stages. The science chamber has a lower pressure than the MOT chamber, which increases the degree of isolation and the lifetime of the atoms in the trap. Here, the atomic cloud is transferred to an elongated Quadropole Ioffe-configuration (QUIC) trap [85].

The atoms are further cooled by forced radio-frequency (RF) evaporative cooling. With evaporative cooling, it is possible to cool the atomic clouds below the critical temperature where Bose-Einstein condensation is realized.

A special feature in the experiment is a step of atom number stabilization, before reaching the critical temperature for Bose-Einstein condensation, to a relative stability at the 10^{-4} level [86, 87]. This fixes the problem of technical preparation noise which typically is around 10 %.

To perform the final measurement the magnetic trap is abruptly

turned off, and the cloud expands in free fall. After a certain time of flight (TOF) the cloud is probed with resonant absorption imaging. From these images, density profiles of the cloud can be extracted, and cloud parameters can be determined.

The whole sequence of creating and detecting Bose-Einstein condensates has a cycle time of roughly 2 min. However, as the evaporation process was changed due to the implementation of a so-called hybrid trap and a dipole trap and the MOT improved, cycle time is down to roughly 30 s at the time of writing this thesis.

The experiment is entirely automated, with control and timing handled by the Experimental Control System (ECS). ECS features 48 digital outputs, controllable with a 1 µs time resolution, 32 16-bit analog outputs, controllable with a 50 µs time resolution, and 2 direct digital synthesizers (DDSs). The system is operating on a 10 MHz clock. Through the software interface of ECS, the user can construct the full experimental sequence, getting full control of all lab equipment. Details can be found in [81].

3.2 Rubidium 87

In our experiments ^{87}Rb is used as the atomic species for the investigation of cold atom clouds. The energy level scheme of the D_2 line ($5^2S_{1/2}$ to $5^2P_{3/2}$), which serves as the focal point for both laser cooling and detection, can be found in [88] along with other atomic properties. It is also indicated in Fig. 3.2. ^{87}Rb is recognized as an especially suitable element for experiments involving Bose-Einstein condensates [47], due to several key characteristics.

Firstly, ^{87}Rb has strong transitions in the visible or infrared region, where commercial lasers are available. This makes it ideal for laser cooling. Additionally, it has a low vapor pressure, and its intermediate mass ensures that atoms at room temperature have sufficiently low

speeds for effective capture by an MOT from background vapor [16], eliminating the need for devices like Zeeman slowers commonly employed for lighter atoms [89].

Furthermore, ^{87}Rb has a strong magnetic moment, a prerequisite for successful magnetic trapping. Its favorable ratio between elastic and inelastic collision rates allows for efficient evaporative cooling, ensuring that cooling processes are faster than heating effects [90]. In summary, ^{87}Rb possesses an almost ideal combination of properties for experiments involving ultracold gases [47].

On the other hand, one clear limitation of ^{87}Rb is the lack of known practically useful Feshbach resonances for controlling the interactions between the atoms [91]. Feshbach resonances are an essential tool in modern experiments with ultracold quantum gases and have led to significant advances in the creation of BECs across various elements and their subsequent use in diverse applications, such as simulators for condensed matter and few- and many-body physics [92].

3.3 Laser setup

The laser light required for the MOT and for detection is generated on the *laser table*, and subsequently transported to the *science table* via optical fibers. For the important experimental results of this thesis, two lasers were used – *the primary laser* and the *repumper laser*, generating the laser light illustrated in Fig. 3.2

The primary laser, a Toptica DL pro, serves multiple purposes, delivering light for Faraday imaging, absorption imaging, optical pumping, and cooling. It is locked 78.5 MHz below the $|F = 2\rangle$ to $|F' = 3/2\rangle$ cross-over peak in ^{87}Rb using Toptica's Digilock combined with a frequency modulation transfer spectroscopy setup [93, 94].

The laser light is divided into two branches. One branch seeds a tapered amplifier (TA) responsible for generating high-power light

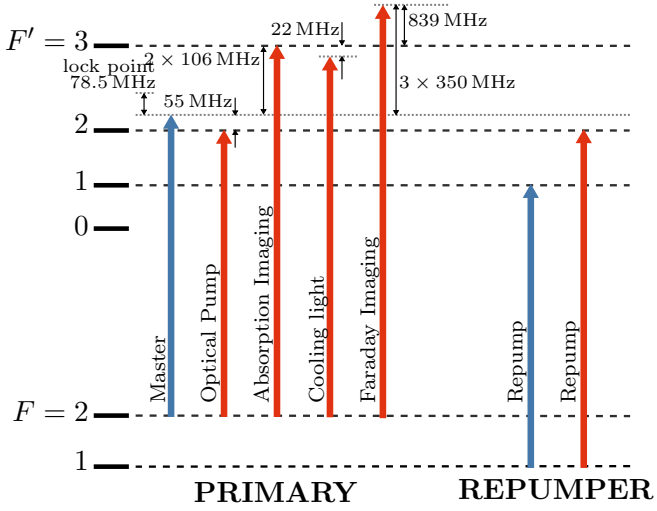

FIGURE 3.2: Illustration of the laser frequencies of the two lasers used in the experiments along with the level structure of ^{87}Rb. The locked laser frequencies are indicated with blue arrows, while the frequencies shifted by AOMs are indicated with red arrows. Adapted from [73]

.

($\approx$500 mW) for the laser cooling process. The other is used for imaging and optical pumping. This branch is first cleaned by a volume Bragg grating (VBG) to eliminate the broad background of spontaneous emission from the diode laser. Then, the light is split into the Faraday imaging, an absorption imaging, and a pump branch. The optical pump is used after the MOT stage to prepare atoms in a weak-field seeking state $|F = 2, m_F = 2\rangle$ for the magnetic trap. acousto-optical modulators (AOMs) in all branches facilitate rapid on-off switching of laser light while simultaneously shifting frequencies relative to the

locking point to achieve the desired frequencies.

A secondary laser called the *repumper laser*, following the design described in [95], generates repumping light, used to bring back atoms from the $|F = 1\rangle$ state. This is primarily used in the MOT but also proves to be a necessary tool in the science chamber for some experimental scenarios such as Stern-Gerlach experiments. It is locked through the use of frequency-modulated saturated absorption spectroscopy, achieved by modulating the current of the laser. The locking point is the $|F = 1\rangle$ to $|F' = 2\rangle$ transition.

3.4 Cooling and trapping

3.4.1 Magneto-optical trap

The first stage of the experimental sequence is the magneto-optical trap, a setup capable of both cooling and confining atoms. Using ^{87}Rb, the MOT can capture atoms directly from a background vapor. An illustration of the setup is given in Fig. 3.3. It consists of three orthogonal pairs of counter-propagating laser beams of relatively high intensity and circular polarisation. The light is red-detuned 22 MHz compared to the $|F = 2\rangle$ to $|F' = 3\rangle$ transition. This detuning ensures that atoms preferentially absorb photons traveling in the opposite direction to their motion. Consequently, upon photon absorption, the atoms receive a momentum kick in the opposite direction, resulting in a reduction of the temperature within the atomic cloud.

A weak magnetic quadrupole field is introduced by a pair of anti-Helmholtz coils. This field induces the linear Zeeman effect to create confinement, by causing atoms away from the center to become resonant, absorb photons, and get a momentum kick toward the center. During the cooling process, repumper light is employed to pump atoms that have transitioned to the $|F = 1\rangle$ state back to the $|F = 2\rangle$ state.

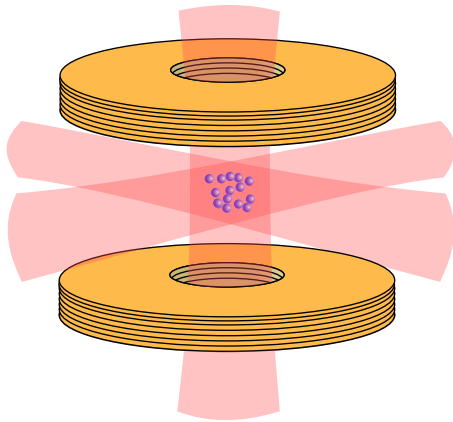

FIGURE 3.3: Illustration of setup for the magneto-optical trap (MOT).

The MOT is capable of capturing approximately 10^9 ^{87}Rb atoms in 10 s. Following the MOT, a compressed MOT (cMOT) is employed to prevent the introduction of potential energy to the cloud when transferring it to a purely magnetic trap. Typically, this step is succeeded by an optical molasses phase. However, the latter is absent in our laboratory due to the absent nulling of the Earth's magnetic field, for which bias coils have not been implemented.

For a comprehensive understanding of the MOT, refer to various textbooks such as [96, 97]. Details about the setup and the sequential timing in our lab, inspired by [98], can be found in [84].

3.4.2 Magnetic trapping

Following the MOT the atoms are confined by magnetic traps, which rely on the Zeeman effect. The potential energy in a spatially varying magnetic field $\vec{B}(\mathbf{r})$ is expressed as

$$U(\mathbf{r}) = \mu_{\mathrm{B}} g_{\mathrm{F}} m_f |\vec{B}(\mathbf{r})| = \mu |\vec{B}(\mathbf{r})|. \tag{3.1}$$

Here, μ_{B} is the Bohr magneton, g_{F} is the Landé g-factor, m_f is the hyperfine magnetic quantum number, and μ is the magnetic moment (not to be confused with the chemical potential). For the two ground states of ^{87}Rb, $|F = 2\rangle$ and $|F = 1\rangle$, g_{F} takes the values of $+1/2$ and $-1/2$, respectively. In the case of a quadrupole field generated by an anti-Helmholtz coil setup, the potential is given by

$$U(\mathbf{r}) = \mu B'(I)\sqrt{\frac{x^2}{4} + y^2 + \frac{z^2}{4}} + mgy, \tag{3.2}$$

where g is gravitational acceleration. An illustration of the coil configuration and the potential for different m_F levels can be seen in Fig. 3.4 (top). For the weak-field seeking hyperfine states ($\mu > 0$) such as $|F = 2, m_F = 1, 2\rangle$ and $|F = 1, m_F = -1\rangle$ Eq. (3.2) represents a confining potential with a minimum at the center. The gradient of this potential is directly proportional to the current, I, $B'(I) = C_B I$, where C_B is a constant determined by the coils' geometry. This constant can be estimated through theoretical models or measured, for instance, in levitation experiments with BECs, where the gradient that precisely counteracts gravity is determined.

When the atoms have been transported to the science chamber, they are transferred to QUIC trap [85], schematically shown in Fig. 3.4 (bottom). It is a modification of the QP trap by the addition of the so-called Ioffe coil that removes the zero point of the QP trap and forms a cigar-shaped harmonic potential:

$$V_{\mathrm{ext}}(x, y, z) = \frac{1}{2}m(\omega_\rho^2 x^2 + \omega_\rho^2 y^2 + \omega_z^2 z^2). \tag{3.3}$$

with the 2 radial trapping frequencies being much larger than the axial, $\omega_\rho > \omega_z$. In our case, the trapping frequencies are $\omega_r/2\pi \approx 300\,\mathrm{Hz}$ and $\omega_z/2\pi \approx 17\,\mathrm{Hz}$, when the 3 coils are connected in series. At the beginning of my PhD, however, we designed and implemented a setup capable of bypassing current from the QP coils in order to make the potential more spherical. This setup is presented in detail in [84].

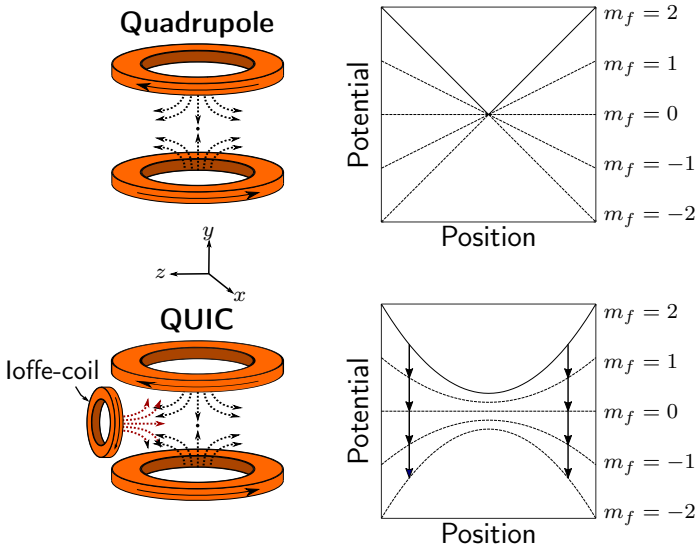

FIGURE 3.4: Coil arrangements for the quadrupole and QUIC traps, and the associated potentials for ^{87}Rb in the hyperfine states $|F = 2, m_F = -2 \rightarrow +2\rangle$. The arrows signify radio-frequency (RF) transitions occurring during the process of evaporative cooling. The figure is adapted from [73].

3.4.3 Forced evaporative cooling

In the QUIC trap, forced evaporative cooling is employed to cool atomic clouds by selectively removing high-energy atoms, thereby reducing the average energy of the remaining atoms. This removal of atoms is achieved using RF radiation, which induces a transition in their hyperfine spin state from the weak-field seeking $|F = 2, m_F = 2\rangle$ to a strong-field seeking spin state. In this spin state, the magnetic field becomes repulsive, leading to the expulsion of these atoms. The spin flips associated with this process are illustrated with arrows in the potential diagram for the QUIC trap shown in Fig. 3.4.

Systematic removal of high-energy atoms is accomplished through continuous adjustment of the RF radiation. This process begins with a high frequency and gradually decreases, ensuring that only the high-energy atoms situated farthest from the trap's center, experiencing the largest magnetic field and Zeeman splitting, are affected. The rate of the frequency sweep is chosen to be as fast as possible while still allowing sufficient time for continuous rethermalization and effective evaporation.

The RF radiation is generated by amplifying the signal from a direct digital synthesizer (DDS) and directing it to a quadrupole antenna located within the science chamber. This forced evaporative cooling method is capable of cooling the atomic cloud until the realization of Bose-Einstein Condensation at typically $\approx 100\,\mathrm{nK}$. At this point typically 10^5 to 10^6 atoms remained in the trap.

3.5 Detection

3.5.1 Imaging setup

Two detection techniques are implemented to probe the atomic cloud: A non-destructive method called Faraday imaging, used for atom number stabilization, and saturation absorption imaging for the final destructive measurement. Both methods make use of an optical setup[1] shown schematically in Fig. 3.5 a). It consists of two pairs of convex lenses and a camera. The camera is an Andor iXon Ultra 897, which is cooled to $-40\,^\circ\,^\circ\mathrm{C}$ to avoid thermal counts.

The first lens pair creates an intermediate image plane, which is imaged onto a CCD camera by the second lens pair. The second lens

[1] In fact, these two imaging methods use distinct axes and individual imaging setups, but due to their close resemblance, I elaborate solely on the setup for absorption imaging.

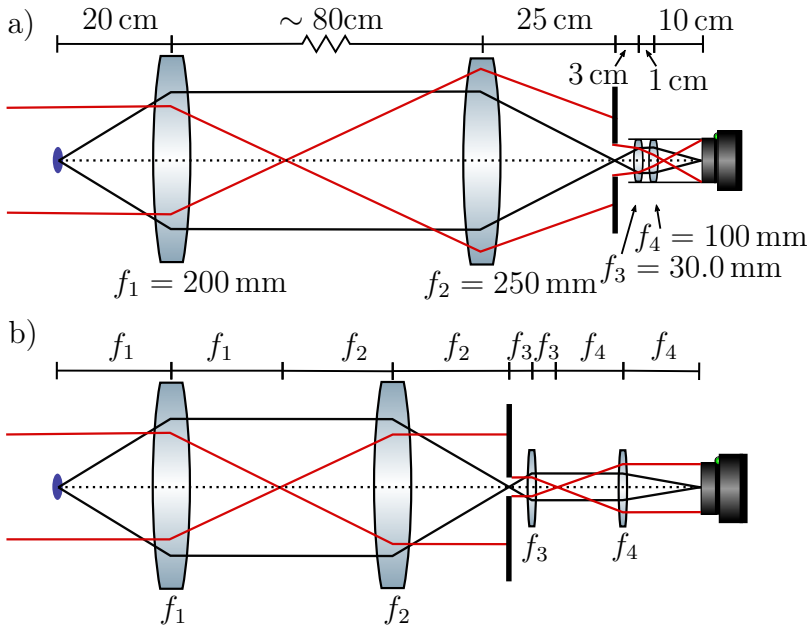

FIGURE 3.5: Illustration of our imaging system (a) and the equivalent setup in a $4f$ configuration (b). Blue ellipsis: a cloud of atoms being illuminated by imaging light. The imaging beam is shown with red lines and the diffracted image of the absorption with black lines. The imaging beam is trimmed by a razor blade aperture at the intermediate imaging plane. The figure is adapted from [84]

pair is positioned within a 1" tube mounted on the camera. In the intermediate plane, four razor blades trim the beam ensuring that only the desired light reaches the camera chip. This serves to prevent scattered photons from contaminating the image and reduces the impact of external stray light.

The total theoretical magnification is $M = \frac{25\,\mathrm{cm}}{20\,\mathrm{cm}} \frac{10\,\mathrm{cm}}{3\,\mathrm{cm}} = 4.2$. However, in practice, factors such as imperfect lens positioning may slightly

modify this magnification, resulting in a measured value of $M = 3.4$, determined from free fall experiments. The finite resolution due to diffraction, estimated using Rayleigh's criterion [99] is 3.8 µm, which is roughly the size of the pixel representation in the object plane. This is associated with a depth of field of ≈ 32 µm. The image size corresponds to approximately 2×2 mm in the object plane.

The lens pair setup in our configuration (Fig. 3.5 a)) deviates from the commonly employed $4f$ configuration [27]. In the standard $4f$ configuration, the lenses are positioned to create an image of the object while ensuring that the imaging beam is re-collimated after the second lens (and fourth lens). This is achieved by maintaining a distance between the object and the image of exactly $4f$, or if the focal lengths are different, $2f_1+2f_2$, as shown in Fig. 3.5 b). Using a setup where the imaging beam is not collimated after passing through a lens pair poses no issue since the cloud and the imaging are always magnified equally in the image plane. However, this setup might be more susceptible to imperfect focusing of the imaging.

3.5.2 Faraday stabilization

The Faraday stabilization setup combines non-destructive imaging with loss pulses of varying durations to precisely control the atom number [86, 87]. The experimental setup is shown in Fig. 3.6.

Before reaching condensation, the cloud is probed in-trap with linear polarized off-resonant light. The light is blue detuned by $\Delta = 1050$ MHz from the $|F = 2\rangle \rightarrow |F' = 3\rangle$ transition. The chosen polarization ensures that all light is reflected by a polarizing beam splitter (PBS) in the absence of atoms. However, in the presence of atoms, the Faraday effect - resulting from the interaction of light with spin-polarized atoms - causes a rotation of the polarization. This rotation allows some light to pass through the PBS and reach the camera. The rotation of the linearly polarized light is directly proportional to

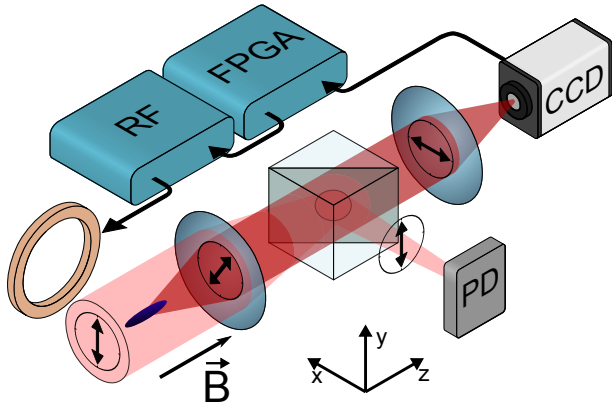

FIGURE 3.6: Faraday stabilisation setup. The figure is reprinted from [73].

the column density of the cloud, enabling the deduction of the atom number [87]. Real-time analysis of images is performed on a field-programmable gate array (FPGA), which controls an RF synthesizer and calculates the duration of a loss pulse required to expel atoms and achieve the desired atom number. The RF radiation for this is generated by amplifying the RF signal and directing it to the antenna in the vacuum chamber, which is also used for evaporation.

The sequence begins with 50 images, and their combined information provides an atom number estimate with sub-shot noise precision. This estimated atom number is then compared with a reference value, and the duration of a weak RF loss pulse is calculated. Subsequently, the feedback pulse is applied to the cloud, and an additional 20 images are captured to assess the success of the stabilization process.

3.5.3 Absorption imaging

At the end of the experiment, the atom cloud is probed using standard saturation absorption imaging. This technique involves illuminating the atoms with a laser beam and measuring the reduction of the light intensity with a CCD camera.

Before imaging, the cloud is released from the trap and allowed to undergo free fall for sufficiently long expansion times, enhancing the spatial resolution of the cloud and ensuring the optical density (*od*) drops to accessible values. Typically, the time-of-flight (tof) is between 15 and 35 ms.

To image the cloud, square pulses of resonant light, generated by AOMs, illuminate the cloud. The typical duration is $\tau = 30\,\mu s$, and the intensity in units of I_{sat} is typically at a level similar to the maximal optical depth (see Fig. 3.7). However, this rule of thumb is challenged in Section 3.5.6 . The imaging beam is a large collimated Gaussian beam with a diameter (to the e^{-2} point) of 7.5 mm, ensuring a near-homogenous intensity across the atom cloud. The imaging light is circularly polarized and resonant to the closed $|F = 2, m_F = 2\rangle$ to $|F' = 3, m_{F'} = 3\rangle$ D_2 transition.

As the imaging direction is perpendicular to the axis of the cigar-shaped QUIC trap, the magnetic field is rotated from orthogonal to parallel with the imaging direction to ensure that the laser light drives a σ^+-transition. This is passively achieved by maintaining a bias field in the imaging direction when turning off the trap, ensuring a well-defined spin orientation of the atoms.

The imaging sequence comprises a total of 6 images. First, an absorption image with atoms (probe) is acquired. Then, the atoms are optically pumped to the $|F = 1, m_F = 1\rangle$ state, rendering them transparent for subsequent images. This allows the acquisition of an image without atoms (reference) only 340 µs later, limited only by the camera shift speed. Two additional images are taken a few seconds later to

account for dark counts and background light, with all experimental settings identical to the first two images, however, without imaging pulses. Finally, after a few seconds, two more images without atoms are captured, identical to the probe and reference images, which are used for diagnostic purposes.

The images are matrices of photon counts converted to intensities in units of I_{sat} using the following formula for each pixel ℓ:

$$\begin{aligned}\tilde{I}_j^{(\ell)} = \frac{I_j^{(\ell)}}{I_{\mathrm{sat}}} = \frac{\mathcal{N}_{\gamma,j}^{(\ell)}\hbar\omega}{I_{\mathrm{sat}}\tau A} = \frac{\mathcal{N}_{\mathrm{el},j}^{(\ell)}}{\mathcal{T}\eta}\frac{\hbar\omega}{I_{\mathrm{sat}}\tau A} \\ = \frac{\mathcal{N}_{\mathrm{c},j}^{(\ell)}}{\mathcal{T}\eta g}\frac{\hbar\omega}{I_{\mathrm{sat}}\tau A} = C\cdot\frac{\mathcal{N}_{\mathrm{c},j}^{(\ell)}}{\tau},\end{aligned} \tag{3.4}$$

where the index j refers to the probe (p) or reference (0) image, I is the real intensity, ω is the angular imaging frequency, τ is the imaging pulse duration, A is the pixel area in the object plane, $\mathcal{T}$ is the transmission through the optical elements in the imaging system, η is the quantum efficiency of the camera chip, and g is the camera gain. The number of photons in the object plane, number of photo-electrons, and camera counts are denoted $\mathcal{N}_\gamma$, $\mathcal{N}_{\mathrm{el}}$, and $\mathcal{N}_{\mathrm{c}}$, respectively. The camera calibration factor is

$$C = \frac{\hbar\omega}{\mathcal{T}\eta g I_{\mathrm{sat}} A}. \tag{3.5}$$

The optical density and the column density $\tilde{n} = \int \mathrm{d}z\, n(z)$ for the ℓ's camera pixel are calculated using

$$od^{(\ell)} = \tilde{n}^{(\ell)}\sigma_0 = \alpha^* \ln\left(\frac{\tilde{I}_0^{(\ell)}}{\tilde{I}_{\mathrm{p}}^{(\ell)}}\right) + \tilde{I}_0^{(\ell)} - \tilde{I}_{\mathrm{p}}^{(\ell)}, \tag{3.6}$$

where σ_0 is the resonant scattering cross-section, $\alpha^* = \alpha\,(1 + 4\delta^2/\Gamma^2)$ is the calibration factor obtained from the methods described in Chapter 4, to account for some of the deficiencies of Eq. (3.6), which rely on

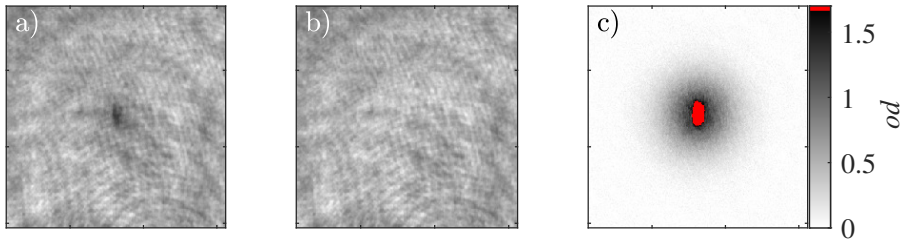

FIGURE 3.7: Example of probe image, a), reference image, b), and extracted optical density (od) for a partially condensed cloud.

simple assumptions for the light-matter interaction. Examples of the probe and reference image, along with the extracted optical density are shown in Fig. 3.7.

From these optical density profiles, atom numbers of the BEC and the thermal cloud as well as temperature can be extracted from fits described in Section 3.5.4, and the total atom number can be obtained by summing up all pixel values within a cloud region (CR)

$$N = \frac{A}{\sigma_0} \sum_{\ell}^{\mathrm{CR}} od^{(\ell)}. \tag{3.7}$$

3.5.4 CloudFit and the ultracoldImage class

Since nearly all information from individual experiments is derived from absorption imaging of clouds, visualization and fitting of density profiles are essential tools. Two main requirements for the imaging software are identified. Firstly, a Graphical User Interface (GUI) is needed to quickly visualize and fit clouds from single or small sets of runs and export the results for minor analyses. This is used on a daily basis for development and tests in the laboratory. Secondly, an

optimized fitting package in code format is required for larger analyses to gain speed and transparency in the analysis process.

In the spring of 2020, the large dataset for [2] was initially analyzed using a cloud fitting routine that lacked a visualization option. It was crucial for the analysis that all fits could be reviewed and any failures identified. On the other hand, a cloud fitting program with a GUI (SkyFit) was available, but the fitting process was integrated into the GUI, making it impossible to use the fitting routines independently. Additionally, the fitting routines needed for the large dataset were not available in SkyFit.

With this in mind, a decision was made to develop a new version of the fitting software package. This package would be independent of a GUI, but a GUI that uses the package was developed. This approach ensures that any changes in the fitting packages are automatically implemented in the GUI, ensuring standardization of all fitting work. Moreover, it should be straightforward to add new fitting routines, support for different atomic species, and compatibility with new image file formats for easy implementation in other laboratories.

The fitting packages were implemented as a MATLAB class, named ultracoldImage, while the GUI was developed as a MATLAB GUI named CloudFit. A screenshot of CloudFit is provided in Fig. 3.8. The code is available at
https://gitlab.au.dk/uqgg/programs/cloudfit.

Calibration parameters and column density

To convert the photon counts in the images to optical density, atom numbers, width, and temperature, several parameters must be specified in CloudFit's settings. First of all, a **camera calibration** given by Eq. (3.5) (in units of $I_{\mathrm{sat}} \cdot \mu$s/count) and the **detection time** are required to compute light intensities for each pixel from the photon count. Additionally, an **imaging calibration**, α^* should be provided

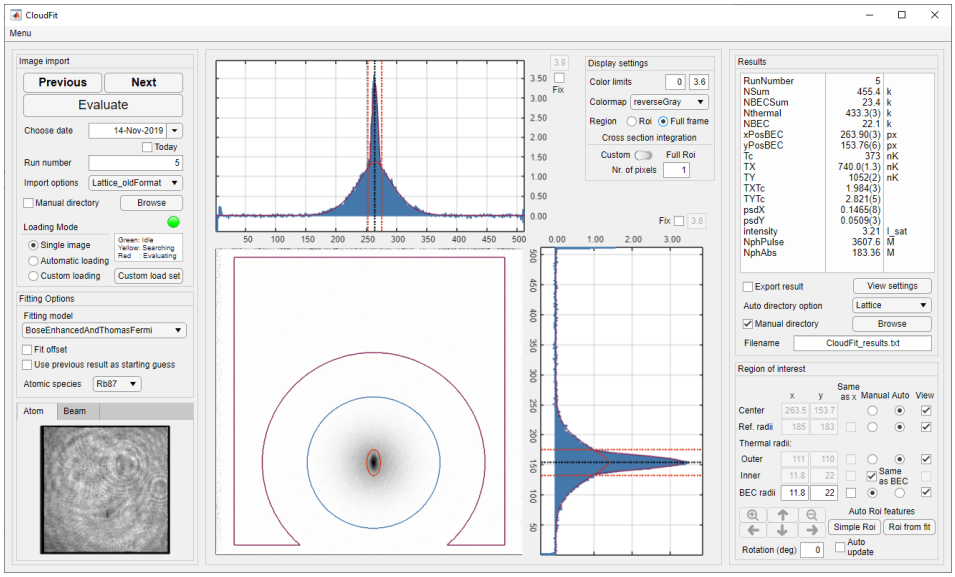

FIGURE 3.8: Screenshot of the CloudFit GUI. On the main image optical depth (*od*) is shown with a black-and-white color map. The ROI consists of a reference region (purple line), a cloud region (blue ellipsis), and a BEC region (red ellipsis). The side panels show the *od* signal for a single row (and column) going through the center of the cloud. In the left panel, the cloud to be loaded and the fitting model is chosen. In the upper right panel the results of the fits are shown and are optionally exported. In the lower right panel ROI settings are specified. A dynamic demonstration is available in the git repository.

as a global parameter or as a slope, α', and offset, α_0 (see Chapter 4). The **cross section** of the imaging transition and the **pixel size** (in the imaging plane) are necessary. Finally, the **mass** of the atomic species, the **trapping frequencies**, and the **time of flight** are needed to calculate the temperature from the width of the thermal cloud.

Region of interest

Before fitting the density profile, the relevant region in the image must be specified with a region of interest (ROI), which comprises three subregions. The blue region (cloud region) in Fig. 3.8 is adjusted so that all atoms are contained within it, while the red region (BEC region) is adjusted to encircle the entire BEC. Additionally, a reference region without atoms or razor blades must be specified, corresponding to the purple region. This is used to compensate for any intensity variations between the image with and without atoms.

Parameter estimation

Four different fit options are preinstalled: A Maxwell-Boltzmann fit or Gaussian fit (Eq. (2.38)), a low-temperature Bose-enhanced Gaussian fit or *maximally peaked BE fit* (Eq. (2.39)), a pure Thomas-Fermi fit (Eq. (2.43)), and finally, a combination of the *maximally peaked BE fit* and a Thomas-Fermi fit. Here, Eq. (2.39) is used to fit the wings of the cloud (the region between the blue and red ellipses in Fig. 3.8), and the resulting fit is extrapolated and subtracted in the BEC region before a Thomas-Fermi fit is performed to the remaining signal. Technically, the fitting process utilizes the MATLAB function *fitnlm*, which is a shell around the *nlinfit* function, by default employing a non-linear least-square estimation.

In addition to the atom numbers obtained from fits, the software also calculates the total number of atoms corresponding to the entire signal within the cloud region using Eq. (3.7).

3.5.5 Thermal fit including fugacity

As discussed in Section 2.3, the two standard fitting functions for thermal distributions available in CloudFit (Section 3.5.4) represent

the low-temperature and high-temperature limits of Eq. (2.37), which provides a more accurate description of the distribution for temperatures just above the critical temperature. However, directly employing Eq. (2.37) as a fitting function is challenging due to its tendency to become trapped in local minima. Nevertheless, by reducing the number of parameters, this issue can be circumvented, resulting in a fitting function that more accurately determines the temperature in this regime.

Equation (2.37) can be considered a fitting model with the parameters, N_{th}, T, c_x, c_x. However, N_{th} can be derived by summing up the entire signal within the cloud region. Utilizing a radius of the cloud region at $3\,w$, with w being the width of Eq. (2.38) or (2.39), roughly underestimates the atom number by 3%, while extending it to $3.5\,w$ reduces the underestimation to below 1%. This, on the other hand, also introduces significantly more statistical noise. Thus, a reasonable compromise between systematic and statistical errors is achieved by selecting a cloud width of $3.25\,w$. Additionally, the coordinates of the cloud center are precisely determined by a Gaussian fit.

After inserting these parameters, the reduced chemical potential $\overline{\mu}(N_{\mathrm{th}}, T)$ becomes a function of temperature alone, determined by numerically solving Eq. (2.13). Similarly, the width, w_i, given by Eq. (2.36) can also be regarded as functions of the temperature. Consequently, the full expression, Eq. (2.37) now solely depends on temperature, which can be emphasized by rewriting it as

$$od_{\mathrm{BE}}(x,y) = \frac{N_{\mathrm{th}}\sigma_0}{2\pi w_x(T) w_y(T) g_3(\exp[\overline{\mu}(N_{\mathrm{th}},T)])} \cdot g_2\left[\exp[\overline{\mu}(N_{\mathrm{th}},T)] \exp\left(-\frac{(x-c_x)^2}{2w_x(T)^2} - \frac{(y-c_y)^2}{2w_y(T)^2}\right)\right]. \quad (3.8)$$

Here, it is expressed as optical density by multiplying with the resonant scattering cross-section, σ_0. Fits with this model are here denoted *general BE fits*.

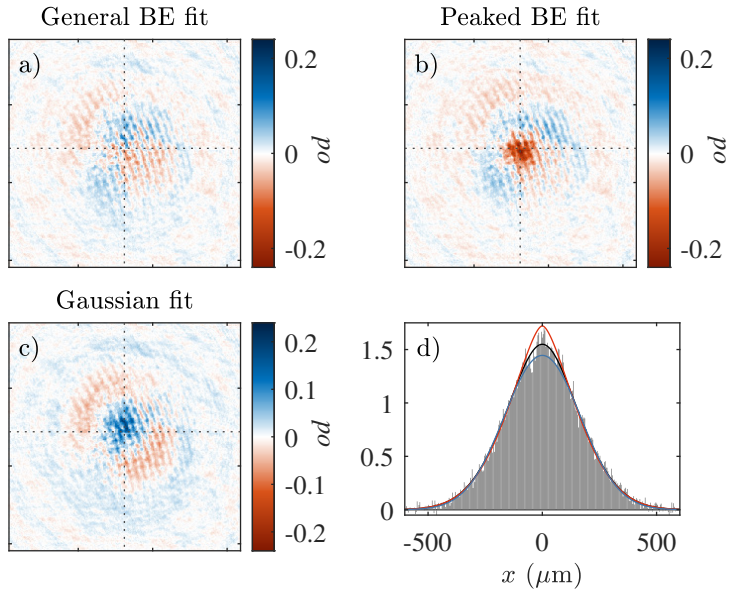

FIGURE 3.9: Averaged residual of fits to 60 identical clouds at a temperature of $T/T_c^0 = 1.09$ using Eq. (3.8) (a), Eq. (2.39) (b), and Eq. (2.38) (c) as fitting models. In d) a cross-section through the center of the optical density profile of a single cloud is shown in grey. The lines are the fits to Eq. (3.8) (black), Eq. (2.39) (red), and Eq. (2.38) (blue).

To demonstrate the fitting process, it is applied to all clouds above the critical temperature in the dataset used in Chapter 5. Details about the cloud production can be found there. Importantly, sets of 60 identical clouds are prepared at same temperature, with distinct temperatures for each of the 5 sets prepared above the critical temperature. The averaged residual of 60 *general BE fits* within a particular set is demonstrated in Fig. 3.9 a). Additionally, the average residual of the *maximally peaked BE fit* (Eq. (2.39)) is plotted in b), and the

average residual of Gaussian fits (Eq. (2.38)) in c). A cross-section of the density profile (d) for a single cloud is also shown as an example with the three different fits applied.

The *maximally peaked BE fits* overestimate the peak *od*, whereas Gaussian fits underestimate it. Despite the improved residual of the *general BE fit*, some systematic effects remain in the image. The observed linear fringes, present only at the positions of atoms, are assumed to be diffraction caused by astigmatism in the imaging setup. Several factors could contribute to the remaining concentric structure. These include systematic errors in the atom number estimated from summation inserted in Eq. (3.8), the fact that the cloud is only partially in focus (the depth of field is smaller than the cloud), and distortion of the cloud caused by photon kicks as discussed further in Section 3.5.6 and Section 4.2. Importantly, the improved fit facilitates the observation of more subtle features in the residuals. In d), the cross-section clearly illustrates how Eq. (3.8) has the flexibility to represent distributions between the two limiting cases of a *maximally peaked BE fit* and a Gaussian fit.

The obtained temperatures are compared to those obtained by the *maximally peaked BE fit* and the Gaussian fit for all 5 sets of 60 clouds. The result is shown in Fig. 3.10 a). Atom numbers extracted from the *maximally peaked BE fit* and Gaussian fit are compared to those obtained by summation in b). The temperature spread within each set of 60 clouds, evaluated according to the methods described in Section 5.1.3 is shown in c) for each of the three fits. Finally, in d) the obtained reduced chemical potential is plotted to provide intuition for this.

The temperature extracted from the *maximally peaked BE fit* agrees with the general Bose-enhanced fit around T_c^0, but worsens as the temperature increases with the systematic error being above 5 % already at $T/T_c^0 = 1.1$. The opposite is true for the Gaussian fit which is worst around T_c^0 and becomes more accurate towards higher temperatures.

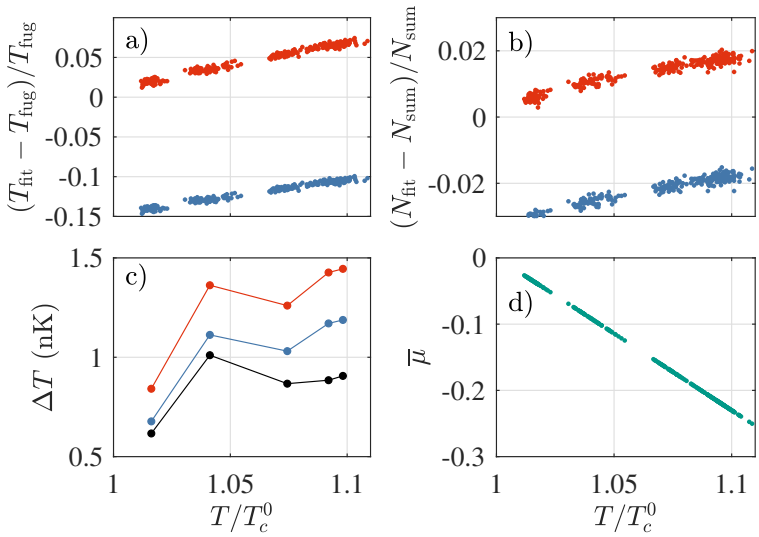

FIGURE 3.10: Comparison of the *maximally peaked BE fit* (red) and the Gaussian fit (blue) to the *general BE fit* as a function of temperature. Systematic deviations are shown for temperature (a) and atom number (b). The temperature spread (standard deviation) is plotted in c), with the black line indicating the spread of *the general BE fit*. Error bars have been omitted for clarity. In d), the reduced chemical potentials are plotted.

A similar trend is observed for the atom number.

The temperature spread is lowest when using the *general BE fit*, slightly higher for the Gaussian fit, and highest for the *maximally peaked BE fit*. Therefore, the *general BE fit* enhances both the precision and accuracy of the temperature estimation.

3.5.6 Error analysis of od

This section treats the errors in optical density in each pixel caused by photon shot noise and examines the impact on the estimation error for the total atom number. These considerations can guide the selection of the optimal imaging intensity and duration. Additionally, they provide essential input for the analysis of estimation errors related to the BEC, thermal, and total atom number as well as temperature in Chapter 5. Similar results are presented in [49].

The pixel uncertainties are obtained by applying error propagation (Eq. (2.57)) to Eq. (3.6), resulting in [36]

$$\Delta od^{(\ell)} = \sqrt{\left(\frac{\partial od}{\partial \tilde{I}_0}\right)^2 \left(\Delta \tilde{I}_0^{(\ell)}\right)^2 + \left(\frac{\partial od}{\partial \tilde{I}_\mathrm{p}}\right)^2 \left(\Delta \tilde{I}_\mathrm{p}^{(\ell)}\right)^2} \tag{3.9}$$

Here, Δ denotes the standard deviation of the quantities. The partial derivatives in Eq. (3.9) are both given by:

$$\left(\frac{\partial od}{\partial \tilde{I}_j}\right)^2 = \left(\frac{\alpha^*}{\tilde{I}_j} + 1\right)^2 \tag{3.10}$$

with the index j referring to the probe (p) or reference (0) image. The noise contribution to $\Delta \tilde{I}_j$ can be divided into photon shot noise and camera noise, where the latter includes photo response non-uniformity and read noise such as dark current effects, sense node reset noise, source follower noise and ADC quantization noise. [38]. Simple assumptions for the camera noise are employed in Section 5.2.1, but in this section shot noise alone will be treated.

The shot noise is easily implemented from Eq. (3.4), using the spread of the Poisson distribution for the photo-electrons $\Delta \mathcal{N}_\mathrm{el}^{(\ell)} =$

$\sqrt{\mathcal{N}_{\mathrm{el}}^{(\ell)}}$ yielding [50]

$$\Delta\tilde{I}_j^{(\ell)} = \frac{\sqrt{\mathcal{N}_{\mathrm{el}}^{(\ell)}}}{\mathcal{T}\eta}\frac{\hbar\omega}{I_{\mathrm{s}}\tau A} = \sqrt{\tilde{I}_j^{(\ell)}}\sqrt{\frac{1}{\mathcal{T}\eta}\frac{\hbar\omega}{I_{\mathrm{s}}\tau A}}. \tag{3.11}$$

Overall, Eq. (3.9) with Eq. (3.10) and Eq. (3.11) inserted characterizes the error in *od* from photon shot noise in a single pixel. When considering an entire image, the expected estimation error of the total atom number (calculated from Eq. (3.7)) is

$$\Delta N = \frac{A}{\sigma_0}\sqrt{\sum_{\ell\in\mathrm{CR}}\left(\Delta od^{(\ell)}\right)^2}, \tag{3.12}$$

where the sum is over the entire cloud region.

To explore the minimization of Eq. (3.9) and Eq. (3.12), $\tilde{I}_{\mathrm{p}}$ is expressed as a function of $\tilde{I}_0$ and *od*. This is achieved using the Lambert W function [100] facilitating to express the intensity of the transmitted as [101]

$$\tilde{I}_{\mathrm{p}}(\tilde{I}_0, od) = \alpha^* W\left[\frac{\tilde{I}_0}{\alpha^*}\exp\left(\frac{\tilde{I}_0 - od}{\alpha^*}\right)\right]. \tag{3.13}$$

Henceforth, the index ℓ is dropped. Equipped with this expression, optimal imaging conditions can be investigated.

Transmission, quantum efficiency and pixel area

A couple of key observations appear initially. First, from examining Eq. (3.11) it becomes clear that having a high transmission, $\mathcal{T}$, in the imaging setup and a high quantum efficiency, η, on the camera is always advantageous. Secondly, when combining Eq. (3.12), (3.9) and (3.11) it can be shown that $\Delta N \propto \sqrt{A}$. This suggests that reducing the pixel area by increasing the magnification of the imaging

setup suppresses noise. However, this dependency is compensated by an increasing number of pixels in the cloud region, rendering the estimation error of atom number independent of the pixel area and magnification [50].

Optimal imaging intensity

To gain insight into the contributions to Eq. (3.9) from the reference and probe images Eq. (3.10), (3.11) and (3.13) are combined to reveal

$$\Delta od_0(\tilde{I}_0) = K\left(\frac{\alpha^*}{\sqrt{\tilde{I}_0}} + \sqrt{\tilde{I}_0}\right) \tag{3.14}$$

$$\Delta od_\mathrm{p}(\tilde{I}_0, od) = K\left(\frac{\alpha^*}{\sqrt{\tilde{I}_\mathrm{p}(\tilde{I}_0, od)}} + \sqrt{\tilde{I}_\mathrm{p}(\tilde{I}_0, od)}\right) \tag{3.15}$$

with $K = \sqrt{\frac{1}{\mathcal{T}\eta}\frac{\hbar\omega}{I_\mathrm{s}\tau A}}$. For the visualization of Eq. (3.14) and (3.15), typical parameters from our lab have been assumed: $\mathcal{T} = 0.94$, $\eta = 0.68$, $\tau = 30\,\mu\mathrm{s}$, $A = 14.4\,\mu\mathrm{m}^2$ and $\alpha^* = 1.5$. Additionally, for specific cases, the optical density is set to $od = 3$ as an example.

In Fig. 3.11 a) Δod_0 (solid line) is plotted along with the contribution of the first (dotted line) and second term (dashed line) of Eq. (3.14). The equivalent is shown for Δod_p in b). The decreasing $1/\sqrt{I}$ behaviour of the first terms arises from the logarithmic term in Eq. (3.6), reflecting the decrease in the relative error of Poisson noise for higher mean values of the photon counts. On the other hand, the $\sqrt{I}$ behaviour arising from the saturation term in Eq. (3.6) is an increasing function of the intensity, leading to a minimum when combined. For the reference image, the minimum is at $(\tilde{I}_0)_{\mathrm{min},0} = \alpha^* = 1.5$, while for the probe image (having lower intensity), the minimum is shifted upwards to $(\tilde{I}_0)_{\mathrm{min,p}} = 3.3$. The combined error of the reference

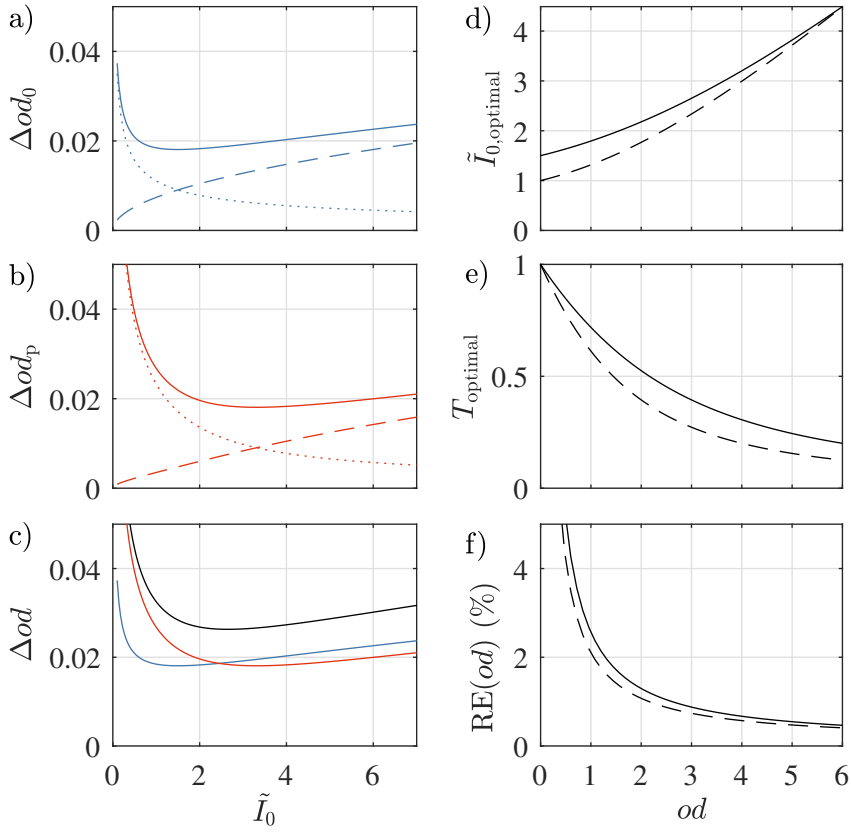

FIGURE 3.11: This figure provides insights into imaging intensities that minimize the impact of photon shot noise in absorption images. In the left column, the contributions to *od* pixel errors are plotted as a function of imaging intensity, $\tilde{I}_0$, for the reference image in blue (a), the probe image in red (b) and their combination in black (c). Additional details can be found in the main text. In the right column, the optimal imaging intensity (d) and the optimal transmission (e) are plotted as a function of *od*. In f), the relative error $\Delta od/od$, when using the optimal imaging intensities, is plotted against *od*. The left column includes results for $\alpha^* = 1.5$ (solid lines) and $\alpha^* = 1$ (dashed lines).

and probe image is shown in Fig. 3.11 c) (black), where Δod_0 (blue line) and Δod_p (red line) are also included. The combined error has a minimum at $(\tilde{I}_0)_\mathrm{min} = 2.6$. Notice that the error increases sharply towards low intensities, while it remains relatively flat towards high intensities; thus, the penalty for choosing a too low intensity compared to the optimal intensity is greater than the opposite.

In the right column of Fig. 3.11 solid lines represent results for $\alpha^* = 1.5$, and dashed lines represent those for $\alpha^* = 1$. The optimal imaging intensity can be determined for various *od* values as shown in Fig. 3.11 d). Another approach to consider is aiming for an optimal transmission, depicted in e) as a function *od*. Notably, this analysis reveals no universal constant fraction for optimal transmission. Finally, in f), the relative error when using the optimal imaging intensity (given by d)) is plotted against *od*. This is a decreasing function of *od*, showing that the best precision for *od* and atom numbers is obtained for narrow, dense clouds (at the expense of spatial resolution). While this comparison might seem unfair since increasing intensity while keeping imaging duration fixed leads to a higher number of absorbed photons per atom, even after compensating for this factor, the qualitative conclusion remains valid.

Imaging duration

At first sight, the situation is simpler for the imaging duration, τ. Equation (3.11) indicates that increasing the imaging duration reduces the error on the intensity and consequently, the optical density. However, this truth is nuanced, as increasing the imaging duration and the number of absorbed photons per atom, $\overline{N}_\mathrm{abs}$, introduces systematic effects. First, in time-of-flight measurements, vertical movement during imaging must be restricted to avoid vertical smearing. Secondly, the dynamic range of the camera pixels should not be exceeded. In our camera, this limit is 16 bits, corresponding to $2^{16} - 1 = 65535$ counted

photons.

Additionally, several effects are associated with the number of absorbed photons per atom. The imaging process induces a gradual acceleration of atoms due to momentum kicks from the probe beam, leading to the cloud being pushed out of the focus plane [36]. Moreover, this movement introduces a Doppler shift that effectively detunes the imaging light. The recoil kicks of the reemitted photons cause a random walk of the atoms and diffusion of the cloud during imaging [36]. Hence, it would be natural to impose a restriction on the $\overline{N}_{\mathrm{abs}}$.

In Fig. 3.12 the Δod landscape is shown as a function of both $\tilde{I}_0$ and τ for the case of $\alpha^* = 1.5$ and $od = 3$. Exemplified restrictions on the imaging duration, number of absorbed photons per atom and camera depth are also plotted. For instance, requiring $\overline{N}_{\mathrm{abs}} < 400$ and d $\tau \leq 30\,\mu\mathrm{s}$, the red circle indicates the optimal imaging intensity and duration for $od = 3$.

Full cloud example

Until now the optimal imaging conditions have been discussed for a specific optical density for a single pixel. However, real optical density profiles contain a range of od values. Here, the overall optimal imaging intensity for estimating the total atom number in a typical bimodal cloud is examined. In this example (see Fig. 3.13 a)), a cloud is constructed with $N_{\mathrm{th}} = 550 \times 10^3$ atoms in the thermal cloud and $N_0 = 40 \times 10^3$ atoms in the BEC, reaching a maximum optical density $od \approx 4$. The cloud region (white circles) specifying the pixels to be included in the estimations of the total atom number, has a radius of 3 thermal cloud widths. The pixel errors, Δod, are shown in b). Here, the optimal imaging intensity ($\tilde{I}_{0,\mathrm{optimal}} = 1.59$) has been used. It is extracted from c), where the error on the total atom number, calculated using Eq. (3.12), is plotted as a function of $\tilde{I}_0$.

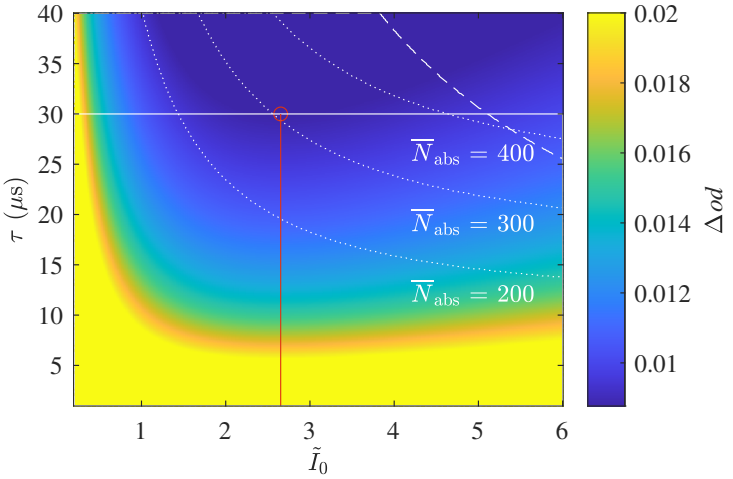

FIGURE 3.12: *od* pixel error as a function of both imaging intensity, $\tilde{I}_0$, and imaging duration, τ assuming $\alpha^* = 1.5$ and $od = 3$. The solid white line denotes an exemplified restriction of $\tau = 30\,\mu\mathrm{s}$. The dotted white lines represent $\overline{N}_{\mathrm{abs}} = 200$, 300, 400, while the dashed white line represents the limit of a 16-bit camera depth. The red line shows the optimal intensity for each imaging duration. Moreover, the red circle indicates the optimal imaging intensity and duration when requiring $\overline{N}_{\mathrm{abs}} \leq 400$ and $\tau \leq 30\,\mu\mathrm{s}$

In an image like the one depicted in Fig. 3.13 a), there is a clear overweight of pixels revealing a low *od*. Consequently, despite a maximum *od* of approximately 4 in the image, the optimal imaging intensity for minimizing the estimation error of the total atom number is just above the lower limit for optimal intensity for $od \to 0$, $\tilde{I}_0 = \alpha^*$. And this is significantly lower than the optimal intensity for the peak *od*. Even with $\tilde{I}_0 = 1.59$, there are still a few thousand photons transmitted per pixel at the maximum *od*, ensuring that the image remains unsaturated. In this scenario, the relative estimation error of the total

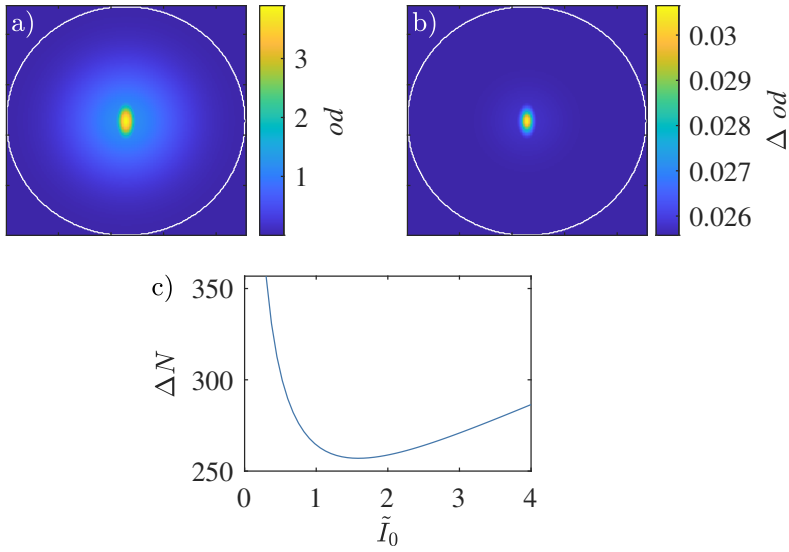

FIGURE 3.13: For a typical optical density profile shown in a) the errors in each pixel are shown in b). The error on the total atom number calculated from Eq. (3.12) including all pixels within the cloud region (white circles in a) and b)) is plotted as a function of imaging intensity in c).

atom number is $\Delta N/N = 257/(590 \times 10^3) = 4.4 \times 10^{-4}$. Additionally, it's noteworthy that for a cloud like this, using the specified imaging intensity, the error Δod in the wings of the cloud remains nearly constant. This characteristic is utilized in Chapter 5.

It is worth emphasizing that while ΔN does not exhibit high sensitivity to the imaging intensity, keeping $\tilde{I}_0$ low offers additional advantages. These include a reduction in $\overline{N}_{\mathrm{abs}}$ and the associated side effects such as diffusion, out-of-focus distortions, and the creation of an effective detuning, as discussed earlier. Consequently, opting for this optimal imaging intensity enhances both precision and accuracy

compared to the rule of thumb outlined in Section 3.5.3.

Finally, it is important to highlight that when dealing solely with the estimation of the total atom number, and spatial resolution isn't a priority, employing a shorter time-of-flight duration can significantly reduce the number of pixels involved in the estimation. This reduces the estimation error on N quantified by Eq. (3.12). Moreover, it leads to a higher average *od*, thereby enhancing the signal-to-noise ratio, as illustrated in Fig. 3.11 f). Consequently, an overall improvement in precision is achieved. Of course, it is essential to ensure that the cloud is sufficiently dilute to allow for some transmission of the imaging pulse. On the other hand, imaging high optical densities might introduce problems with systematic errors, as discussed in Chapter 4.

The detuning of the imaging frequency implicitly entering α^* in Eq. (3.6) has been ignored in this treatment. This decision was based on the observation that a frequency precision of, for instance, 100 kHz due to the laser lock, has a negligible impact on the individual pixel value. However, upon reviewing this section, I realized that since all pixels experience the same detuning within an image, these small contributions are likely to accumulate and introduce significant noise into the total atom number. A detailed examination of this phenomenon would be a natural extension of the analysis presented in this section.

Indeed, following the submission of this thesis, I discovered that the precision of our laser lock, measured to be 160 kHz*, often constitutes the predominant factor contributing to the estimation error of the total atom number. Mitigating the effect of laser frequency uncertainty is achievable by increasing the imaging power and invoking power broadening of the imaging transition. Thus, the optimal imaging intensity for the particular cloud discussed in this section (when neglecting the limitations shown in Fig. 3.12) is, in fact,* $\tilde{I}_0 > 10$*. Some details on this effect can be found in [3].*

3.5.7 Focus of the imaging setup

Focused imaging setups are crucial for obtaining accurate estimates of cloud parameters through absorption imaging. Our imaging system has a finite resolution due to diffraction, which corresponds roughly to the length represented by one camera pixel (3.8 µm). This is associated with a depth of field of $\approx 32\,\mu m$, stressing the necessity for precise focusing methods.

Usually, systems are focused by minimizing the size or reducing apparent diffraction effects of a compact object, such as a BEC. However, this approach does not always provide a well-defined determination of the focus plane and requires the presence of a BEC. Here, a method is introduced that achieves modest precision in determining the focus plane (around $30 - 40\,\mu m$) in a straightforward deterministic manner on a thermal cloud. This method is a refinement of techniques outlined in [81]. While it does not achieve the same precision as the 2 µm achieved in [35], it is arguably simpler to implement.

The method relies on the principle that the refractive index changes across an atomic resonance [102]. When the imaging light is red-detuned, the refractive index is above unity, causing an atomic cloud to act as a confining lens. Conversely, using blue-detuned light, the refractive index drops below unity, transforming the cloud into a spreading lens. This illustrated in Fig. 3.14.

Probing the atoms using absorption imaging has the following consequences. If the imaging light is blue-detuned and the focus plane of the imaging setup is positioned behind the atoms (relative to the direction of the light), the unabsorbed light is dispersed, resulting in more photons being removed from the central part of the probe beam than expected from absorption alone. Consequently, the interpreted density profile appears denser and narrower. Conversely, if the focus plane is in front of the atoms, the dispersed light from the atomic lens ends up at the center of the cloud on the camera. In this case, fewer

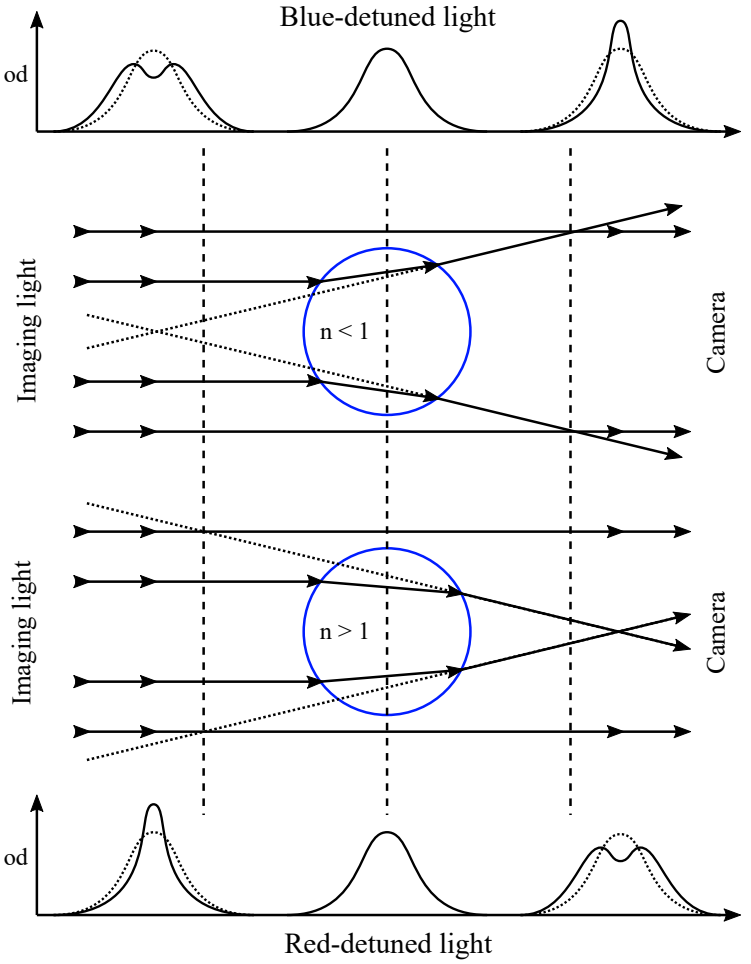

FIGURE 3.14: The effect on the density profile obtained by absorption imaging when using blue-detuned (top) and red-detuned (bottom) imaging light. The effect is shown for the object plane (dashed line) of the imaging setup being in front of, behind, and at the center of the atomic cloud. The figure is reproduced from [81].

photons than expected from absorption are removed from the central part of the probe image, leading to a lower and broader interpreted density profile. It is even possible for density profiles to resemble a doughnut shape.

Employing red-detuned light yields opposite consequences. A focus plane situated behind the atoms results in a lower and broader interpreted density profile, whereas a focus plane positioned in front of the atoms leads to a denser and narrower density profile. If the focus plane is positioned at the center of the cloud, using detuned imaging light should not affect the density profile. Therefore, at this point, the width obtained using red- and blue-detuned imaging light is the same.

Experimental implementation

The camera is mounted on a translational stage equipped with a micrometer adjuster. The second lens pair is affixed to the camera within a tube, ensuring that it moves with the camera chip. Once the imaging setup is approximately focused, the resonance is determined by identifying the imaging frequency that maximizes the signal during absorption imaging.

Using imaging light with a detuning of $\pm 14\,\mathrm{MHz}$, a thermal cloud is imaged at various camera positions around the approximate focus. For each camera position, the cloud is probed three times using red-detuned light and three times using blue-detuned light. The horizontal (X) and vertical (Y) widths, obtained from Gaussian fits to the density profiles, are plotted against the camera position, d_{camera}, as shown in Fig. 3.15. The widths are fitted using 3rd-order polynomial fits.

The intercepts of the polynomials for the width obtained using red- and blue-detuned light is interpreted as the focus points. These are determined numerically to be $d_x = 18.16(5)\,\mathrm{mm}$ for the horizontal direction and $d_y = 14.96(4)\,\mathrm{mm}$ for the vertical direction. The errors

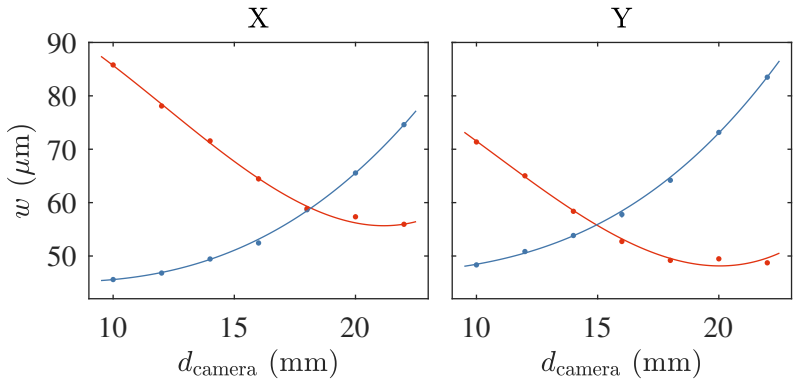

FIGURE 3.15: Horizontal (X) and vertical (Y) widths of Gaussian fits to the density profiles obtained with 14 MHz red-detuned (red points) and blue-detuned (blue points) imaging light as a function of the camera position. The red lines and blue lines are 3rd-order polynomial fits to red points and blue points, respectively. Note that error bars are included for the widths, although they are too small to be visible.

are calculated by repeatedly estimating the interception when resampling the fitting parameters (treated as stochastic variables) based on the most probable fit values and the covariance matrix. Thus, the precision (1 standard deviation) of the focus plane is approximately $40-50\,\mu$m. Considering the magnification of $M = 5/4$ from the object plane to the intermediate imaging plane, this corresponds to a precision of $30-40\,\mu$m in the object plane. For typical expanded cloud sizes (6 w) of $0.5-1.1$ mm, this is a reasonable precision. The focus precision could likely be improved by using smaller clouds or BECs, though in this case preparation noise might be a limiting factor.

Unexpectedly and regrettably, this specific measurement reveals astigmatism in the imaging setup, as the horizontal and vertical dimensions have different focus planes. This is confirmed by observing

that while placing the camera at the position to achieve focus in the horizontal direction, no diffraction patterns are observed in this dimension when imaging a small BEC. However, such patterns are observed in the vertical direction. This stresses the importance of ensuring that optical elements are centered on the imaging light and that tilted lenses are avoided.

Chapter 4

Spatial calibration of high-density absorption imaging

The following chapter is based on the paper [1] of which I am the first author. While the majority of the content, including text and figures, remains unchanged from the original paper, a few formulas already presented in Section 3.5.3 have been omitted along with the outlook section, which will be addressed in the conclusion of this thesis. I was involved in conducting the experiment, analyzing the data, and contributing to the writing of the paper.

Our research aimed to enhance a widely used calibration technique for absorption imaging, as introduced by Reinaudi et al. [31]. This technique, initially proposed for dilute clouds, has become common in the study of dense clouds. We questioned its applicability as a fixed calibration coefficient indepedent of the local optical density, and we had noticed variations in calibration coefficient across different experiments, as also outlined in Veyron et al. [30], who achieved similar results. Our objective was to extend the findings of Reinaudi et al. to denser cloud conditions, similar to those encountered in our experiments, investigating any potential dependencies of the calibra-

tion value on optical density. The ultimate aim was to enhance the accuracy of estimated atom number and temperature.

4.1 Introduction

The accurate measurement of the atom numbers and temperatures of clouds of ultracold atoms is rife with complications, both in the case of dilute mesoscopic samples and for samples at high densities. In almost all cases, detection relies on optical methods which can be divided broadly, in resonant and dispersive techniques.

Resonant techniques rely on the detection of scattered photons, and the most common are absorption and fluorescence imaging, where the atom number is inferred from the number of resonant photons scattered by an atomic sample. Fluorescence methods, which rely on direct capture of these scattered photons, have been used ubiquitously in atomic physics. Absorption imaging is a workhorse in the field of ultracold atomic physics, including the investigation of Bose-Einstein condensation [47], but its accurate calibration remains difficult [29, 31]. Other variations on absorption imaging exist, including resonant frequency modulation imaging [103], which has been shown to produce images with high signal-to-noise ratio (SNR) [104]. Absorption imaging can also be implemented in a *dark-ground* configuration using spatial filtering in the Fourier plane of the imaging setup to remove the unscattered probe beam and thus improve SNR [27, 28]. There also exist minimally-destructive, but still resonant, methods to perform absorption imaging of atomic clouds, including partial-transfer absorption imaging [26].

Dispersive techniques, on the other hand, detect a phase shift imprinted on the off-resonant probe light by the spatially varying refractive index of the atomic sample. Since these techniques do not rely on scattering of photons they can be made minimally destructive

and are suitable for repeated imaging of ultracold samples. Techniques that have been applied to cold and ultracold atoms include phase-contrast imaging [90, 105–107], off-resonant frequency modulation spectroscopy [108], spatial heterodyne imaging [109], diffraction contrast (or defocus) imaging [110–113], and Faraday imaging [114, 115].

In absorption imaging, an atomic sample is probed by resonant light and the atomic density is inferred based on the photons scattered out of the probing beam. For a cloud of two-level atoms in a monochromatic light field the attenuation can be obtained from the steady-state solution of the optical Bloch equations [116]

$$\frac{dI}{dz} = -\frac{\sigma_0 n(z)}{1 + I/I_{\mathrm{sat}} + \left(\frac{2\delta}{\Gamma}\right)^2} I, \tag{4.1}$$

where $n(z)$ is the atomic density, I_{sat} is the saturation intensity, δ is the laser detuning from the atomic transition and Γ is the line width of the transition.

The resonant scattering cross-section is related to the saturation intensity by $\sigma_0 = \hbar\omega_0\Gamma/2I_{\mathrm{sat}}$ where ω_0 is the resonance frequency. After integration along the z-direction, the optical density (od) and the column density $\tilde{n}$ are given by [31]

$$od = \tilde{n}\sigma_0 = \left(1 + \frac{4\delta^2}{\Gamma^2}\right) \ln\left(\frac{I_0}{I_{\mathrm{p}}}\right) + \frac{I_0 - I_{\mathrm{p}}}{I_{\mathrm{sat}}}, \tag{4.2}$$

where $\tilde{n} = \int \mathrm{d}z\, n(z)$. Extracting the column density requires a probe and a reference image, both corrected for dark counts in the absence of probing light. The probe image $I_{\mathrm{p}}(x, y)$ contains the shadow cast by the atoms while the reference image $I_0(x, y)$ contains an image of the probe beam in the absence of the atoms.

Accurate detection relies on correct determination of the saturation intensity I_{sat}, which will generally differ from the result of the two-level

atom due to the complex multi-level structure of the internal states of real atoms and imperfect polarization states of the probe beam. Additionally, the probing light imparts momentum to the atoms, which can lead to an effective detuning for typical probing durations. At higher densities, additional effects such as re-absorption processes and coherent many-body scattering come into play [29, 30]. One must also correct for the effect of an imperfect probe pulse shape [49]. All of these preclude an accurate determination of the number of atoms in a dense, cold cloud of atoms.

At low density and atom number $\lesssim 1 \times 10^4$, however, some calibration techniques have been developed. Single-atom resolved detection allows for the observation of step-like features in the atomic signal, which enables direct counting of atom numbers [77, 117, 118]. This approach is most often applied to fluorescence imaging, as it provides a better SNR at low atom numbers. At a few hundred atoms, spatially non-resolved single-atom counting becomes challenging. However, the linear relationship between the quantum projection noise and the mean atom number of coherent spin states has been used to ensure accuracy in atom counting [36].

At higher atom numbers, it has been shown that the effective saturation intensity can be inferred from the momentum acquired by the atoms during imaging [37] if an auxiliary imaging axis is available. One can also measure the number of photons absorbed by atoms during optical pumping [119, 120] to obtain an estimate of the atom number. However, the most generally employed method for calibration takes advantage of the fact that the measured atomic density should not depend on the intensity of the probe beam. By imaging samples at a given density with different probe intensities, the saturation intensity I_{sat} can be adjusted to provide accurate atom numbers [31].

In this work, we apply the calibration technique presented in Ref. [31] to ultracold atomic clouds, but our method varies the calibration as a function of optical density, allowing one to probe density-dependent

effects. Our experimental apparatus is in a unique position to perform these measurements since it can produce thermal samples actively stabilized in atom number at the shot noise level [86]. This is achieved through a combination of non-destructive Faraday imaging, online image analysis and active control of the atom number. Based on these measurements, we observe a dependence of the saturation intensity I_{sat} on optical density and the number of photons absorbed per atom. A simple recipe is presented to incorporate this calibration method into the evaluation of absorption images. Under typical experimental conditions, it leads to corrections in the detected atom number of up to $\approx 12\,\%$ and in the temperature of up to approximately $\approx 14\,\%$. The lack of active stabilization does not preclude the calibration we describe here. Rather, the atom number fluctuations common to non-stabilized experiments will simply lead to larger uncertainties in the calibrated values. Note that the experiments presented here are related to recent *in-situ* measurements [29]; however, Ref. [29] does not provide an analysis for the commonly used time-of-flight imaging technique.

4.2 Experimental method

The calibration measurements were performed in an experimental apparatus designed to produce and investigate Bose-Einstein condensates, which was previously described in detail [87]; relevant aspects are summarized here. Initially, $\approx 10^9$ ^{87}Rb atoms are trapped and cooled in a magneto-optical trap from a background vapor. Subsequently, the atoms are transferred to a magnetic quadrupole trap and mechanically moved to a second chamber with lower pressure and longer lifetime of the atomic clouds. There, the atoms are confined in an elongated quadrupole Ioffe-configuration trap [85] with trapping frequencies $\omega_r/2\pi = 247.5(2)\,\mathrm{Hz}$ and $\omega_z/2\pi = 17.26(1)\,\mathrm{Hz}$ and further

cooled by forced radio-frequency (RF) evaporative cooling.

The evaporative cooling sequence consists of a series of frequency sweeps. When the cloud contains $N \sim 4 \times 10^6$ atoms at a temperature of $\sim 14\,\mu\text{K}$, the sequence is briefly interrupted and the cloud is probed *in situ* by minimally-destructive Faraday imaging [114]. The dispersive Faraday interaction leads to a rotation of the polarization proportional to the atomic column density $\tilde{n}$ and allows for probing of the atom number with sub-shot noise precision [87]. These Faraday images are analyzed in real-time on a field-programmable gate array (FPGA), which also calculates the required fraction of atoms that must be removed to reach the desired target atom number. To induce the required losses, the FPGA controls an RF-synthesizer and applies a loss pulse with a duration adjusted to discard the appropriate number of excess atoms. The frequency of the RF radiation is chosen to remove atoms at the mean energy of the sample and thus minimize the change in temperature. Thus, atom number stability at the shot noise level can be achieved [86]. To validate successful stabilization, a second set of 20 Faraday images is acquired. Subsequently, the cloud is held in-trap for 300 ms to allow for thermal equilibrium to be established. The resulting atomic clouds contain 3.3×10^6 atoms at a temperature of $2.0\,\mu\text{K}$, which corresponds to a factor of three above the critical temperature to obtain Bose-Einstein condensation.

4.2.1 Absorption imaging

The spatially-dependent calibration technique presented here is applied to absorption images, which are acquired as follows. To initiate the time-of-flight (ToF) imaging procedure, the magnetic trapping potential is extinguished and the atomic cloud expands freely under the influence of gravity. During the time of flight, a homogeneous magnetic field pointing parallel to the imaging beam direction is applied, which enables imaging on the closed-cycle σ_+-transition from

the $|F = 2, m_F = 2\rangle$ state to the $|F' = 3, m_{F'} = 3\rangle$ state. The clouds are imaged after 12 ms of time of flight, which results in a maximal optical density $\tilde{n}_{\max}\sigma_0 \approx 4.5$.

The imaging setup consists of two lens pairs with a total magnification of $M = 4.3$. The first lens pair forms an intermediate image which allows us to restrict the imaging beam path from all sides using a four-blade knife edge mask. This ensures that the imaging light exclusively falls on the CCD chip and thus reduces scattered imaging light in particular from other parts of the CCD camera.

The imaging pulses are generated with an acoustic-optic modulator (AOM) in a double-pass configuration. The driving RF power is chosen to saturate the AOM, which minimizes the thermal drift of the deflected beam during the first few microseconds after turning it on. This allows us to produce reliable square pulses with durations as short as 3 µs.

To reduce the effect of vibrations of the optical elements, the separation between the probe and reference images is reduced to a minimum. This is achieved by applying an optical pumping pulse for a duration of a 200 µs on the $|F = 2\rangle$ to $|F' = 2\rangle$ transition, which transfers the atoms to the dark $|F = 1\rangle$ state.

In total, four images are recorded during absorption imaging. The first two contain the absorption signal of the atoms I_p and the reference image I_0, and are separated by 340 µs. Importantly, we compare the average intensity in the probe and the reference image in a region that is free from atoms and apply a correction factor to the reference image that balances these intensities. This accounts for small differences in the number of photons in the probe and reference pulse. Furthermore, two dark images are recorded three seconds later, where the imaging light is blocked. These images are used to correct for stray light reaching the camera, which may vary over time as e.g., room lights are switched on and off.

4.2.2 Calibration technique

To calibrate absorption imaging, an effective saturation intensity $I_{\mathrm{sat}} \rightarrow I_{\mathrm{sat}}^{\mathrm{eff}} = \alpha I_{\mathrm{sat}}$ was introduced by Reinaudi et al. [31], which can mitigate some of the effects outlined in Sec. 4.1. This allows a detuning of the imaging light to be absorbed in the α coefficient as $\alpha^* = \alpha\,(1 + \ 4\delta^2/\Gamma^2)$. Inserting this into Eq. (4.2) and using the implicit dependence of the cross-section on I_{sat}, the expression for the optical density becomes

$$od = \alpha^* \ln\left(\frac{\tilde{I}_0}{\tilde{I}_{\mathrm{p}}}\right) + \tilde{I}_0 - \tilde{I}_{\mathrm{p}} \tag{4.3}$$

where the normalized quantities are $\tilde{I}_j = I_j/I_{\mathrm{sat}}$, and from here on, the index j refers to the probe (p) or reference (0) image. At low intensity, $\tilde{I}_0 \ll 1$, the optical density is primarily given by the logarithmic term $\tilde{n}\sigma_0 \approx \alpha^* \ln\left(\tilde{I}_0/\tilde{I}_{\mathrm{p}}\right)$, while at large incident intensities $\tilde{I}_0 \gtrsim 1$, the linear term becomes relevant or even dominant. Since the latter term depends directly on the imaging light intensity, a calibration of the imaging camera is required.

The number of photons in the object plane of the atom cloud corresponding to the ℓ-th pixel is given by

$$\mathcal{N}_j^{(\ell)} = \frac{\mathcal{N}_{\mathrm{c},j}^{(\ell)}}{\mathcal{T}\eta g} \tag{4.4}$$

where $\mathcal{N}_{\mathrm{c},j}$ is the number of photons counted by the camera, $\mathcal{T}$ is the transmission through the optical elements in the imaging system, η is the quantum efficiency of the camera chip and g is the camera gain. Here, we assume that these images are dark-image corrected. The average normalized intensity in a given pixel is given by Eq. (3.4). In addition, the average number of absorbed photons per atom is given

by

$$\overline{\mathcal{N}}_{\text{abs}} = \frac{1}{N} \sum_{\ell}^{\text{ROI}} \mathcal{N}_0^{(\ell)} - \mathcal{N}_p^{(\ell)} \tag{4.5}$$

where N is the total atom number $N = A/\sigma_0 \sum_{\ell}^{\text{ROI}} od^{(\ell)}$. The sum is over all pixels ℓ in the region of interest (ROI) of the image.

To infer α^*, one takes advantage of the low- and high-intensity limits of Eq. (4.3). In practice, the intensity of the imaging light $\tilde{I}_0$ is varied from shot to shot while keeping the density of the imaged samples constant. Thus, one obtains data where the balance between the linear and logarithmic terms in Eq. (4.3) varies. Since the optical density should not depend on intensity, the optimal value of α^* is the one that leads to the smallest variance of the evaluated optical density. However, the optimal α^* depends on density and on the number of absorbed photons, as shown in the following.

4.3 Spatially dependent α^*-calibration

To obtain a spatially corrected α^*-coefficient, the two dark-count-corrected images, I_{p} and I_0, are azimuthally averaged. The aspect ratio of the cloud is taken into account by averaging elliptical ROIs with a width of 10 pixels, where the major and minor axes of the ellipses are proportional to the cloud widths in both directions. These cloud widths are determined by a Gaussian fit to the cloud *od* given by Eq. (4.3) with $\alpha^* = 1$. Figure 4.1 shows the optical density of a single, typical experimental image of a thermal atom cloud with its Gaussian density profile and these elliptical ROIs. The widths of the elliptical ROIs were chosen as a compromise between the desired spatial resolution and the signal-to-noise ratio of the resulting calibration coefficients.

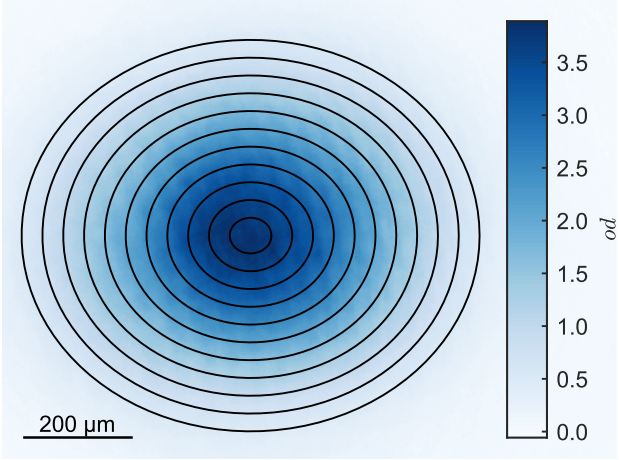

FIGURE 4.1: Optical density of an atomic cloud recorded for standard imaging conditions using $\alpha^* = 1$. Lines indicate borders of elliptical regions in which separate values of α^* are extracted.

Images like the one shown in Fig. 4.1 are acquired for a range of imaging intensities at a fixed average number of absorbed photons $\overline{\mathcal{N}}_{\mathrm{abs}}$. This minimizes the influence of, e.g., the induced Doppler shift from scattered photons. When performing a single calibration, $\overline{\mathcal{N}}_{\mathrm{abs}}$ should match that used for actual experiments. Consequently, the probe exposure time has to be adjusted to account for the imaging intensity. The maximum available intensity was 7.9 I_{sat}, resulting in a minimum pulse duration of 2.2 μs. On the other hand, the measurements were performed with pulse durations below 32.3 μs to constrain the vertical movement of the atoms during probe exposure to the size of one pixel. This results in a minimum imaging intensity of 0.13 I_{sat}. For each imaging intensity, 2 to 3 experimental runs are performed.

To obtain the α^*-coefficient, Eq. (4.3) can be recast into a linear

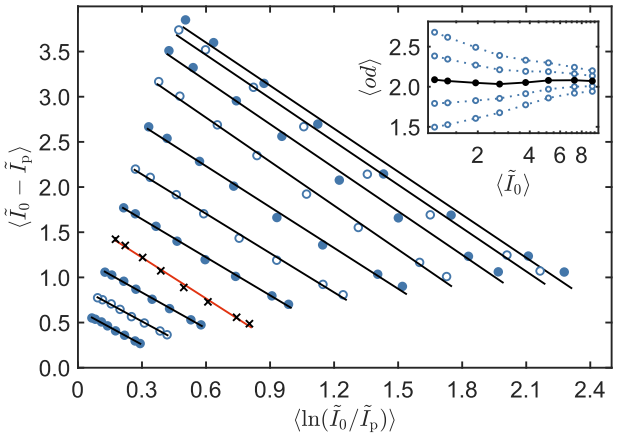

FIGURE 4.2: Determination of the α^*_k-coefficient and optical density od_k. The data points in each region of interest k (alternating blue dots and circles) show a linear dependence. The black lines are fits according to Eq. (4.6) where the slope corresponds to the value of α^*. The data points indicated by crosses and the corresponding linear fit (orange) represent a global determination of α^*. For this calibration, the average number of absorbed photons per atom was $\overline{\mathcal{N}}_\mathrm{abs} \approx 183$. (inset) Visualization of the effect of α^* for a specific region with $\langle od \rangle \approx 2$ (black dots: optimal α^*, open circles: $\alpha^* \pm 0.3$ and ± 0.6). The optimal α^* minimizes the dependence of $\langle od \rangle$ on probe intensity [31].

equation

$$\langle \tilde{I}_0 - \tilde{I}_\mathrm{p} \rangle_\mathrm{k} = \langle od \rangle_\mathrm{k} - \alpha^*_\mathrm{k} \left\langle \ln\left(\frac{\tilde{I}_0}{\tilde{I}_\mathrm{p}}\right) \right\rangle_\mathrm{k}, \tag{4.6}$$

where the $\langle\rangle_\mathrm{k}$ indicates averages over the k-th elliptical ROI. Since these averages can be determined directly from the image data, a linear fit can be used to determine both the α^*_k-coefficient and the optical density od_k in each ROI.

Figure 4.2 shows such linear fits to the averages in Eq. (4.6) for each

ROI, where the α_k^*-coefficients are given by the slopes, and the offsets provide the average optical density od_k in each ROI. This method has the advantage of providing uncertainties on the fitted quantities, which is used in the following. In what follows, we will refer to this as the *local* calibration method.

In addition, Fig. 4.2 illustrates two other methods to determine non-spatially-resolved α^*-coefficients. The *original* method [31] determines the peak optical density as a function of the imaging intensity for various values of α^*. An incorrect α^* leads to a clear dependence on the intensity, while the optimal value minimizes the variation as shown in the inset of Fig. 4.2. Note that Ref. [31] kept the total number of photons in the imaging pulse constant, while the total number of absorbed photons is kept constant in this work. Moreover, a *global* α^*-coefficient can be determined by taking the averages in Eq. (4.6) over the entire image and performing the linear fitting technique (see orange line in Fig. 4.2). This method provides a simpler approach that focuses on calibrating the total atom number instead of the peak *od* as in the *original* method.

4.3.1 Density dependence

A close inspection of Fig. 4.2 shows that the magnitude of the slope increases for ROIs with larger $\langle od \rangle$, i.e., the lines with higher y-intercept, *cf.* Eq. (4.6). Moreover, the data points deviate from a linear dependence for the highest optical densities. While our analysis captures the general density dependence, a microscopic description of the imaging process is required to explain the nonlinear behavior [30].

Figure 4.3 shows the α^*-coefficient extracted within each ROI as a function of the corresponding optical density for two average numbers of scattered photons per atom. The α^* values show a clear increase as a function of optical density, and this dependence is enhanced for a

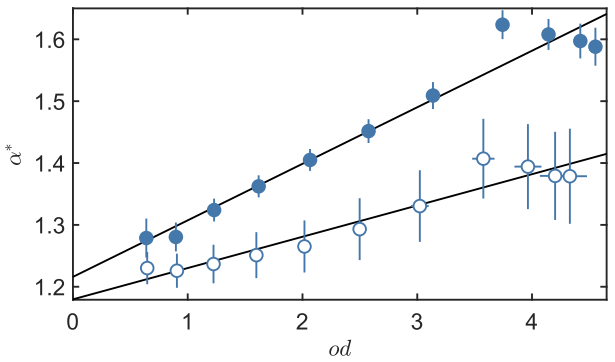

FIGURE 4.3: Dependence of the α^*-coefficient on optical density. The solid and open points correspond to data taken with an average number of $\overline{\mathcal{N}}_{\mathrm{abs}} \approx 183$ and 71 absorbed photons per atom, respectively. The errors represent the uncertainty of the linear fits in Fig. 4.2 without weights. The larger errors for open points show that fewer absorbed photons lead to a larger discrepancy from a linear fit (see main text). We exclude ROIs with $\langle od \rangle < 0.5$ due to the large uncertainties of these points. The lines are fits according to Eq. 4.7.

larger average number of scattered photons. We attribute this to the effects outlined in Sec. 4.1, dominated by the re-absorption of photons.

The density dependence in Fig. 4.3 is modelled with a linear relation

$$\alpha^* = \alpha_0 + \alpha' od. \tag{4.7}$$

Figure 4.3 includes two such linear fits, which allow us to determine α^* for all optical densities in a given atom cloud. Thus, this realizes a spatially dependent calibration that can be applied in subsequent experiments.

To investigate the origin of the density dependence, we have simulated the effects of a non-square pulse shape, motion due to gravity during exposure, and a time-dependent detuning that depends on the

number of scattered photons per atom in each voxel by numerically integrating Eq. (4.1) on a 3D grid using a finite difference approach. These simple simulations, which do *not* include many-body effects such as re-absorption processes, do not lead to appreciable deviations from the expected *od*-independent α^*-coefficient. Therefore, we conclude that many body scattering processes must be included for an accurate representation of the dynamics involved. This is corroborated by Ref. [29], which explores, theoretically and experimentally, the effect of incoherent many-body scattering and shows a similar linear dependence to the one used in Eq. (4.7).

4.3.2 Photon number dependence

The differences in the α^*-coefficients obtained at various numbers of absorbed photons per atom motivate further investigation. The calibration was, therefore, repeated multiple times for different average absorbed photon numbers between $\overline{\mathcal{N}}_{\mathrm{abs}} \approx 38$ and 185.

Figure 4.4 shows the slope α' and offset value α_0 as a function of $\overline{\mathcal{N}}_{\mathrm{abs}}$. The slope α' increases to good approximation linearly for the values of $\overline{\mathcal{N}}_{\mathrm{abs}}$ considered here, which we attribute to the many-body scattering effects outlined in Sec. 4.1. A similar, statistically slightly less significant linear increase is observed for α_0. This increase as a function of the absorbed number of photons may be attributed to the resulting larger effective detuning due to the accumulated Doppler effect. Most importantly, this illustrates the importance of performing the calibration under the same conditions at which imaging in later experiments is performed (see also Sec. 4.5). In particular, the same average number of absorbed photons should be used, and the calibration measurements should include clouds of similar average *od*.

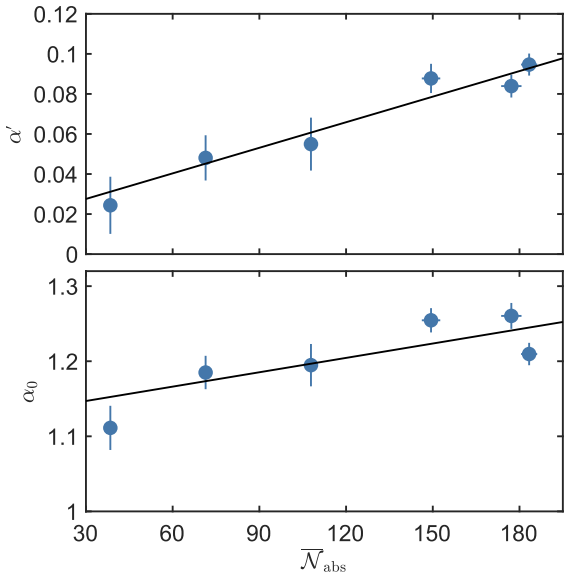

FIGURE 4.4: Gradient α' and offset value α_0 of the α^*-coefficient as a function of the average absorbed number of photons per atom $\overline{\mathcal{N}}_{\mathrm{abs}}$. The points show the values extracted from weighted linear fits according to Eq. (4.7), and the error bars denote the error on the fit.

4.4 Impact of spatial calibration

This section describes the implementation of the *local* calibration and demonstrates its effect on the cloud profile, total atom number N, and temperature T. The linear dependence of α^* can easily be incorporated into the standard procedure for extracting the optical density. By inserting Eq. (4.3) into Eq. (4.7) one obtains

$$od = \frac{\alpha_0 \ln\left(\frac{\tilde{I}_0}{\tilde{I}_\mathrm{p}}\right) + \tilde{I}_0 - \tilde{I}_\mathrm{p}}{1 - \alpha' \ln\left(\frac{\tilde{I}_0}{\tilde{I}_\mathrm{p}}\right)} \tag{4.8}$$

Thus, one can use the calibrated values of α_0 and α' to determine the *od* directly. Using this procedure, each pixel is assigned an individual α^* value given by

$$\alpha^* = \frac{\alpha_0 + \alpha'(\tilde{I}_0 - \tilde{I}_\mathrm{p})}{1 - \alpha' \ln\left(\frac{\tilde{I}_0}{\tilde{I}_\mathrm{p}}\right)}. \tag{4.9}$$

To test the effect of the *local* spatial calibration, we compare it to the *original* method via an analysis of clouds with a range of different atom numbers N and temperatures T. We studied atomic clouds under 10 different conditions by gradually lowering the end-frequency of the RF evaporation and, for each end-frequency, we produced sets of ≈ 60 identical clouds. The hottest set of clouds had $T = 1.855 \pm 0.006\,\mu$K, $N = (3.34 \pm 0.02) \times 10^6$ and peak $od = 4.57 \pm 0.02$, while the coldest set had $T = 693 \pm 5\,$nK, $N = (1.86 \pm 0.02) \times 10^6$, and peak $od = 6.44 \pm 0.07$.

The clouds were imaged under conditions where the average number of absorbed photons per atom was $\overline{\mathcal{N}}_\mathrm{abs} = 180 \pm 5$ and the obtained calibration coefficients were $\alpha_0 = 1.21$, $\alpha' = 9.5 \times 10^{-2}$ (*local* method), $\alpha^* = 1.69$ (*original* method), and $\alpha^* = 1.51$ (*global* method).

Figure 4.5 shows examples of azimuthally-averaged cloud profiles obtained with the *original* method, the *local* method and without calibration ($\alpha^* = 1$). The optical density was averaged along elliptical contours with a horizontal width of three pixels. The upper and lower figures show examples of clouds from the hottest and coldest set, respectively.

The *local* method typically yields a lower estimated optical density in the wings of the clouds than the *original* method, resulting in a narrower distribution. However, the calibrated peak *od* can be either lower or higher depending on the temperature and actual peak *od*. To understand this behavior, it is important to note that the two calibrations were conducted on clouds with a peak $od \approx 4.5$, similar to the cloud in the upper figure. The *original* method determines a single

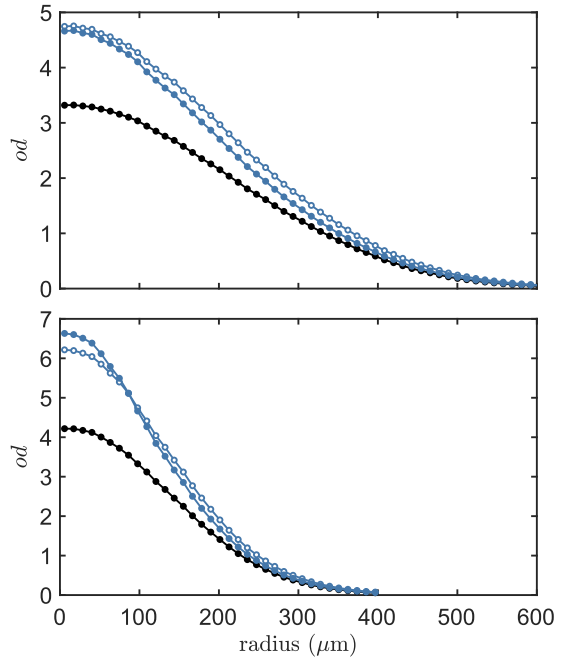

FIGURE 4.5: Comparison of the *od* profiles for atomic clouds evaluated using three different calibration methods: the *local* calibration (solid blue points), the *original* calibration method used in Ref. [31] (open blue circles), and no calibration ($\alpha^* = 1$, black points). The *optical density* was averaged azimuthally along elliptical contours, and here, the horizontal dimension is shown. The figure shows the cloud profiles for both a hot (top, $T = 1.855 \pm 0.006\,\mu$K) and a cold cloud (bottom, $T = 693 \pm 5\,$nK).

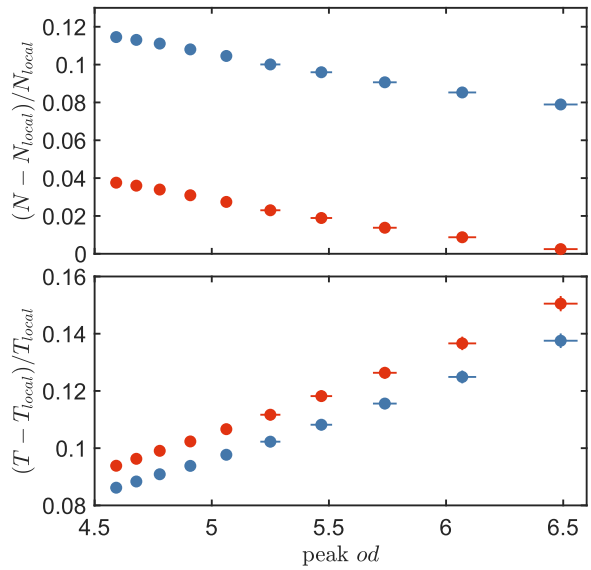

FIGURE 4.6: Relative deviations in the atom number and temperature resulting from the *original* calibration [31] (blue) and the *global* calibration (red) compared to the *local* method (N_{local} and T_{local}). The points (error bars) denote the mean values (standard deviation) from ≈ 60 clouds prepared with the same RF end-frequency.

α^* value that minimizes the dependence of the peak *od* dependence of the probe intensity and applies this locally optimal α^* on all pixels. Knowing that the appropriate α^* increases with *od* it is clear from Eq. 4.3 that the *original* method overestimates all optical densities below the peak *od* used in the calibration cloud and underestimates all optical densities above.

These effects generally lead to discrepancies between the two methods in extracting atom number, N, and temperature T. The deviations of the *original* method from the *local* method are shown in Fig. 4.6.

For both methods, N is calculated by summing the signal in the full ROI, and T is extracted from the width of a fitted Gaussian distribution. Each point is the mean value of sets of ≈ 60 clouds prepared with the same end-frequency of the RF evaporation.

The *local* method introduces corrections in the total atom number up to $\approx 12\,\%$ and in temperature up to $\approx 14\,\%$. For clouds with a peak *od* close to the one used for the calibration, the *original* method most dramatically overestimates the total atom number since the optical density in the wings is overestimated. When cooling further and increasing the peak *od* a gradually increasing underestimation of the peak *od* by the *original* method begins to compensate for the overestimation in the wings.

For temperature, however, the trend is the opposite. Here, the correction from the *local* method is lowest for low peak *od*, where there is an overestimation by the *original* method in the wings of the cloud. For colder clouds, this overestimation is accompanied by an underestimation of the peak *od*, leading to an increasing overestimation of the cloud width and temperature.

Overall, the *original* method is not fully accurate even for the exact cloud parameters used in the calibration, since it only performs the calibration for a specific *od*. Thus, the derived α^* will not necessarily render parameters like N and T independent of the probe intensity. The *global* method suffers from similar issues, but it improves the accuracy of the total atom number since it is a calibration for the average *od*. On the other hand, the *local* method addresses the density dependence of α^* by providing individual calibration parameters for each pixel.

4.5 Practical calibration considerations

In order to perform an α^* calibration for a given experiment, one proceeds as follows: First, a set of images is taken with $\alpha^* = 1$, varying I_p while keeping $\overline{\mathcal{N}}_\mathrm{abs}$ constant by adjusting the imaging pulse duration. The data is then segmented into elliptical ROIs as shown in Fig. 4.1 and plotted as in Fig. 4.2(d). Based on this data, the density dependence of α^* can be obtained as a function of *od* as shown in Fig. 4.5, and the slope and offset (α' and α_0) can be extracted from a linear fit. These values allow for a pixel-by-pixel determination of α^* from Eq. (4.9). The system is now calibrated, and the density profile of future experimental images can be corrected using the pixel-by-pixel correction of α^* in Eq. (4.3).

Note that the slope and intercept are dependent on the value of $\overline{\mathcal{N}}_\mathrm{abs}$ and re-calibration is necessary for different $\overline{\mathcal{N}}_\mathrm{abs}$. In practice, low *od* values lead to large uncertainties in the fit, so only cloud ROIs with $\langle od \rangle$ above 0.5 are used to extract α' and α_0. It may be advantageous to perform the calibration for a shorter time of flight than used in the final experiment, which will enable it to cover a broader range of *od* values.

Moreover, it is important to reduce the effects of fringes in images that are caused by variations between the probe and reference images due to vibration of the optical elements or out-of-focus effects and astigmatism. These fringes should be minimized (e.g. using minimal separation between the probe and the reference image or using the methods in Refs. [32–34]), since the local value of α^* in these regions will enhance the effect of the fringing. That is, the dense region in a fringe will be given a higher local α^*, leading to an enhancement in the *od*.

While the method and data presented here profit from the atom number stabilization provided by Faraday imaging, this is not a necessary requirement to perform this type of calibration. One would find

that the error bars on the data lead to a larger uncertainty in α^*; however, the typical atom number and *od* fluctuations in a well-functioning experiment would not preclude a spatially-resolved α^* calibration.

4.6 Conclusion

In conclusion, we have presented a spatial calibration technique for time-of-flight absorption images of ultracold atomic clouds. Our calibration method is *local* since it assigns a calibration coefficient α^* for each optical density. The analysis shows a significant dependence of the calibration coefficient α^* on the optical density which we attribute to the many-body scattering processes and the re-absorption of photons [29, 30]. The calibration coefficient can readily be obtained from absorption images, and we provide a practical guide to the calibration process. Finally, it is shown that the spatial calibration technique leads to corrections in the detected atom number up to $\approx 12\,\%$ and in temperature up to $\approx 14\,\%$ in comparison to previous calibration techniques.

Our work highlights the aforementioned difficulties in the accurate determination of atom numbers and temperatures of dense clouds of ultracold atoms. Accurate techniques are available for small [77, 121] and mesoscopic [36] atoms numbers. However, the best available calibration techniques for large atomic samples rely on models of light interacting with a single atom [31, 120]. Due to a lack of alternatives, these techniques are nonetheless commonly employed in dense atomic clouds and BECs [29]. The technique presented here mitigates some of the difficulties by an empirical calibration strategy, and as such, it could be applied to BECs, e.g., by employing long times of flight or partial-transfer absorption imaging [26] to achieve optical densities in the range considered here.

Our work shows the need for further theoretical developments

to understand the scattering processes in ultracold dense clouds of atoms [30]. A more detailed understanding may explain the differences between the results reported here and those presented in Ref. [29] for *in-situ* measurements. In particular, we do not observe a universal slope of α^* in Eq. (4.7), but find that this depends on the absorbed photon number. Furthermore, future experimental work should explore the applicability of our method at lower temperatures and higher densities, particularly in the BEC regime. These developments will allow for a better understanding of the many-body scattering processes that underpin atom-light interactions in dense atomic ensembles.

Chapter 5

Atom Number Fluctuations in BECs

This chapter presents a comprehensive statistical analysis of uncertainties in the preparation and parameter estimation of partially condensed Bose gases, aimed at extending our understanding of atom number fluctuations in Bose-Einstein condensates. It is based on the paper in preparation [3], with the paper's introduction incorporated into the thesis introduction (Section 1.2). Certain theoretical results and methods have been omitted here. This concerns statistical formulas and spatial distributions for the thermal clouds already covered in Section 2.4 and Section 2.3, as well as formulas for optical density its associated error already covered in Section 3.5. Additionally, the initial part of the experimental sequence closely resembles that described in Section 4.2, and is also left. On the other hand, in Section 5.2.4 and Section 5.2.5, further details are added compared to the paper draft. The analysis and drafting of the paper have been predominantly conducted by me.

To begin, I will briefly motivate the work presented in this chapter, by summarizing the result of our prior research [2], upon which the analysis in this paper is based. After the group measured atom number fluctuations in a BEC for the first time [52], we aimed to characterise

these fluctuations as a function of atom number and trap geometry. However, pinning down these dependencies proved challenging due to the quality of the resulting data. Nonetheless, we were able to make an overall comparison between the observed peak fluctuations and the theoretical predictions of the canonical ensemble.

As discussed in Section 2.2, the expectation of fluctuations in the microcanonical ensemble is lower than that of the canonical ensemble. However, calculations in the microcanonical ensemble for typical experimental conditions remain unattainable. Observing peak fluctuations reduced by 27 % compared to the canonical result indicates that the microcanonical ensemble may indeed be a more appropriate framework for modelling these experiments.

When re-examining the data of [2], we were surprised that to find that the estimation errors of the thermal cloud were sufficiently low for the observation of atom fluctuations in this component as well. Furthermore, we discovered that these fluctuations were strongly anticorrelated with those of the BEC as expected for fundamental fluctuations between the two components. To determine whether this was the observation of particle exchange between the two components or if this anticorrelation arose from the estimation methods, a detailed analysis of all significant noise contributions to the BEC and thermal atom numbers was required.

Through Monte Carlo simulations of optical density profiles obtained by absorption imaging, the noise contributions to the estimation of atom number and temperature are assessed for both the condensed and thermal cloud, providing insights relevant across the field of ultracold atoms. This analysis was specifically applied to fluctuations measurements to get insight into the aforementioned anticorrelation and to improve the estimate of the fundamental peak fluctuations.

5.1 Experimental description and data analysis

5.1.1 Experimental setup

The experimental sequence is described in Section 4.2. The present sequence, however, has the following deviations. After stabilizing the atom number, the trap is smoothly changed to the desired end-aspect ratio, $\lambda = 5.4$, by controlling the current bypassing the quadrupole coils, and the final cooling to reach BECs is performed. Equilibrium is ensured by holding the final radio frequency for 800 ms, after which the atoms are held for a further 400 ms without rf radiation before trap turn-off.

The cloud is imaged after 35 ms time-of-flight with an imaging pulse duration of $\tau = 30\,\mu s$ and an intensity of $I_0 = 3.2\ I_{sat}$, where I_{sat} is the saturation intensity. In this sequence, two additional images without atoms are captured, which are identical to the probe and reference images. These images are used for diagnostic purposes such as the analysis of pixel noise.

5.1.2 Determining atom cloud parameters

Based on the images of the atom clouds, the relevant parameters, such as atom number and temperature, are determined as follows. First, the intensity is computed using Eq. (3.4), followed by the determination of optical density using Eq. (3.6). Figure 5.1 shows a typical optical density profile. The relevant parameters are extracted by fitting the wings of the cloud (area between the blue and red ellipse) with a Bose-enhanced Gaussian distribution given by Eq. (2.39).

The widths are linked to the effective temperature, T_j, through the equation $w_j = \sqrt{k_B T_j/m}\sqrt{1/\omega_j^2 + t^2}$. Here, ω_j for $j = z, r$ denotes the

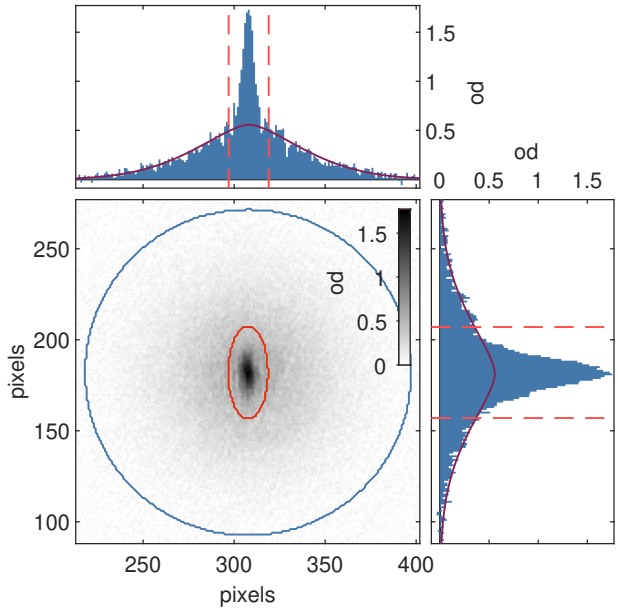

FIGURE 5.1: Example of an optical density profile (lower left panel) and cross sections through the center in both directions (side panels). The radius of the blue ellipse is 3 times the thermal width (as defined in Eq. (2.39)). The area within the blue ellipse is called the *cloud region*. The area within the red ellipse is the *BEC region*, and the area between the blue and red ellipse corresponds to the *wings* of the thermal cloud. The edges of the BEC region are projected as dashed red lines in the side panels. The purple lines in the side panels show the thermal fit.

axial and radial trapping frequencies, t is the time of free expansion, and m is the mass of the atomic species. These temperatures are averaged to a single temperature according to [46, 122].

In a second step, the fit is extrapolated to the BEC region (red ellipse in Fig. 5.1) and subtracted from the data. The remaining signal within this region is then summed up to determine the BEC atom

number, N_0. Additionally, the total atom number N is measured by summing up the signal in the entire cloud region.

The final evaluation of all clouds in the analysis uses a fixed center of the cloud region and a fixed elliptical BEC region large enough to encompass the largest BEC. The radii of the BEC region are set to $S = 1.13$ times the largest recorded BEC radii from Thomas-Fermi fits (red ellipse in Fig. 5.1). Additionally, a slightly larger elliptical region defined by $S = 1.2$ sets the inner boundary for the thermal fit region to ensure a stable fit [46].

The outer boundary of the wings (blue ellipse) is determined from a pre-analysis of the entire fluctuations data set performed with a fixed thermal region large enough to include the warmest cloud. The total atom number, N, and the widths, w_j, are extracted for all clouds. We fit a higher-order polynomial to w_i as a function N, which provides us with $w_i(N)$. In the final evaluation, we set the cloud region to 3 $w_i(N)$ based on the total atom number N in an image to be evaluated.

5.1.3 Measurement of atom number fluctuations

The fluctuations are measured as a function of temperature (corresponding to a final rf). To determine fluctuations at a specific temperature, the variance of the atom number in the BEC and the thermal cloud needs to be obtained from samples prepared under the same conditions. In practice, ≈ 60 experimental realizations were used to obtain a variance. Only realizations for which the atom number stabilization succeeded were included, and a minimum of 45 clouds were required to evaluate the variance. Figure 5.2 shows the atom number in the BEC, N_0, and the thermal atom number, N_{th} as a function of the total number N for such a set of measurements.

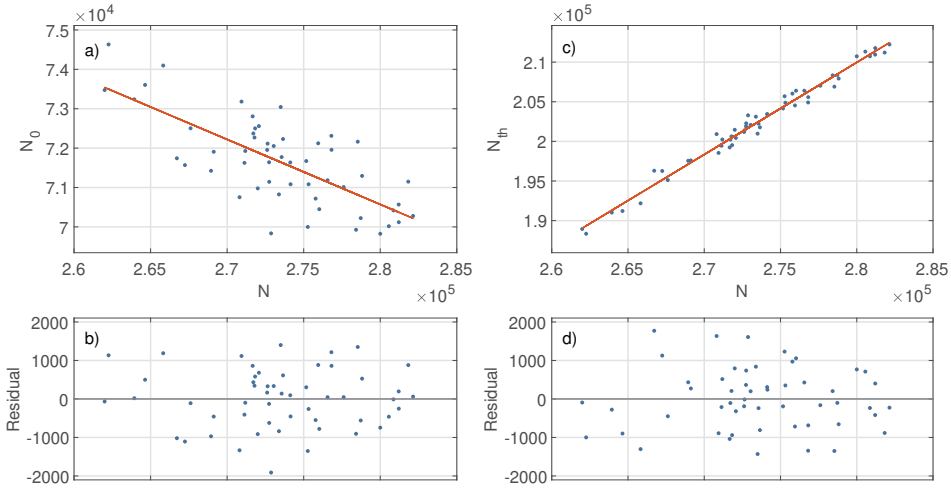

FIGURE 5.2: In order to prevent technical drift caused by the stochastic nature of evaporation, N_0 (a) and N_{th} (c) are plotted against N and fitted to a line. The variances of these are calculated from the residuals shown in (b) and (d).

Since each measurement takes ≈ 90 s, a measurement set takes considerable time during which the experimental apparatus is exposed to drifts in temperature. This leads to small drift of the trap depth, which results in a small drift in the total atom number and temperature. Consequently, the variance of the atom numbers cannot be calculated directly. Instead, the technical drift within a set of ≈ 60 experimental realizations is eliminated by subtracting a linear fits $N_0(N)$ from the BEC atom number and $N_{\mathrm{th}}(N)$ from the thermal atom number as shown in Fig. 5.2. This subtraction proved vital to the observation of fluctuations [2, 52] and in the following, it is referred to as the *correlation method*. The variance is then determined as the two-sample variance (Eq. (2.47)) of the residuals shown in Fig. 5.2 (b) and (d). The error of the variances is obtained from Eq. (2.49).

Figure 5.11 shows the measured variances of the BEC (red dots) and the thermal cloud (blue dots). As expected, both variances show a sharp increase in fluctuations just below the critical temperature. In addition, the temperature variance was studied. Again, the two-sample variance of the residual was taken after subtracting a linear fit from the temperatures T as a function of the N for each of the sets of ≈ 60 clouds. Figure 5.5 shows the standard deviation of T as a function of temperature. It lies around 1 nK and slightly increases toward colder temperatures, where smaller clouds of atoms degrade the thermal fit.

In both cases, it is clear that a detailed model of technical noise and its effects on the extracted variances is of great importance. Such a model of the inherent technical noise sources is the main result of this paper, as discussed in the following sections.

5.2 Cloud parameter noise analysis

This section focuses on a particular type of technical noise – the estimation errors associated with cloud parameters. The mechanisms responsible for these errors are general and applicable to any analysis of density profiles obtained using absorption imaging, not just studies of fundamental atom number fluctuations. Due to the complexity of the data analysis, it is challenging to derive analytical expressions for the estimation errors and our analysis is based on a Monte Carlo simulation.

In the following, the most critical mechanisms impacting the estimation errors and their implementation in the Monte Carlo simulation are described. In addition, we briefly discuss the imaging effects not included in the simulation.

5.2.1 Imaging noise in optical density

The main contributions to uncertainties in the value of the optical density in each pixel of the absorption images (Fig. 5.1) arise from photon shot noise and camera errors. The pixel uncertainties are given by Eq. (3.9), wherein the incorporation of Eq. (3.10) and Eq. (3.11) gives the contribution from photon shot noise.

An analysis of ≈ 1000 empty images shows that shot noise is the predominant contributor to the noise of the individual pixel values with the average spread of $\Delta od_{\mathrm{SN}}^{(\ell)} \approx 0.026$, or $\Delta N_{\mathrm{SN}}^{(\ell)} \approx 1.3$ per pixel. Note that the shot noise for the individual pixel is completely uncorrelated to neighbor pixels. However, the analysis also shows indications of correlated noise due to camera effects. This correlated noise can be orders of magnitude smaller but still cause significant errors in parameter estimation because it is correlated between pixels.

We did not specifically map out the pattern of the correlated camera noise but found that adding a global error $\Delta od_{\mathrm{cam}} = 2 \times 10^{-4}$ (all pixels in the cloud region get the same value in each of the reconstructed images) to the shot noise reproduces the estimation error of the total atom number $N = A/\sigma_0 \sum_{\ell}^{\mathrm{CR}} od^{(\ell)}$ in the empty images [1]. Here, the sum is over all pixels ℓ in the *cloud region* (CR) of the image.

The expected estimation error of the total atom number from shot noise alone is given by Eq. (3.12). In our experiment, this error is significantly exceeded. This deviation is largest when using large cloud regions where the shot noise has relatively less impact. For the magnitudes of $\Delta od_{\mathrm{SN}}^{(\ell)}$ and Δod_{cam} mentioned above, the correlated camera noise becomes the dominant contribution for cloud regions involving more than $\approx 17,000$ pixels. Note that the full cloud region varies from $\approx 65,000$ pixels for warm clouds to $\approx 15,000$ pixels for cold clouds, while the BEC region has a fixed size of $1,428$ pixels. Therefore, the

[1] This was done in a Monte Carlo simulation.

BEC atom number is completely dominated by shot noise, and the camera noise mainly affects the thermal and total atom number.

The error in the optical density affects the estimation errors of all extracted parameters: Total atom number, thermal atom number, BEC atom number, as well as temperature.

5.2.2 Finite number noise for the thermal cloud

This analysis assumes that the thermal cloud follows a Bose-enhanced Gaussian distribution for all temperatures. However, due to a finite number of thermal atoms, a perfect distribution never occurs, and Poisson noise is expected for the number of atoms per pixel. This finite number effect is easily simulated by randomly drawing the position of each atom based on the spatial probability function (Eq. (2.39)).

Apart from the extra noise on the individual pixels that impacts the thermal fitting, the finite number effect also causes binomial variations in the number of atoms present in the BEC region, and in the wings of the cloud (see Fig. 5.1), and even beyond the $3w_i$ wide cloud region. However, even if choosing the full cloud region to be $3\,w_i$ in radius does have a slight systematic effect on the total atom number, the statistical binomial variation in how many atoms are found inside and outside the region is negligible.

5.2.3 Simulation of noise contributions

In the following, we describe a Monte Carlo simulation of density profiles of atom clouds, including the noise contributions discussed in Sec. 5.2.1 and 5.2.2. This simulation allows for an analysis that mimics the experimental analysis procedure described in Sec. 5.1.2. Thus, it enables the extraction of estimation errors on N_0, N_{th}, N, and T.

The simulation was conducted for 40 temperatures covering the full experimental range. To simulate atom clouds at an arbitrary temper-

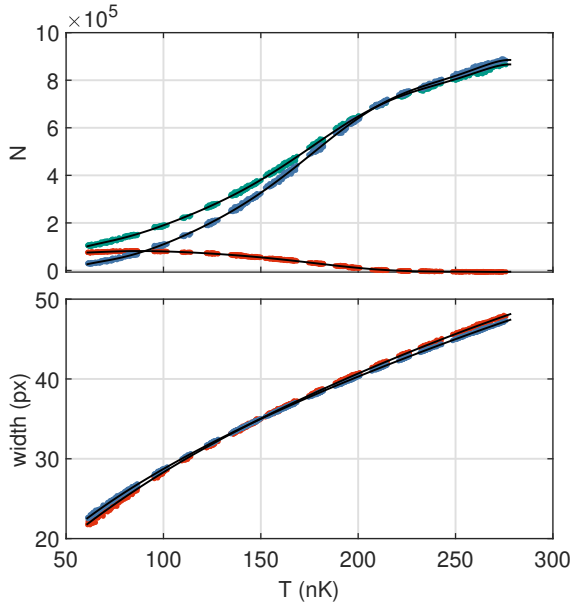

FIGURE 5.3: Polynomial fits of cloud parameters for all ≈ 1000 clouds in the analysis for the entire temperature range. The upper panel shows the thermal atom number N_{th} (blue points), the BEC number N_0 (red points), and the total atom number N (green points) as a function of temperature T. The lower panel shows the axial (red points) and radial (blue points) thermal cloud widths after time-of-flight expansion. The black lines indicated the polynomial fits used in the analysis.

ature, knowledge of the mean value of N_0, N_{th}, and the cloud widths, w_i, of the thermal cloud as a function of temperature is required. These are obtained from higher-order polynomial fits $N_{\mathrm{th}}(T)$, $N_0(T)$, and $w_i(T)$ to the experimental thermal atom number, the BEC number, and the widths, respectively, as a function of temperature for all ≈ 1000 clouds in the measurement. These fits are shown in Fig. 5.3.

In the simulation, images corresponding to in Fig. 5.1 are construc-

ted as follows. For a given temperature, the thermal cloud widths are obtained from the polynomial fits and inserted in the probability function Eq. (2.39). Now, the position of each thermal atom is randomly drawn from the probability function, and they are placed on a grid corresponding to 400×400 pixels, which corresponds to more than ± 4 cloud widths of the warmest clouds. This produces simulated images with the appropriate spatial distribution and directly reproduces the finite number noise discussed in Sec. 5.2.2).

Shot noise is randomly added to each pixel with a standard deviation of $\Delta od_{\mathrm{SN}} = 0.026$. To speed up the simulation, the magnitude is the same for all pixels regardless of the actual *od*. This can be justified by the fact that for the thermal cloud in wings, the optical density maximally differs from $od = 0$ to $od = 1.5$, and thus, the expected difference in the magnitude of the shot noise for these two cases is on the level of 2×10^{-3}. In the BEC region, larger *od*'s are recorded, leading to larger differences in the magnitude of shot noise. However, as will be clear later, the direct effect of shot noise on the BEC estimation is minimal. Finally, the completely correlated camera noise is added $\Delta od_{\mathrm{cam}} = 2.0 \times 10^{-4}$ to all pixels.

The simulated images of atom clouds are fitted with Eq. (2.39) using the least square method with the same error on all pixels. The settings for the *cloud region* and the extraction of N_0, N_{th}, N, and T are identical to the evaluation of real clouds as described in Sec. 5.1.2, i.e. the *wings* of the cloud are fitted to Eq. (2.39) to extract N_{th} and T. This thermal distribution is then subtracted from the *BEC region*. N_0 is obtained by summing the remaining *od* data in this region and N by summing the raw data in the entire *cloud region*.

There are three mechanisms contributing to the error of the BEC atom number. To gain further insight into these, we also record the summing error caused by $\Delta od^{(\ell)}$ in the BEC region, secondly, the variation of the thermal atom number in the BEC region (finite number effect), and, finally, the variation of the thermal fit evaluated in the

BEC region.

The process of constructing images, adding noise, and fitting the thermal distribution was repeated 100,000 times for each temperature. This allows for the determination of the variances, covariances, and correlations between each of the measured quantities. In essence, the covariance matrix (see Sec. 2.4.3) is obtained for each temperature.

5.2.4 Cloud parameter estimation errors

Figure 5.4 shows the results of the simulation in Sec. 5.2.3. The upper figure illustrates the estimation errors for the BEC atom number, where the primary contributions are the variation in the thermal fit evaluated in the BEC region (blue) and the binomial error in the BEC region (green) arising from the finite number of thermal atoms. The direct impact of errors in *od* (purple) is minimal. The thermal fit effect remains relatively constant within the temperature range. The error due to finite number dominates at and above the critical temperature but decreases with temperature due to the reduction in thermal atoms. The remaining lines are discussed in subsequent sections. Note that the temperature axis is scaled with the critical temperature for an ideal gas, T_c^0, which is not constant due to the loss of atoms during evaporative cooling.

The lower panel of Fig. 5.4, shows that the estimation error of the thermal atom number from the fits (blue) is slightly larger than that for the total atom number (orange) obtained from summing the signal in the full cloud region. The error increases in a nearly linear manner and reflects that for low temperatures, the clouds are narrower, and fewer pixels enter the cloud region, leading to a smaller impact from Δod. However, as the atom number also decreases with lower temperatures, the relative error for both the total atom number and the thermal cloud, in fact, increases. For both of these quantities, we observed a relatively large impact from camera effects. These are en-

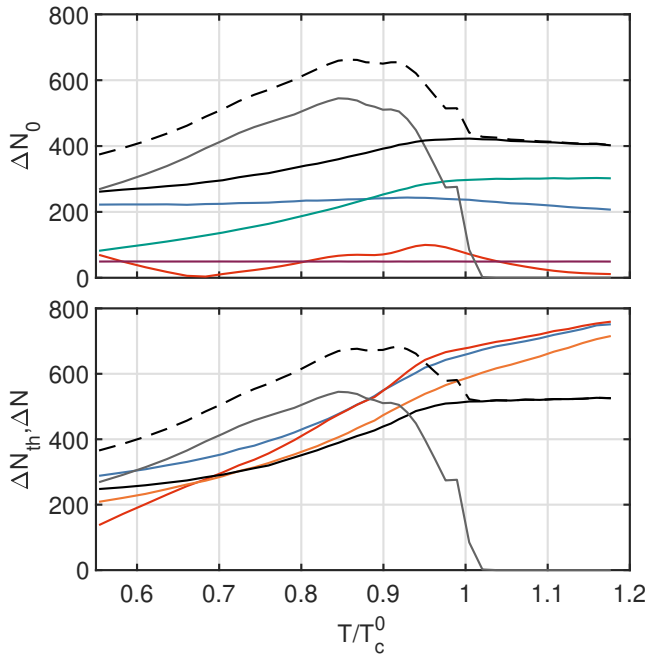

FIGURE 5.4: Technical errors (standard deviation) of the BEC, thermal, and total atom numbers for various noise sources. The upper panel shows errors for the BEC atom number. (Blue) Error of the thermal fit in the BEC region. (Green) Error from the distribution of a finite number of thermal atoms in the BEC region. (Purple) Error from shot noise and camera noise. The lower panel shows the technical errors for the thermal and total atom numbers. (Blue) Estimation error of the thermal fit. (Orange) Estimation error of the total atom number. In both panels, the red lines show the error inherited from the estimation error of the total atom number due to the method shown in Fig. 5.2, while the grey lines show the *ensemble shift effect*. The black solid lines show the total estimation error of the BEC and thermal atom number, respectively, and the dashed lines show the combination of all technical contributions, including the *ensemble shift effect*

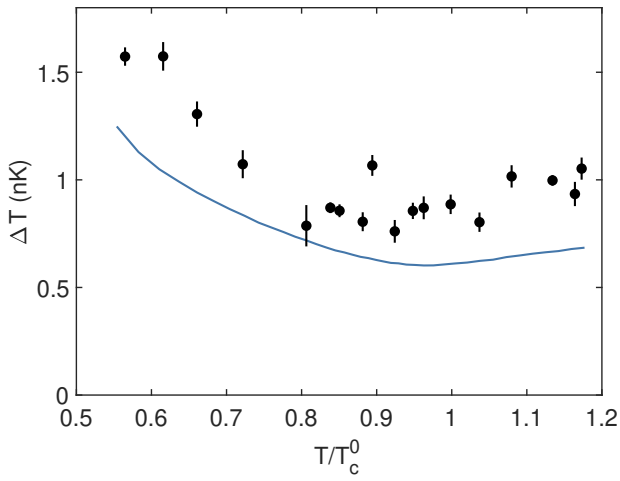

FIGURE 5.5: Spread of the temperature as a function of the reduced temperature T/T_c^0. The black points represent the measured standard deviation of the temperature within a set of 60 clouds that were prepared with the same final rf. The error bars are extracted from Eq. (2.49) using error propagation. The blue line indicates the standard deviation obtained from the Monte Carlo simulation described in Sec. 5.2.3.

hanced when using the large regions of interest necessary for studying bimodal clouds.

Figure 5.5 displays the simulated estimation error for the temperature (blue line) which is slightly lower than the spread of the experimentally obtained temperature (black points). This difference may indicate the presence of preparation noise or further noise sources affecting estimation temperature. More interestingly, it could also reflect the fundamental role of statistical ensembles. As shown in [2] the system shall be described by the microcanonical ensemble. Strictly speaking, the temperature is, therefore, not a good control parameter,

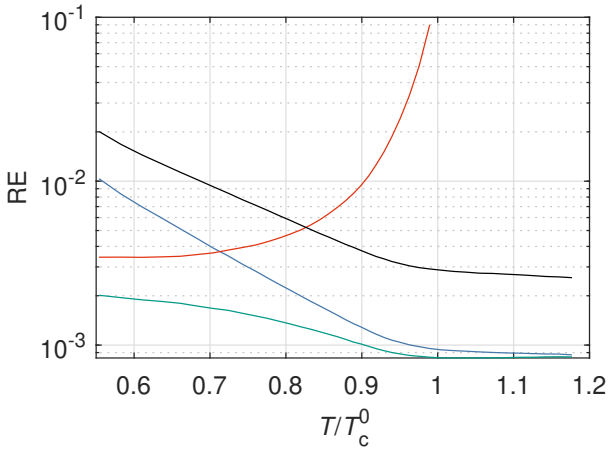

FIGURE 5.6: Relative estimation estimation errors of cloud parameters obtained from the Monte Carlo simulation in Section 5.2.3 for the BEC atom number (red), thermal atom number (blue), the total atom number (green), and temperature (black).

or, once it is used, it may fluctuate.

Relative errors

Figure 5.6 shows the relative estimations errors of the BEC, thermal and total atom number, as well as temperature. Naturally, the relative error of the BEC atom number (red) is significant for small BECs just below the critical temperature but decreases to the level of 2.5×10^{-2} towards lower temperatures as the BEC number increases and the influence of the thermal cloud reduces (see Fig. 5.4).

The precision of the thermal atom number (blue) increases from below 10^{-3} above the critical temperature to 10^{-2} at $T/T_c = 0.55$, as the relative size of the thermal cloud decreases and degrades the thermal fit. The trend of the temperature precision follows that of

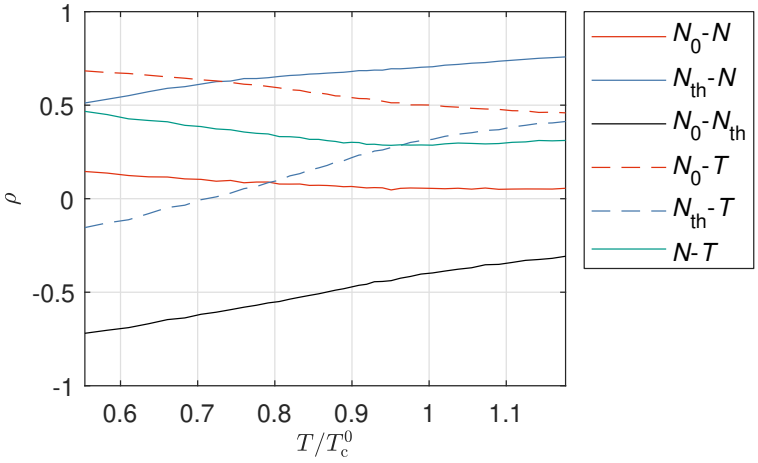

FIGURE 5.7: Correlations between estimation errors of cloud parameters.

the thermal atom number, as it is estimated from the same fit. However, with a precision below 3×10^{-3} above T_c to 2×10^{-2} for lower temperatures.

The total atom number is only slightly lower than the thermal fit above the critical temperature, but as the temperature decreases, the precision only increases to 2×10^{-3}. Thus, the total atom number is the cloud parameter that can be estimated with the highest precision for the whole temperature range.

Correlations between cloud parameters

The estimation errors induce correlations among the cloud parameters. These correlations are shown in Fig. 5.7.

N_0 exhibits a moderate correlation with N, which increases as the relative size of the wings and the BEC region decreases. Further, N_0 shows minimal correlation to T. On the other hand, N_{th} is strongly

correlated with N, with the correlation being most pronounced above T_c. Above T_c, N_{th} exhibits a moderate correlation with T above T_c, but this transitions to a slight anti-correlation at lower temperatures. Additionally, N is moderately correlated with T.

Most importantly, there exists a moderate to strong anti-correlation between N_0 and N_{th} solely from the estimation methods, indicating that observing a strong anti-correlation between these parameters does not necessarily imply particle exchange between the two components. It's worth noting that these correlations may not be intuitively deduced, which emphasise the significance of the Monte Carlo simulation in Section 5.2.3.

It is important to note that while the results mentioned above are specific to our imaging setup, the Monte Carlo simulation used to determine estimation errors can be applied to all analyses of density profiles obtained from absorption imaging.

5.2.5 Additional noise sources

The analysis presented above includes the most significant imaging effects that result in statistical errors in the parameter estimation. However, it should be mentioned that there may be other imaging effects that could potentially impact the statistical errors. Fortunately, most of these effects are primarily systematic and thus have a low impact on statistical errors. This section provides a more detailed discussion of these additional imaging effects.

Defocus, diffusion and detuning

First, the imaging system has a finite resolution due to diffraction, which roughly corresponds to the length of one camera pixel. This is associated with a depth of field of $\sim 32\,\mu m$ while the full cloud size ($6w_i$ diameter) varies from $0.5-1.1$ mm after time-of-flight, and hence,

some of the atomic distribution must be out of focus. This primarily leads to systematic effects affecting temperature estimation.

In addition, the atoms are accelerated during the imaging pulse due to momentum kicks from the probe beam followed by isotropic spontaneous emission. This introduces further defocussing with systematic consequences [36]. The recoil kicks from spontaneously emitted photons also lead to a random walk of the atoms and diffusion of the cloud during imaging, resulting in further systematic effects [36]. A simulation of our imaging setup shows that atoms typically move by less than one pixel and the resulting statistical effect is expected to be negligible.

Since $\approx$ 400 photons on average are absorbed per atom during imaging, the maximal Doppler shift at the end of the imaging pulse is $\approx$3 MHz. This will reduce the likelihood of absorption by only 20% for maximally accelerated atoms due to the high imaging power ($I_0 = 3.2\, I_{\mathrm{sat}}$) and primarily cause systematic effects. These effects are partly compensated by the calibration factor, α^*, in Eq. (3.6).

Fit discrepancy

To extract the cloud parameters the low-temperature limit of the Bose-enhanced Gaussian distribution Eq. (2.39) is used, representing the maximally peaked distribution, which is valid at the critical temperature. Using Eq. (2.39) for all temperatures introduces systematic effects as shown in Section 3.5.5. However, since N and T are highly correlated, most of this effect is, however, caught by the *correlation method*. Yet, if the correlation between temperature and total atom number is incomplete due to imperfect preparation (discussed in Sec. 5.3.2), the varying systematic effects can cause statistical effects.

Figure 5.8 shows the effect of fitting with Eq. (2.39) when the true underlying distribution is described by Eq. (2.37). To simulate this scenario, uncorrelated noise between N and T is generated follow-

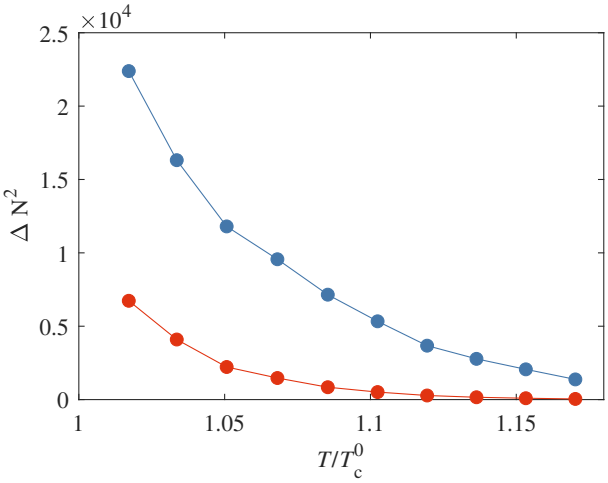

FIGURE 5.8: Impact on the variance of employing Eq. (2.39) as the fitting function above T_c, when the true underlying distribution is described by Eq. (2.37). The blue points is the result for the thermal atom number, while the red points denote the BEC atom number.

ing the method outlined in Section 5.3.2 with the preparation noise factor set to be the most probable value $\epsilon = 0.18$, as determined in Section 5.4.2. For each temperature, 1000 pairs of N and T are generated, and the chemical potential is computed for each pair by solving Eq. (2.13). The cloud widths are determined by Eq. (2.36). These parameters are then inserted in Eq. (2.37) and the distribution is fitted using Eq. (2.39). The variance is calculated for both N_0 and N_{th} after using the *correlation methods*. Note that even though there is no BEC above T_c the measurement of it remains well-defined.

Both the resulting technical noise for the N_0 (red) and N_{th} (blue) increase towards the critical temperature. The effect is most pronounced for N_{th}, reaching a maximum of nearly 2.5×10^4, which is close to a significant contribution.

Moreover, Eq. (2.39) is not the appropriate fitting function below the critical temperature as it does not account for the repulsive interaction between thermal and condensed atoms. Unfortunately, there is no applicable fitting model that takes thermal and condensed atoms into account and includes time-of-flight expansion.

Distribution noise and residual

The short time between the probe and the reference images, results in no observable fringes in the empty regions of the optical density profiles such as Fig. 5.1. However, when averaging all the residuals obtained by subtracting the thermal fit from the optical density profiles, within a measurement set, these mean residuals show some vertical fringes like those shown in Fig. 3.9. The averaging is necessary to reduce the effect of shot noise. We ascribe these fringes to some degree of astigmatism in our imaging setup which is expected to have systematic consequences for the thermal fit, but due to their static nature, the statistical effect is expected to be low.

When concentrating on a single optical density profile and subtracting both the thermal fit and the mean residual mentioned above, it should be possible to observe the pure shot noise, camera noise, and distribution noise. Figure 5.9 compares residuals from the simulation described in Sec. 5.2.3 with experimental residuals where the systematic structure discussed above has been subtracted. In the simulated results, a finite resolution of the imaging system is mimicked by performing a discrete convolution of the density profile with a Gaussian of appropriate width.

It is evident that the experimental residuals show a different structure, than those obtained from simulation. This structure is a stochastic pattern and differs for each realization. It is not well understood, but it is speculated that it could be caused by the bunching effect, lensing effects, or maybe a combination of those in the atomic cloud. It is

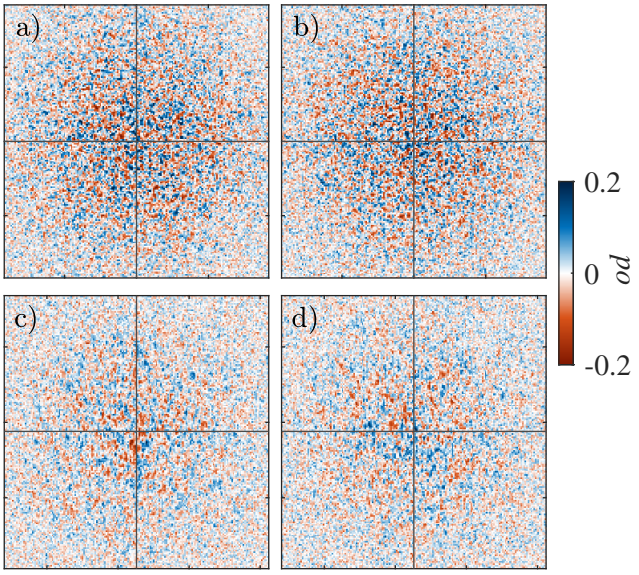

FIGURE 5.9: Residuals from individual clouds. a) and b) shows simulated residuals. c) and b) shows experimental residuals where general systematic effects (Fig. 3.9) have been subtracted.

very plausible that these structured deviations from the distribution might result in additional errors in the thermal fit.

In our Monte Carlo method, we also did not consider statistical correlations between the atoms, i.e., in the simulation, the position of each atom is drawn independently of previously "measured" positions. This approach does not account for the bunching effect in thermal atoms [123]. However, the averaging of each column density is expected to suppress the potential role of bunching in the analysis.

5.3 Fluctuation measurement noise contributions

The analysis of atom number fluctuations in BECs employs techniques beyond the regular determination of atom numbers. In particular, the *correlation method* to eliminate the effect of slow drifts can add a technical variance. Moreover, remaining uncertainties in the atom number preparation also critically impact the measurement of atom number fluctuations. This section discusses these two technical noise sources, which are specific for the measurement of atom number fluctuations.

5.3.1 Error inherited due to *correlation method*

In the analysis of atom number fluctuations, the technical drift within a measurement set is eliminated by subtracting a linear fit from the relevant atom number ($N_0(N)$ or $N_{\mathrm{th}}(N)$) as discussed in Sec. 5.1.3 and shown in Fig. 5.2. This *correlation method* was essential for the determination of BEC atom number fluctuations [2, 52].

However, due to the subtraction, the residuals of N_0 and N_{th} inherit any estimation error of the total atom number N. Such an estimation error, δN, causes a shift of N_k equal to $\delta N_k = -\frac{\mathrm{d}N_k}{\mathrm{d}N}\delta N$ where N_k can be N_0 or N_{th}. The resulting technical errors are shown in Fig. 5.4 as red lines for both the BEC (upper panel) and the thermal cloud (lower panel). The nontrivial behavior of these curves is caused by the macroscopic correlation $N_0(N)$ and $N_{\mathrm{th}}(N)$.

The slope $\mathrm{d}N_0/\mathrm{d}N$ is small in magnitude for all temperatures because it generally requires the removal of several thermal atoms to gain one atom in the BEC. Therefore, this effect is close to negligible for the BEC. On the other hand, $\mathrm{d}N_{\mathrm{th}}/\mathrm{d}N = 1 - \mathrm{d}N_0/\mathrm{d}N$ is always close to one, and the effect becomes important for the thermal clouds.

5.3.2 Ensemble shift effect

This second effect specific to measuring atom number fluctuations is due to the imperfect preparation of the atom clouds.

Experimentally, the total atom number and the temperature are highly correlated due to the evaporation process. This effect was discussed in Sec. 5.1 and shown in Fig. 5.2, which dictates the subtraction of a linear fit before evaluating the variance. However, the relationship between T and N is not completely deterministic. According to Eq. (2.11), any preparation noise in the total atom number, which is uncorrelated to the temperature, can cause variance in the BEC atom number, which is not captured by the *correlation method*. This effect is called the *ensemble shift effect,* as it corresponds to probing ensembles with different initial conditions.

In experiments, this is supported by the observation of the correlation coefficient between N and T for measurement sets at a given final radio frequency. This coefficient decreases towards colder sets, indicating that sets exposed to more evaporation cooling since the stabilization step have a relatively larger uncorrelated atom number variance.

It is straightforward to solve Eq. (2.11) numerically and simulate this effect. It depends on the uncorrelated variations in the total atom number after stabilization, which were analyzed previously [86]. Here, we use the atom numbers variance in the BEC and the thermal cloud directly to obtain the size of these uncorrelated variations.

In our model, the variance in the total atom number is divided into two parts, one that is completely correlated and one completely uncorrelated to the temperature. Assuming that no further effects influence the correlation between N and T, it is possible to extract the uncorrelated spread of the total atom number for a measurement set

$$\Delta N_{\mathrm{uncorr}} = \sqrt{\Delta N^2 - \Delta N_{\mathrm{corr}}^2} \tag{5.1}$$

where ΔN^2 is the experimentally observed variance of the total atom number and $\Delta N_{\mathrm{corr}} = \mathrm{cov}(N,T)/\Delta T$ is the correlated atom number spread, with $\mathrm{cov}(N,T)$ the observed covariance between N and T and ΔT the observed temperature spread. For each measurement set at a given final rf, one can thus obtain $\Delta N_{\mathrm{uncorr}}$ and ΔN_{corr}. Since estimation errors for N and T are not considered this variance sets an upper limit to the uncorrelated variance in the total atom number.Therefore, we use the procedure described above to find the temperature dependence of $\Delta N_{\mathrm{uncorr}}$, but we introduce a global *preparation noise parameter*, ϵ, which scales this variance.

In brief, the simulation is carried out as follows. For each temperature T, the average number N, and the variances $\Delta N_{\mathrm{uncorr}}$ and ΔN_{corr} are obtained from global fits to the data. The variance ΔN_{uncorr} is scaled with the preparation noise parameter, $\Delta N_{uncorr} = \epsilon \times N_{\mathrm{uncorr}}$ and ΔN_{corr} is chosen correspondingly to fix ΔN. Then 100,000 random atom numbers, N_j are drawn from the Gaussian distribution $\mathcal{G}(\mu = N,\ \sigma = \Delta N_{\mathrm{corr}})$. For all N_j, the corresponding temperature is found $T_j = T(N_j)$. In addition, 100,000 uncorrelated atom spreads are now drawn from $\mathcal{G}(\mu = 0,\ \sigma = \Delta N_{\mathrm{uncorr},i})$ and added element-wise to a final N_j.

The semi-ideal model is then solved for each realization of T_j and N_j. All resulting $N_{0,j}$ are plotted against N_j, and the *correlation method* in Fig. 5.2 is carried out to evaluate the variance. This is repeated for all temperatures T and for all preparation noise parameters $0 \leq \epsilon \leq 0.26$ in steps of 0.01. The result of this simulation for $\epsilon = 0.18$ is shown in Fig. 5.4 as grey lines for the BEC (upper panel) and the thermal cloud (lower panel) [2]. Note, that the effect on the BEC and thermal atom number is completely anti-correlated by

[2]Note, that the kink in the curve just below the critical temperature can be attributed to the fit of N_0 as a function of N close to the critical temperature and is not of fundamental nature.

construction, and therefore, the resulting spread is exactly the same. The consequences of the combined noise analysis are discussed in the following section.

5.4 Complete fluctuation and noise analysis

This section combines the noise contributions discussed in Sec. 5.2 and Sec. 5.3 and analyses their effect on the size of the fundamental atom number fluctuations.

5.4.1 Combination of noise

To combine the estimation errors (Sec. 5.2.3), the inherited errors from the measured total atom number N (Sec. 5.3.1), and the *ensemble shift effect* (Sec. 5.3.2), one defines the total technical noise variables as the sum of all noise contributions according to

$$N_{0,\mathrm{tech}} = N_{0,\mathrm{est}} - \frac{\mathrm{d}N_0}{\mathrm{d}N} N_{\mathrm{est}} + N_{\mathrm{ens}}(\epsilon) \tag{5.2}$$

$$N_{\mathrm{th,tech}} = N_{\mathrm{th,est}} - \frac{\mathrm{d}N_{\mathrm{th}}}{\mathrm{d}N} N_{\mathrm{est}} - N_{\mathrm{ens}}(\epsilon) \tag{5.3}$$

where $N_{0,\mathrm{est}}$, $N_{\mathrm{th,est}}$, and N_{est} are the estimation errors of the BEC, thermal, and total atom number, respectively, and $N_{\mathrm{ens}}(\epsilon)$ is the *ensemble shift effect*. Importantly, $N_{\mathrm{ens}}(\epsilon)$ depends on the choice of ϵ. Note that these are all stochastic variables with a mean value equal to zero. From Eq. (2.58), one can define

$$\mathbf{G} = \begin{pmatrix} 1 & 0 & -\frac{\mathrm{d}N_0}{\mathrm{d}N} & 1 \\ 0 & 1 & -\frac{\mathrm{d}N_{\mathrm{th}}}{\mathrm{d}N} & -1 \end{pmatrix} \tag{5.4}$$

and set up the covariance (Eq. (2.51)) from our simulation of estimation errors

$$\mathbf{\Sigma} = \begin{pmatrix} \Delta N_{0,\mathrm{est}}^2 & c_{0,\mathrm{th}} & c_{0,\mathrm{tot}} & 0 \\ c_{0,\mathrm{th}} & \Delta N_{\mathrm{th,est}}^2 & c_{\mathrm{th,tot}} & 0 \\ c_{0,\mathrm{tot}} & c_{\mathrm{th,tot}} & \Delta N_{\mathrm{sum}}^2 & 0 \\ 0 & 0 & 0 & \Delta N_{\mathrm{ens}}^2(\epsilon) \end{pmatrix}. \tag{5.5}$$

The covariances $c_{i,j}$ between the estimations errors extracted from the simulation in Sec. 5.2.3. Here, i, j stands for the BEC, the thermal and total atom number using 0, *th* and *tot*, respectively. Finally, the total technical noise contributions and their covariances can be calculated using Eq. (2.57)

$$\mathbf{G\Sigma\tilde{G}} = \begin{pmatrix} \Delta N_{0,\mathrm{tech}}^2 & c_{0,\mathrm{th,tech}} \\ c_{0,\mathrm{th,tech}} & \Delta N_{\mathrm{th,tech}}^2 \end{pmatrix}. \tag{5.6}$$

This allows us to plot the total technical error $\Delta N_{0,\mathrm{tech}}$ and $\Delta N_{\mathrm{th,tech}}$ in Fig. 5.4. For the preparation noise parameter $\epsilon = 0$, the ensemble shift disappears, and the total technical error includes only estimation errors (solid black lines). The dashed black lines represent the total technical error when choosing the best estimate for ϵ (see Sec. 5.4.2). Note importantly that the strong correlation between N_{est} and $N_{\mathrm{th,est}}$, as well as the minus sign in front of $\mathrm{d}N_{\mathrm{th}}/\mathrm{d}N$ in $\mathbf{G}$, lead to a partial cancellation of estimation error on N_{th} from fitting, and the error inherited from N. This results in the total error on N_{th} being smaller than the sum of the individual errors, highlighting the importance of using the covariance matrix in the noise analysis.

Moreover, the covariance term can be converted to a correlation, $\rho = c_{0,\mathrm{th,tech}}/(\Delta N_{0,\mathrm{tech}} \Delta N_{\mathrm{th,tech}})$. These correlations are shown in comparison with experimental results in Fig. 5.10. First, the preparation

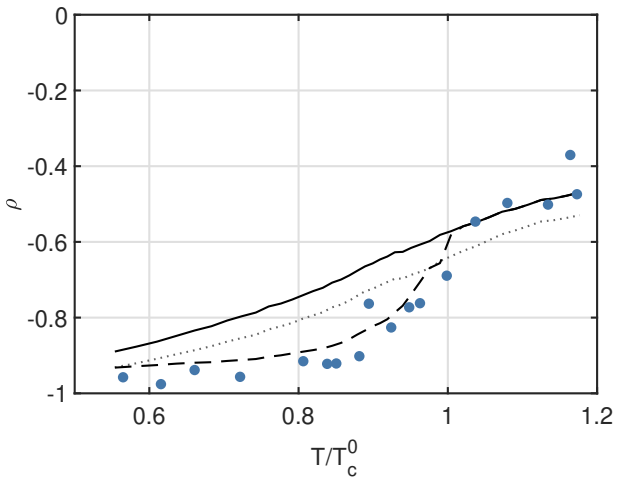

FIGURE 5.10: Correlation between the BEC and the thermal atom number. Blue points indicate the measured correlation. The dotted line is the expected correlation from estimation errors only without including the *ensemble shift effect* (see Sec. 5.3.2) extracted directly from the Monte Carlo simulation. The solid black line is the corrected correlation from estimation errors only as discussed in Sec. 5.4.2. The dashed black line represents the corrected noise model, including the estimated impact of the *ensemble shift effect*.

noise parameter, ϵ, of the *ensemble shift effect* is set to zero and plotted as a dotted black line. The experimental results are the measured correlation between the residuals of the BEC atom numbers and the thermal atom numbers shown in Fig. 5.2(b) and (d) for individual sets of 60 clouds that were prepared under the same conditions. Note that it is not the correlation between the raw measurement of the BEC and thermal cloud, which is caused by technical drift of the evaporation. The residual, after the *correlation method*, should be cleaned for this.

Importantly, the noise analysis shows a strong anti-correlation in

agreement with the experimental data. This indicates that the observed anti-correlation is introduced by the analysis technique rather than the inherent fluctuations of the atom number, as will be discussed in the Sec. 5.5.

Since the *ensemble shift effect* is absent and the fundamental fluctuations have not yet been considered, there is an expected disagreement between the measured correlations and the simulated result below the critical temperature. However, above the critical temperature, any differences indicate deficiencies in the assumptions for the Monte Carlo simulation of estimation errors. This is treated in the next section.

5.4.2 Noise analysis in fluctuation measurements

The noise analysis outlined in the previous sections and their combination using the covariance matrix lays the basis for a full analysis of the noise sources affecting the measurement of atom number fluctuations in quantum degenerate Bose gases. However, in practice, two problems arise that complicate this analysis. On the one hand, the noise analysis does not fully capture the noise observed in the absence of a BEC. Secondly, the size of the technical noise parameter, ϵ, which affects the impact of the *ensemble shift effect*, needs to be determined.

Thermal cloud noise analysis

When examining the variance of the atom number in the thermal cloud above the critical temperature in Fig. 5.11, the simulated estimation error of the thermal atom number lies below the experimental one. Moreover, the simulated anti-correlation between the BEC and the thermal atom number is too high compared to the measured quantities as shown in Fig. 5.10. Note that there is no BEC at $T/T_c^0 > 1$ such that only estimation errors are involved.

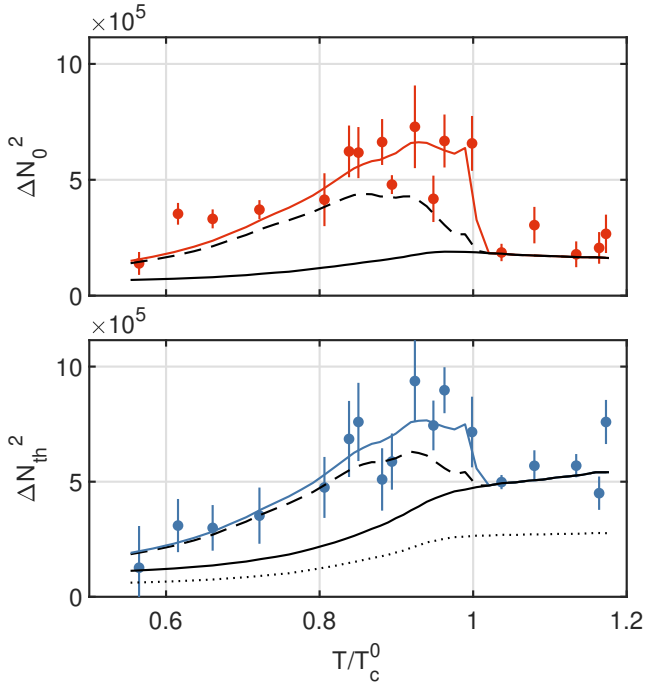

FIGURE 5.11: Variance of the BEC (upper panel) and the thermal atom number (lower panel) as a function of temperature. Data points represent the measured variance, where the error bars are obtained from Eq. (2.49). The solid black lines indicate the variance from estimation errors. In the thermal case, a dotted line indicates the estimation error extracted from the Monte Carlo simulation, while the solid line represents the correction of the simulation discussed in Sec. 5.4.2. Additionally, the dashed black lines represent the total technical noise, including the estimated impact of the *ensemble shift effect*.

Three factors impact the thermal atom number variance above the critical temperature; the estimation error on the thermal fit, the error in total atom number, and the covariance between these two. The total atom number variance should be captured well by our simulation result. This is supported by the observation that an increase in the shot noise contribution to Δod, does not significantly change the above-mentioned differences. However, we strongly suspect that the structured residuals discussed in Sec. 5.2.5 might cause larger thermal fitting errors and less correlation to the total atom number.

The above reasoning motivates an adjustment of the noise model at the level of the covariance matrix. We find that this can be achieved uniquely by increasing the estimation error of the thermal atom number by 30% and by reducing the anti-correlation of the thermal to the total atom number by 12%. This adjustment showcases the power of using the covariance matrix as a tool in this analysis. Importantly, this only affects the variance of the thermal number of atoms and now provides a realistic background value. The solid lines in Fig. 5.11 (lower panel) and Fig. 5.10 represent these changes.

Technical noise parameter determination

The second issue to be addressed is the value of the technical noise parameter, ϵ, which sets the size of the *ensemble shift effect*. To determine the best estimate of ϵ we use the following method.

For each value of ϵ the corresponding variance from the *ensemble shift effect* is inserted in $\mathbf{G}$ (Eq. (5.6)), and the total technical variance is calculated for each temperature, corresponding to dashed lines in Fig. 5.11. This variance is subtracted from the measured variance of the BEC and thermal atom number and the remaining signal is fitted with a model adapted from [2]

$$\Delta N^2_{j,\mathrm{model}}(\Delta N^2_{j,p}, T_\mathrm{p}, T) = (f * g)\,(T) \tag{5.7}$$

where f and g are given by

$$f(T) = \Delta N_{j,\mathrm{p}}^2 \left(\frac{T}{T_\mathrm{p}}\right)^3 \Theta(T_\mathrm{p} - T), \tag{5.8}$$

$$g(T) = \mathcal{N}(T, \sigma_T). \tag{5.9}$$

The two free parameters are the peak atom number variances $\Delta N_{0,\mathrm{p}}^2$, $\Delta N_{\mathrm{th,p}}^2$. The temperature of peak fluctuations T_p is set at the value already determined in [2]. Here, $\mathcal{N}(T, \sigma_T)$ is a normal distribution centered on the temperature T with a standard deviation σ_T given by the median of the measured temperature variation. The convolution of Eq. (5.8) with Eq. (5.9) accounts for the temperature spread within a set of 60 clouds.

The fit to the remaining signal is based on the sum of the normed square residuals, $\chi^2 = \sum_{i=1}^{n}[(\Delta N_j^i)^2(\epsilon) - \Delta N_{j,\mathrm{model}}^2(\Delta N_{j,p}^2, T_\mathrm{p}, T_i)]^2/e_i^2$, for the entire model with $\Delta N_{j,p}^2$ as the free parameter. Here, $(\Delta N_j^i)^2(\epsilon)$ represents the measured variances after subtracting technical noise, for the BEC $(\Delta N_0^i)^2(\epsilon)$ or the thermal cloud $(\Delta N_{\mathrm{th}}^i)^2(\epsilon)$ with the errors e_i on the measured variances, and $\Delta N_{j,\mathrm{model}}^2(\Delta N_{j,p}^2, T_i)$ is the prediction of fundamental fluctuations at the same temperatures. We determine the optimal value of ϵ by finding the value which minimizes χ^2.

Figure 5.11 includes the sum of the fit and all technical noise contributions with the optimal choice of ϵ for the BEC and the thermal fluctuations. This choice of ϵ is detailed in Fig. 5.12 which shows the peak fluctuations (upper panel), and χ^2 (lower panel), as a function of the preparation noise parameter, ϵ, for the BEC and the thermal cloud.

Importantly, Fig. 5.11 shows very good agreement between observed data and the overall noise model combined with a fit to the fundamental fluctuations. For the chosen model of the *ensemble shift effect*, fundamental fluctuations are necessary to explain the observed atom number variances. However, it is clear that extracted funda-

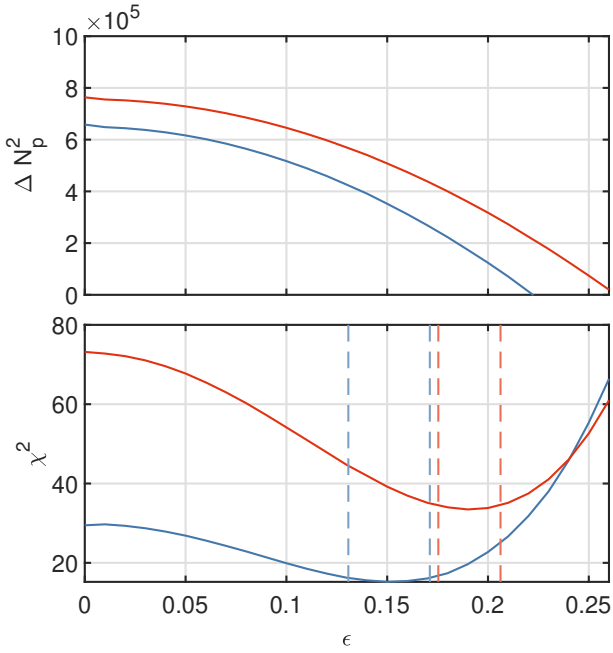

FIGURE 5.12: The upper figure shows the extracted fundamental peak fluctuations for different choices of the preparation noise parameter, ϵ, which controls the impact of the *ensemble shift effect* described in Sec. 5.3.2. The lower figure shows the χ^2 for the noise model as a whole, which includes the fit of the fundamental fluctuations. Red lines represent the analysis of the BEC data, while the thermal case is shown in blue lines. In the lower figure, the vertical dashed lines mark the 68% confidence interval for the most probable ϵ for both the BEC and thermal cloud.

mental fluctuations are sensitive to the level of the *ensemble shift effect*. The peak fluctuation amplitude at the best estimate for ϵ is $\Delta N^2_{\mathrm{p},0} = (4.1 \pm 7) \times 10^5$ and $\Delta N^2_{\mathrm{p,th}} = (2.4 \pm 8) \times 10^5$.

Figure 5.12 shows that the best estimates for the preparation noise

parameters are $\epsilon_0 = 0.191(15)$ and $\epsilon_{\mathrm{th}} = 0.15(2)$ extracted from the BEC and thermal atom number variance, respectively, with the weighted mean value for $\bar{\epsilon} = 0.18(1)$. The error correspond to the distance between the χ^2_{min} and the $\chi^2_{\mathrm{min}} + 1$ values. Within this error, there is good agreement between the two estimates for the preparation noise parameter.

Overall, it confirms that the fundamental fluctuations can indeed be measured despite the presence of the *ensemble shift effect*. However, Fig. 5.12 also demonstrates that sufficiently high values of the preparation noise parameters will impede the observation of fundamental peak fluctuations. This means that measuring atom number fluctuations requires an experiment with low technical noise rather than relying on post-selection of data.

5.5 Conclusion

Motivated by the recent observation of atom number fluctuations in weakly interacting Bose gases, this paper presents a comprehensive statistical analysis of uncertainties in the preparation and parameter estimation of partially condensed Bose gases. In particular, the combined analysis of the condensed and the thermal components also shows the presence of fluctuations in the thermal component.

Our statistical analysis consists of two parts. First, the estimation errors generally relevant for experiments using absorption imaging are analyzed. In the second part, effects specifically relevant for the measurement of atom number fluctuations are treated. These contributions are combined using the covariance matrix approach, which importantly allows for the phenomenological adjustment of individual contributions. Finally, the impact of this noise analysis on the measurement of atom number fluctuations is discussed.

The first part of the analysis shows that a Monte Carlo method can

be used to analyze the effect of photon shot noise, camera noise, finite number effects, and the image evaluation procedure. Thus, a detailed understanding of the estimation errors of the BEC and thermal cloud atom number can be gained.

The theoretically obtained estimation errors for the BEC atom number match the background value ($T/T_c^0 > 1$) of the observed BEC atom number variance ΔN_0^2 extremely well. However, our simulation does not capture the estimation errors of the larger thermal cloud equally well. Thus, the background value ($T/T_c^0 > 1$) of the thermal atom number variance ΔN_{th}^2 is underestimated. This indicates that further noise sources will have to be included in future analysis. In particular, we suspect that subtle correlations in imaging noise could significantly contribute.

Moreover, our analysis allows for an evaluation of the error in the temperature estimation. The simulated spread of the temperature is in close agreement with the experimental result. This confirms the excellent temperature resolution of the experiments of $\approx 1nK$.

The second part of our analysis considers the effects of the *correlation method* and takes imprecision in the preparation of the atomic ensembles into account. In particular, the *correlation method* is shown to lead to an additional error inherited from the estimation error of the total atom number. This only leads to a minor effect on the BEC atom number variance but contributes considerably to the variance of the thermal atom number. The method also introduces an inherent anticorrelation between the BEC and thermal atom number.

Finally, our analysis shows how noise in the preparation of the atomic samples affects variations of the BEC fraction - here called the *ensemble shift effect*. In combination with the *correlation method*, this gives rise to additional correlated noise, which emerges just below the critical temperature, increases towards lower temperature, peaking at $T/T_c^0 \approx 0.85$, and falls off slowly. Due to its slow onset as temperature decreases, it does not preclude the observation of fundamental atom

number fluctuations but affects their observed amplitude.

The complete noise analysis also shows that the parameter extraction method leads to the strong observed anticorrelation between the thermal and the BEC atom numbers. Thus, the measurement of atom number fluctuations in the thermal cloud is not an independent observation of fluctuations in a quantum degenerate Bose gas. Instead, it should be viewed as a complementary method to obtain information on the fluctuations, albeit at a larger background variance. This also shows that the expected anticorrelation between the thermal and the BEC atom numbers due to fundamental fluctuations can not be observed directly in our experiments.

Significantly, this analysis also shows that an observation of the fluctuations is not possible by post-selection of data from an experiment with large technical atom number fluctuation but precise detection.

Chapter 6

Experimental advances towards EIT

This chapter describes the three major experimental developments towards the measurement of electromagnetically induced transparency (EIT), and an existing setup capable of producing microwave radiation. Firstly, in order to trap any hyperfine level regardless of Zeeman state, a trap independent of the magnetic field is required. This is offered by a optical dipole trap. This also allows for the use of the magnetic field as a free parameter for tuning interactions via Feshbach resonances. In the process of implementing an optical dipole trap, a hybrid trap for the transition between magnetic trapping and light trapping was installed.

Secondly, to use the narrow Feshbach resonances of ^{87}Rb, precise control of the magnetic field is needed. Consequently, a magnetic field stabilization setup was developed as well as synchronisation of the experiment with the 50 Hz in the mains.

Thirdly, for measuring EIT with high precision, two lasers with extremely well-controlled frequency differences are required. This is achieved with a so-called Phase-lock setup.

Lastly, the setup facilitating versatile state preparation by generating microwave and radio frequency radiation is briefly presented.

In addition to these advancements, the group recently implemented a single photon detector (Thorlabs SPDMH2), allowing the group to demonstrate EIT now. The first objective is to measure the width of the EIT window as a function of density in the atomic cloud. Details of this will be explored in future PhD theses of the group.

To motivate the developments outlined in this chapter, two brief background sections are provided following this overview.

EIT theory sketched

EIT appears in systems where at least 3 states are coupled together by light fields [23]. In the widely employed Λ-scheme depicted in Fig. 6.1 a), two lower states, where the two lower states, $|1\rangle$ and $|2\rangle$ (which could be hyperfine sublevels), are both coupled to a common excited state $|3\rangle$, by light fields Ω_p and Ω_c, where p and c stand for probe and coupling, respectively. When all atoms in a cloud are initially prepared in state $|1\rangle$ and only a resonant probe field Ω_p is applied, the atoms will absorb photons from this field. Conversely, when a coupling field (assumed to be resonant here) is also applied to the atoms, a transparency window emerges in the absorption spectrum as illustrated in Fig. 6.1 b). The width of this window is denoted by γ_EIT.

In the dressed state picture, the presence of the coupling field generates two new eigenstates $|\pm\rangle = (|2\rangle \pm |3\rangle)/\sqrt{(2)}$ with energies $E_\pm = \pm\hbar\Omega_\mathrm{c}$ relative to the energy of level $|3\rangle$. The emergence of an EIT window in the absorption spectrum of the probe field can be understood as a result of destructive interference between these two excitation pathways [54].

Accompanying the EIT spectrum is a significant modification of the refractive properties, leading to a reduced group velocity of light [56]. The propagation of a resonant quantum probe field through a 3-level Λ-type medium resonantly coupled to Ω_c can be described as a *form-stable quantum excitation* known as a dark state polariton [55], which

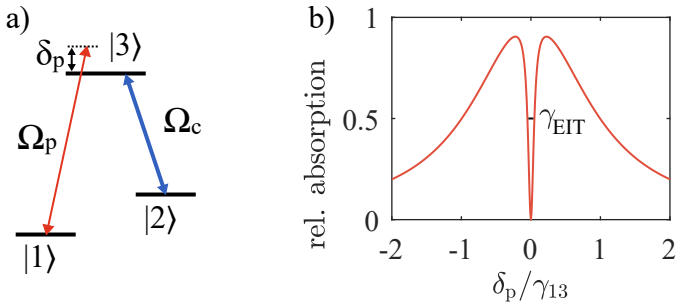

FIGURE 6.1: a) A three-level system of the Λ-configuration. b) Example of an EIT spectrum with the signature of a transmission window in the probe field's absorption spectrum. The probe field detuning, δ_p, is scaled with the decay rate from level $|3\rangle$ to $|1\rangle$. The figure is inspired by [23].

is a mixture of photonic and matter excitations. The group velocity of this propagating *quasiparticle* is determined by the mixing angle between the light and matter components, controlled by the coupling field. With a strong coupling field, the polariton is primarily a light excitation, resulting in a high group velocity. Conversely, with a weak or extinguished coupling field, the polariton is predominantly or exclusively a matter excitation, leading to a low or even zero group velocity. This behavior has stimulated interest in EIT as a potential candidate for quantum memory applications.

Polaron polaritons

In a BEC of Λ-type 3-level atoms, another quasiparticle known as the polaron polariton [61, 62] can emerge if the collisional interaction between particles in the two lower states can be tuned. In a typical EIT setup, the probe field is weak, resulting in a low occupation of the second lower state $|2\rangle$, effectively acting as an impurity. Its interaction

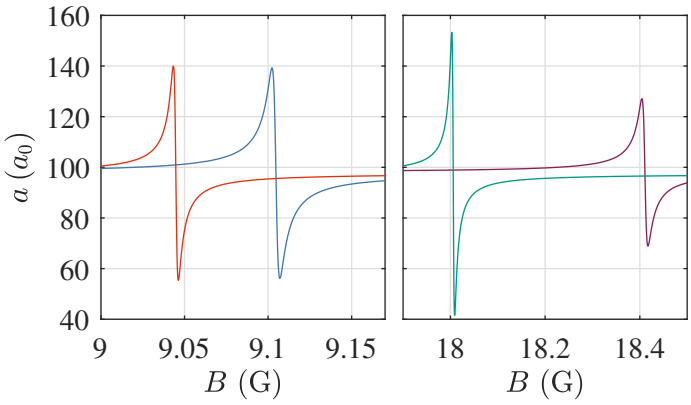

FIGURE 6.2: Most promising Feshbach resonances in ^{87}Rb for tuning of the interstate scattering length interaction, which simultaneously could serve as the ground state in an EIT lambda scheme. The resonance are for the $|1,1\rangle$ - $|2,0\rangle$ states (red), the $|1,1\rangle$ - $|2,-1\rangle$ states (blue), the $|1,0\rangle$ - $|2,-2\rangle$ states (green) and the $|1,1\rangle$ - $|2,1\rangle$ states (purple). Notice the difference in scale in the left and right panels. The widest resonance is actually the green. The resonance parameters are taken from [124].

with the surrounding medium of $|1\rangle$ atoms facilitates the formation of a polaronic quasiparticle [62], and combined with the condition for EIT, that of the polaron polariton.

The most promising Feshbach resonances in ^{87}Rb for the experimental realisation of [61, 62] are the respective groups of resonances around 9 G and 18 G, some of which are illustrated in Fig. 6.2. These resonances involve states that could serve as the ground states in a EIT lambda scheme. Given that the maximum range of commercially available Fluxgate magnetometers is currently ± 10 G [125], the $|1,1\rangle$ - $|2,-1\rangle$ resonance was chosen, despite the $|1,0\rangle$ - $|2,-2\rangle$ resonance offering better tunability. The $|1,1\rangle$ - $|2,-1\rangle$ was initially predicted in [126] and first measured in [127, 128].

6.1 Optical Dipole trap

To pave the way for EIT, an aging optical dipole trap setup detailed in [81, 82] was first revitalized. The light source for this setup originated from a 914 nm laser, akin to the repumper laser presented in Section 3.3. This laser injected another diode laser (lacking an external cavity), and the light was subsequently amplified by tapered amplifiers (TAs). Despite achieving functionality with the dipole trap, notable stability issues with both injection and TAs were encountered, and the trap had a relatively short trap lifetime. Consequently, we acquired a 20 W, 1064 nm Azurlight fiber laser and a completely new setup was constructed, as described in this section.

6.1.1 Light shift

Optical dipole trapping introduces a third trapping mechanism compared to radiation-pressure trapping (e.g., MOT) and magnetic trapping. This method relies on the electric dipole interaction with far-detuned light [129]. Classically, when an atom is subjected to an electric field, it is polarized by the induced shift of the position of the electrons compared to the positive core, creating a dipole moment of $\mathbf{p} = -e\mathbf{r} = \epsilon_0\chi_a\mathbf{E}$, where $\epsilon_0\chi_a$ is the polarizability. The energy of an induced electric dipole in an electric field is [97]

$$U = -\frac{1}{2}\epsilon_0\chi_a E^2 = \frac{1}{2}e\mathbf{r}\cdot\mathbf{E} \tag{6.1}$$

Quantum mechanically, when a two-level atom initially in the ground state is exposed to an oscillating electric field $\mathbf{E} = \mathbf{E}_0\cos(\omega t)$ generated by laser radiation, two notable effects come into play. First, it affects the population of the states of the atom through the absorption of photons from the field. For large detuning, the absorption or

scattering rate is [97]

$$R_{\text{scatt}} \simeq \frac{\Gamma}{8}\frac{\Gamma^2}{\delta^2}\frac{I}{I_{\text{sat}}}, \tag{6.2}$$

where Γ is the decay rate of the excited state, $\delta = \omega - \omega_0$ is the angular detuning with ω being the angular frequency of the light field, and ω_0 the resonance of the two-level system, I is the intensity of the light, and I_{sat} is the saturation intensity.

Secondly, it introduces a shift in the energy of the newly formed eigenstates in comparison to the original states. This is identical to the effect of the dressed state discussed in the introduction of this chapter on EIT. In the scenario of blue-detuned light, the energy of the lowest state experiences an upward shift, while for red-tuned light, the energy is lowered. For large detunings, this energy shift is given by [97]

$$U_{\text{dipole}} \simeq \frac{\hbar\Omega^2}{4\delta} = \frac{\hbar\Gamma}{8}\frac{\Gamma}{\delta}\frac{I}{I_{\text{sat}}}, \tag{6.3}$$

where Ω is the Rabi-frequency given by $\Omega = eX_{12}|\mathbf{E}_0|/\hbar$ with $X_{12} = \langle 1|\,\mathbf{r}\cdot\hat{\mathrm{e}}_{\text{rad}}\,|2\rangle$ and $\hat{\mathrm{e}}$ is the polarisation vector of the radiation. This energy shift is commonly referred to as the A.C. Stark effect or light shift. While the qualitative outcome remains the same for a real multilevel atom, it becomes crucial to consider contributions to the energy shift from all relevant transitions and their associated coupling strengths. A thorough exploration of these complexities is available in various sources, such as [129].

If the laser radiation is red-detuned and has a Gaussian intensity profile, the atoms experience a Gaussian potential. Focusing a laser beam to attain high intensities allows for the creation of a compact trap, however, only with a typical depth below 1 mK - a value dependent on laser power, beam waist, and detuning. The potential can be

expressed as

$$U_{\text{dipole}}(\mathbf{r}) = U_0 \exp\left\{\left[-2\left(\frac{x^2}{w_{0,x}^2} + \frac{y^2}{w_{0,y}^2}\right)\right]\right\} \tag{6.4}$$

with U_0 being the trap depth and the w_0's being the beam waists in the radial directions, which may differ. The confinement in the direction of the laser beam, however, is weak. Therefore, it is common practice to combine two perpendicular laser beams to achieve robust confinement in all three directions, which is also implemented in our experiment. However, more flexible geometries such as lattices [129] or box potential [130] can also be realized.

A crucial result of Eq. (6.2) and (6.3) is that the scattering rate falls off as the inverse square of the detuning, $R_{\text{scatt}} \propto 1/\delta^2$, whereas the trap depth only falls off as the inverse of the detuning, $U_{\text{dipole}} \propto 1/\delta$. Experimentally, this means that, provided the laser power necessary to achieve a specific trap depth can be achieved, an increase in detuning results in a reduction of the scattering rate. Followingly, the lifetime of atomic clouds within the trap is enhanced.

Evaporative cooling in a dipole trap is achieved by systematically reducing the power in the dipole beams. This reduction lowers the trap depth, leading to the expulsion of the hottest atoms from the trap. Consequently, the average energy within the remaining atoms decreases, facilitating the cooling process.

6.1.2 Experimental implementation

The optical setup for the dipole trap is shown schematically in Fig. 6.3. The 1064 nm laser light is outputted from a collimation unit of the 20 W, 1064 nm Azurlight fiber laser (an external seeder configuration). It passes through an optical isolator before a remotely controlled flipper mirror enables the termination of all laser light, effectively turning

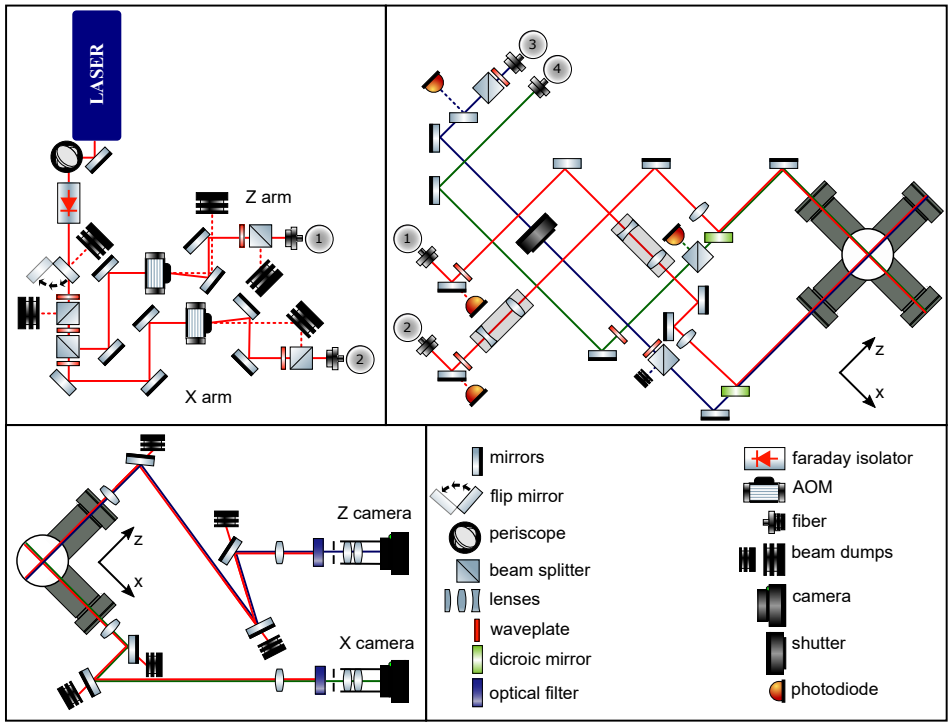

FIGURE 6.3: Schematic illustration of the optical setup for the dipole trap. The dipole beams are represented by red lines. The upper-left panel shows the setup before the coupling into optical fibers. The upper-right panel shows the laser paths leading to the science chamber. The lower-left panel demonstrates how the dipole light is dumbed by leaking through mirrors and using a 780 nm single-band bandpass filter in front of the cameras. The figure is adapted from [131].

off the dipole trap. When the flipper is raised, the light is split into two branches referred to as the *X arm* and the *Z arm*. Each branch includes an AOM that shifts the frequency upward and downward, respectively, by 80 MHz. The presence of this frequency difference prevents the two dipole beams from undergoing low-frequency beating and potentially causing heating when combined. The AOMs not only allow for the control of laser power in each beam but also facilitate rapid on-off switching of the light.

Approximately 1 W of laser light is directed into the *X arm*, while 11 W is directed into the *Z arm*. The *Z arm* is designated as the high-power branch, which is important for the hybrid trap, presented in Section 6.2. The light from the *X arm* is coupled into a Schafter & Kirchoff single mode polarisation maintaining fiber with a relatively large mode field diameter, MFD = 10.5 µm, and end-caps. For the *Z arm* a NKT Photonics single-mode 15 µm polarisation maintaining fiber (MFD = 12.6 µm) is employed to withstand the high power. The fibers guide the light to the beam-shaping setup immediately before the science chamber.

The coupling efficiencies for the AOMs are $\approx 75\,\%$ and the fiber coupling efficiencies are approximately 75 % and 84 % for *X* and *Z arms*, respectively. Consequently, there is little to gain from implementing telescopes before the AOMs and the fiber.

Power stabilization of the outcoupled light is achieved using a photodiode (Thorlabs PDA10A2) and a proportional-integral-derivative (PID) circuit that regulates the RF power to the AOM. The photodiode is strategically positioned to detect leakage through the first mirror after the outcoupling of the light. This configuration ensures that the outputted light is effectively controlled and secured against drift.

After outcoupling, the light is shaped to form a Gaussian intensity profile in the science chamber with an approximate beam waist of 80 µm using the lens setup illustrated in Fig. 6.4. An outcoupling

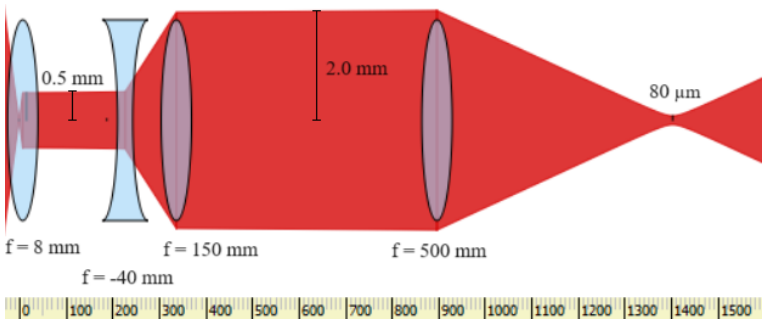

FIGURE 6.4: Schematic illustration of the optics used to generate a beam waist of around $\approx 80\,\mu$m at the position of the atoms. Figure adapted from a screenshot of GaussianBeam.

lens of $f = 8\,$mm is used to collimate the beam to a beam radius of $w = 0.5\,$mm. After this, a Galilean telescope with lenses of focal lengths $f = -40\,$mm and $f = 150\,$mm magnifies the collimated beam to $w = 2\,$mm. The focused beam is then obtained using a final convex lens with $f = 500\,$mm. The width of the beam waist is easily controlled by adjusting the position of the first collimating lens, resulting in only marginal changes in the beam waist position in the direction of the beam.

After the science chamber, the 780 nm mirrors for the imaging leak the majority of the light for the dipole trap. As a result, the light is dumped by placing beam dumps after the mirrors. The small fraction of light reaching the camera is expelled using a 780 nm optical filter (Semrock 780/12 nm BrightLine® single-band bandpass filter).

6.2 Hybrid trap

After implementing the dipole trap, the decision was made to introduce a hybrid trap, combining a dipole beam and a quadrupole (QP) trap, as presented in [132]. This hybrid configuration uses the strengths of each trap while avoiding their respective weaknesses. The QP trap benefits from tight confinement, large trap depth and fast initial evaporation, but it suffers from Majorana spin-flip losses and heating in the vicinity of the zero field point at the trap's center for low temperatures. The dipole trap, on the other hand, offers spin-independent trapping but has a relatively small trap depth, which makes it difficult to make a transition directly from an MOT. By combining these features, the hybrid trap facilitates fast and robust cooling to degeneracy.

The hybrid trap is realized by focusing a dipole beam with a vertical offset, typically ranging from one to several beam widths below the zero field point of the QP trap. The resultant combined potential of the QP trap (Eq. (3.2)) and the dipole trap (Eq. (6.4)) is

$$\begin{aligned} U_{\text{hybrid}}(\mathbf{r}) =& \mu B'(I)\sqrt{\frac{x^2}{4}+y^2+\frac{z^2}{4}}- \\ & U_0 \exp\left\{\left[-2\left(\frac{x^2}{w_{0,x}}+\frac{(y-y_0)^2}{w_{0,y}}\right)\right]\right\}+mgy, \end{aligned} \tag{6.5}$$

where y_0 is the offset between the dipole beam and the zero point of the QP field. The potential in the vertical and axial direction can be seen in Fig. 6.5 for various magnetic field gradients. In this figure, the dipole trap is configured to have a depth of $U_0/k_\mathrm{B} = 50\,\mu\mathrm{K}$ and a width of $w_0 = 80\,\mu\mathrm{m}$. For high gradients, the trap is predominantly governed by the QP potential. Lowering the gradients induces a transition from the QP trap to the hybrid trap. In scenarios with low magnetic field gradients, the potential of the dipole beam dominates in the radial

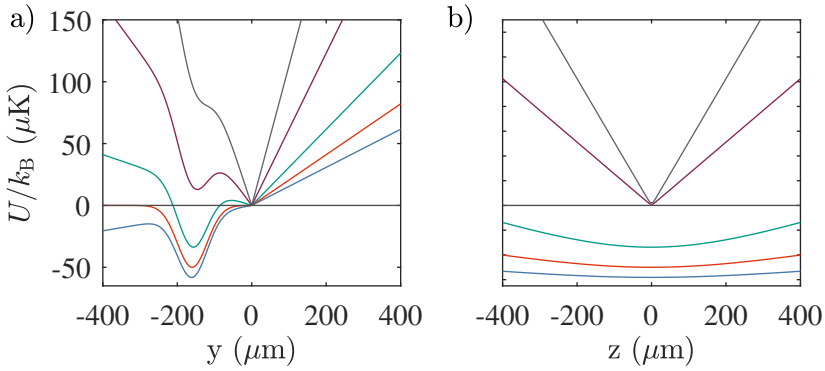

FIGURE 6.5: Illustration of the potential in the hybrid trap. a) shows the potential in the vertical direction, while b) shows the potential in the axial direction at the minimum in y. The blue, red, green and purple lines are the potential for magnetic field gradient, respectively being 0.5, 1, 2, 5, 10 B'_g (the magnetic field gradient balancing gravity for the $|F = 2, m_F = 2\rangle$ state.) The trap depth of the dipole potential is set to 50 µK.

directions, while confinement in the axial direction is provided by the QP potential, resulting in trapping frequencies given by

$$\omega_{x,y} \simeq 2\sqrt{\frac{U_0}{m w_{0,x,y}}} \quad \text{and} \quad \omega_z \simeq \frac{1}{2}\sqrt{\frac{\mu B'}{m y_{\min}}}, \tag{6.6}$$

where $y_{\min}$ is the vertical position of the potential minimum. When the magnetic field gradient is set to $B'_g = mg/\mu = 15.3$ G/cm, the QP trap exactly balances the $|F = 2, m_F = 2\rangle$ state. When setting the gradient just below this point allows continued evaporation by lowering the power in the dipole beam.

Physically, implementing the hybrid trap (with the dipole trap already set up) required removing the Ioffe coil from the QUIC trap

circuit to establish a QP trap in the science chamber. The shift in the trap center, approximately 1 to 1.5 cm, necessitated adjustments to both the Z and X-imaging setups. Finally, the beam waist of the dipole beam was positioned approximately 2 beam widths below the zero point of the QP trap.

The subsequent steps in the implementation included setting up the complete sequence for evaporation. Initially, forced evaporative cooling is conducted in a highly confining quadrupole (QP) trap. As the temperature decreases, the confinement of the QP trap is gradually reduced by decreasing the current in the QP circuit, to avoid Majorana losses and heating [132].

Once the cloud is cooled to the level where Majorana losses are unavoidable, it is transferred to the hybrid trap. This transfer is facilitated by increasing the power of a single dipole beam ($\approx$6 W) and lowering the current in the QP circuit until the magnetic field gradient is just below the value compensating for gravity. In the hybrid trap, further cooling to achieve condensation is accomplished by lowering the laser power. Alternatively, the other dipole beam can be activated, extinguishing the field gradient, and the final evaporation can be carried out in the crossed optical dipole trap.

Initially, we successfully achieved BECs containing approximately $N_0 = 10^5$ atoms in both the hybrid trap and a crossed dipole trap. Details about the evaporation sequences and their optimisation can be found in [131]. However, since then, significant enhancements have been made to the MOT, resulting in both faster evaporation and larger BEC numbers. Consequently, the current evaporation sequence differs substantially from these initial realizations.

6.3 Magnetic field stabilization

Due to the narrowness of the $|1,1\rangle$ - $|2,-1\rangle$ resonance, precise control of the magnetic field is required. This includes reducing both the magnetic field noise and the long-time drift. To address these challenges, two approaches were pursued. Firstly, a setup capable of synchronizing the experiment with the 50 Hz signal from the mains was implemented, and secondly, a setup capable of actively stabilizing the magnetic field was designed. In the following, the latter approach will be presented first. It has been designed and briefly tested but was never set up in the lab since another research result was pursued first.

6.3.1 Active stabilization

We aimed to design a setup capable of actively stabilising the magnetic field to $B_{rms} \approx 100\ \mu$G. This level of stability should be sufficient for controlling the scattering length within the practical tunable intervals of approximately 25 mG on either side of the resonance. Attaining significantly better stabilization, such as that demonstrated in works like [133], where stability reached 2.6 μG or [134] achieving stability of 18.5 μG with a long-term drift below 7 μG within 2 h, typically involves combining the active stabilization with the use of shielding materials like μ-metal. Additionally, some laboratories use the cancellation of magnetic fields at 50 Hz to enhance stability to levels below 100 μG [135], since the predominant source of magnetic field noise typically arises from 50 Hz signals in the mains.

Private conversations with the group of Carsten Klempt revealed their success in achieving stability of 40 μG through active stabilization, without the use of shielding. This, however, was for a field below 1 G, where more sensitive fluxgate sensors are available. Additionally, inspiration was drawn from [136] in successfully realizing active stabil-

ization using a PID controller implemented on a Field-Programmable Gate Array (FPGA).

The designed setup is illustrated in Fig. 6.6. The concept involves combining a setup capable of generating the major part of the field with a low-inductance setup capable of making fast corrections to the field. Both setups use a coil pair in a Helmholtz-like configuration to generate magnetic fields. Although the radii of the coils are relatively small, preventing a true Helmholtz configuration, the design achieves an essentially homogeneous field at the position of the atoms.

The first setup involves a coil pair with ≈ 200 windings and generates a field at the position of the atoms of $\approx 2\,\mathrm{G/A}$. A stable current source, delivering 5 A, enables this part of the setup to reach the Feshbach resonance at 9.1 G.

The second setup is the newly designed stabilization setup. It is designed to control the magnetic field within a small range of 500 mG around the resonance on top of the existing field generated by the first setup. At 9.1 G in one axis, the typical noise in the other two axes (of around $3-5\,\mathrm{mG}$) has a negligibly small effect on the total magnitude (on the order of tens of nG), and, thus, stabilizing the field in one direction only is sufficient.

For magnetic field measurements, a Bartington Mag-03IE1000 Fluxgate magnetometer with a range of $\pm 10\,\mathrm{G}$, sensitivity of $1\,\mathrm{V/G}$, bandwidth of 3 kHz, noise spectral density of $60-100\,\mathrm{nG}/\sqrt{\mathrm{Hz}}$ resulting in a $B_{rms} \approx 5\,\mu\mathrm{G}$, and a zero drift of $\pm 6\,\mu\mathrm{G/K}$ was employed. The sensor position is critical; it must measure the field in the exact same direction as the axis of the coil pair and with the same magnitude. Additionally, the sensor should be placed as close as possible to the atoms. In our setup such a position is achievable close to the atoms (but outside the vacuum chamber) between the coil pairs.

The sensor signal is processed through an analog circuit designed by the local electronics department. It filters the signal (cut-off frequency to be determined upon installation), subtracts 9 V using a

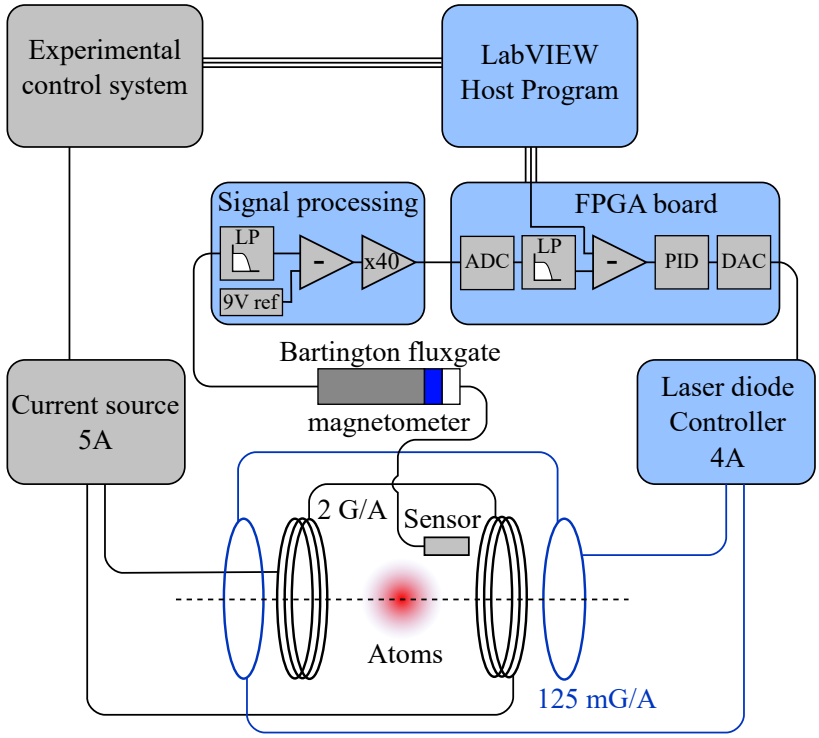

FIGURE 6.6: Illustration of the magnetic field stabilization setup. The grey boxes represent the existing setup. The blue boxes represent the newly designed magnetic field stabilization setup. The existing setup brings the field near 9 G, and the stabilization setup is designed to stabilize the field in a small range of ±250 mG around this value. A detailed explanation of the setup is given in the main text.

highly stable reference and amplifies the difference with a factor of 40. This results in an output of $\pm 10V$, corresponding to a range of ± 250 mG around 9 G. This amplification is intended to reduce the sensitivity to noise before entering the FPGA board.

The FPGA board employed is a National Instruments sbRIO 9636, controlled by a LabVIEW host program on a computer via an Ethernet connection. It has a 16-bit analog-to-digital converter (ADC) and can be configured to have differential analog input with a range of ± 10 V, resulting in the least significant bit (LSB) corresponding to 8 μG. The sampling rate is 200 kS/s. The sensor signal is passed through a digital low-pass filter. The *error signal* is generated by subtracting the sensor signal from the reference value set by the host program (determined from a ECS value). Using a digital reference value ensures that no noise or drift enters the stabilization setup from the reference value. The error signal is fed to a PID with a loop rate of 60 kS/s, and the correcting signal is outputted via a 16-bit digital-to-analog converter (DAC) with a range of ± 10 V. Note that when using a discrete sampling, it is beneficial to use a high sampling rate combined with a low-pass filter, to ensure that high-frequency noise is not interpreted as low-frequency noise.

The correcting signal is directed to the modulation analog input (± 10 V) of a 4 A laser diode controller (Thorlabs LDC 240C). This controller regulates the current in the circuit of the correcting coil pair with few windings, ensuring that it generates 125 mG/A at the position of the atoms.

As a preliminary test, the entire stabilization system, including the base setup with a coil pair of many windings, was assembled in the office, where, regrettably, the magnetic field noise was already very low. The setup demonstrated its capability by reducing the noise in the office from 270 μG to 120 μG estimated from measurements of the probe. Unfortunately, the test in the lab is yet to be conducted, and the ultimate measurement of the resulting field will be carried out

using the atom as the probe. Whether the setup can reach stability of 120 μG in a more hostile environment is an open question.

Phase shift

In a stabilization setup like this, it is crucial to consider phase shift. That is, for a given frequency, what is the delay, from measuring the signal with the sensor to the correcting signal reaching the sensor again, compared to the period of an oscillation? The largest phase shift allowed, when requiring a damping of noise, is easily calculated. To neutralize a noise contribution of angular frequency ω and amplitude, A, a corrective signal of equivalent frequency and amplitude will be generated, however, delayed by an inevitable phase ϕ. The resulting signal is:

$$S(t) = A\sin(\omega t) - A\sin(\omega t - \phi) \tag{6.7}$$

$$= 2A\sin\left(\frac{\phi}{2}\right)\cos(\omega t - \phi/2). \tag{6.8}$$

If the resulting signal should have a lower amplitude than the noise contribution, it must be required that $2\sin\phi/2 < 1$, which holds true when $\phi < 60°$. Therefore, it is crucial to avoid phase shifts (delays) in the stabilizing setup, stemming from factors such as electronics, a finite sampling rate, and changes in current in a circuit with inductance. Specifically, it is important to recognize that low-pass filters introduce phase shifts, and hence, the cut-off frequencies of these filters should be chosen carefully. Using excessively low cut-offs introduces too much phase shift, reducing the maximum frequency of the noise contributions that can be effectively mitigated. Conversely, too high cut-offs may permit unwanted high-frequency distortion in the stabilization process.

6.3.2 Clock thief circuit

The purpose of the so-called clock thief circuit is to synchronize experiments with the 50 Hz signal in the mains, ensuring that critical parts of the experiments are consistently executed at the same phase. Since the largest contribution to the magnetic field noise is 50 Hz and its odd harmonics (150 Hz, 250 Hz, 350 Hz, ...), the circuit leads to a stabilizing effect (or, at the least, a deterministic behavior) of the magnetic field. To implement the clock thief, the ECS was configured to use an external clock [1].

Secondly, an electrical circuit was designed to take a 10 MHz square wave clock signal both as input and output. The clock signal of the output, connected to ECS as the external clock, is stopped when a user initiates it by sending a digital pulse to the circuit. The circuit incorporates a feature to continuously monitor the polarity of the 50 Hz signals in the mains. The clock is then reactivated within the next $0-20$ ms as the polarity of the 50 Hz transitions from negative to positive. The design ensures that no half clock pulses are generated during the stop-and-start process. Following this step, the experimental run becomes synchronized to a specific phase of the 50 Hz signal.

Once the circuit was designed and tested, a final version was professionally manufactured by the local electronics department. This version supports external clock input from sources such as an atomic clock. Additionally, it incorporates a built-in highly stable clock with a precision of ± 50 ppb, resulting in a jitter of the full experimental run (30 s) within ± 2 µs.

The stability of the 50 Hz signal in the mains was observed to be at the 10 mHz level, equivalent to 200 ppm. If the clock thief is employed at the beginning of a 30 s experimental run, the jitter at the end of the sequence is ± 6 ms, which, compared to the 20 ms period, is nearly a random phase. However, if the clock thief is activated 1 s

[1] Despite its seemingly straightforward nature, this posed a notable challenge.

before a critical point in the experiment, the jitter reduces to $\pm 200\,\mu s$, achieving a phase synchronization precision of 1%, which is sufficient for most experimental requirements.

The clock thief circuit proves highly beneficial for critical parts of experiments with durations significantly shorter than the 20 ms period of the mains. For longer actions, reliance is placed on the active magnetic field stabilization method introduced earlier.

6.4 Phase-lock laser setup

The third large advance towards EIT is a setup capable of locking the frequencies of the two laser fields entering the EIT scheme (Fig. 6.1): the coupling field and the probe field. Locking the two lasers separately to a peak in Doppler-free saturation spectroscopy could achieve precision on the order of only 100 kHz and limit the minimum measurable width of the EIT window to around the same value. However, employing a phase-lock setup [137], enables the locking of the two lasers together with sub-hertz precision.

Originally demonstrated in the Bachelor's project of Jeppe Thuesen [138], the setup has since been completely rebuilt by Malthe Fiil Andersen. The current setup is described in detail in his progress report [139]. Briefly, the setup includes two Toptica DLC Pro external cavity diode lasers: one for the probe and the other for the coupling laser. Doppler-free saturation spectroscopy is used to lock the coupling lasers to the crossover peak between the $|F = 2\rangle$ to $|F' = 2\rangle$ and $|F' = 3\rangle$.

The probe laser is locked to the coupling laser using the OPLL (optical phase-lock loop) box presented in [137]. Here, the beat signal between the two lasers is down-converted, and a reference frequency is up-converted, such that the comparison of the two frequencies is performed in the RF regime instead of the microwave regime, which

is difficult to handle electronically. The OPLL box adjusts the piezo voltage, controlling the length of the external cavity in the probe laser and its current in order to fix the beat frequency, effectively locking the frequency difference between the two lasers to sub-hertz precision.

With the frequency difference set to 6.8 GHz, the lasers can address transitions from both the $|F = 1\rangle$ (probe) and $|F = 2\rangle$ (coupling). From these locking points, the laser fields are adjusted to the final desired frequencies using AOMs.

This lock provides not only exceptional precision but also robustness for relatively rapid changes in the set frequency. This stability enables the sweeping of the set frequency with a direct digital synthesizer (DDS) and performing measurements of the full EIT spectrum on a single cloud. For weak probe fields, this process can be even be repeated multiple times on the same cloud.

6.5 Microwave setup

The laboratory is equipped with a microwave (MW) radiation setup designed to drive transitions between the two hyperfine states of ^{87}Rb, $|F = 1\rangle$ and $|F = 2\rangle$, with a separation of 6.8 GHz. While not used for the primary results of this thesis, this setup plays a crucial role in state preparation and state manipulation for future experiments involving EIT.

The setup was originally developed during a bachelor project by Kristoffer Theis [140]. The initial setup involved mixing a ≈ 500 MHz signal from a DDS (AD9914) with a 1.75 GHz signal from a signal generator, resulting in a 2.25 GHz signal. This signal is then tripled, amplified, and emitted as radiation through antennas situated within the vacuum (similar to the antennas for RF radiation). The programmable control of the DDS allowed for the use of microwave pulses and sweeps during experimental runs. In combination with the RF radi-

ation used for evaporative cooling, this setup allows for versatile state preparation of atoms in the two hyperfine levels.

In 2022, the setup underwent revision during the master project by Maximillan Baron [141]. The original DDS was replaced with a dual-channel radio-frequency source (FlexDDS NG DUAL) from Wieserlabs Electronics. This upgrade offers enhanced flexibility in terms of pulse shapes, sweeps, and their combinations. Notably, the second channel of the FlexDDS is dedicated to RF pulses and sweeps, ensuring complete synchronization and frequency stability between microwave and RF radiations in state manipulation operations.

Chapter 7

Conclusion and Outlook

This PhD project led to four important outcomes. Firstly, it involved characterizing atom number fluctuations in Bose-Einstein condensates, underlining the importance of employing the microcanonical ensemble for accurate modeling [2]. Since this aspect was addressed in the initial phase of my PhD and comprehensively covered in [84], the focus of this thesis is on the other three outcomes.

Spatial calibration absorption imaging

In Chapter 4 a spatial calibration technique for time-of-flight absorption images of ultracold atomic clouds is presented. It is a refinement of the calibration technique introduced by Reinaudi et al. [31], incorporating an effective saturation intensity characterized by a global calibration coefficient, α^*. Our results show a significant dependence of the calibration coefficient α^* on the optical density, which is attributed to the many-body scattering processes and the re-absorption of photons [29, 30].

This calibration coefficient can be derived from radially averaged absorption images, and a practical guide to the calibration process was provided. The analysis demonstrates that this spatial calibration technique leads to corrections in detected atom numbers of up to approximately 12 % and temperature estimates of up to around 14 %

compared to previous methods. This underscores the challenge of obtaining accurate atom numbers and temperatures for ultracold atomic clouds, particularly Bose-Einstein condensates.

Future experimental work should explore the applicability of our method at lower temperatures and higher densities, particularly in the BEC regime. This will allow for a better understanding of the many-body scattering processes of atom-light interactions in dense atomic ensembles.

Statistical analysis and atom number fluctuations in BECs

In Chapter 5 a comprehensive statistical analysis of uncertainties in the preparation and the parameter estimation of partially condensed Bose gases is presented. This analysis is motivated by the recent observation of atom number fluctuations in weakly interacting BECs, with the aim of enhancing the understanding of fluctuation measurements and clarifying the relationship between fluctuations observed in the BEC and those in the thermal cloud.

The first part of the analysis shows that a Monte Carlo method can be used to analyze the effect of photon shot noise, camera noise, finite number effects, and the image evaluation procedure. This facilitates a detailed understanding of the estimation errors associated with BEC and thermal cloud atom numbers, as well as temperature, generally relevant for experiments using absorption imaging. However, the observed estimation errors of the thermal cloud are not fully explained, indicating that further noise sources will have to be included in future analyses.

The second part of the analysis considers noise sources specific to measurements of atom number fluctuations. Here, in particular, the *ensemble shift effect*, caused by preparation noise, emerges as a notable contribution. This effect peaks just below the critical temperature and

falls off at lower temperatures, resulting in a crucial impact on the measurement of atom number fluctuations.

The combined analysis demonstrates a reduction in estimated peak fluctuations compared to previous analyses. Additionally, it reveals a strong anticorrelation between thermal and BEC atom numbers due to the parameter extraction method, suggesting that the observed anticorrelation cannot be solely attributed to particle exchange between the two components.

Given the crucial role of the ensemble shift effect and preparation noise, future experimental work will focus on further reducing preparation noise. This may be accomplished by placing the atom number stabilization step later in the experimental sequence, or alternatively by implementing two- or multi-step stabilization techniques. Additionally, increasing the repetition rate of the sequence offers a direct approach to mitigate drift effects. The observed technical correlations between the BEC and thermal atom numbers could be reduced by using Bragg pulses to separate the two components, thereby enabling independent measurements. These improvements will drastically enhance the measurement of atom number fluctuations and potentially allow for the observation of particle exchange between the two components and their expected atom number anticorrelation.

In the analysis of absorption images, a more accurate fitting function for the thermal cloud in the presence of a BEC will be highly beneficial. Additionally, further efforts are required to understand the larger observed uncertainty of the thermal fit compared to the results of the Monte Carlo simulations. Potential factors contributing to this uncertainty could include bunching effects in the thermal distribution or lensing effects during imaging.

On the theoretical side, improved methods for simulating interacting Bose gases need to be developed to enable a direct comparison between theoretical predictions and experimental measurements. This could be assisted by measurements of atom number fluctuation using

atomic species with tunable interactions, which could provide valuable insights into the impact of interactions on BEC fluctuations.

Electromagnetically induced transparency

In Chapter 6, significant experimental advances towards realizing EIT are outlined. Central to these advancements is the successful integration of a new 1064 nm laser, crucial for establishing a hybrid trap and crossed optical dipole trap. These traps provide stable configurations capable of cooling to degeneracy and are now employed in all experimental operations.

Furthermore, a promising setup for magnetic field stabilization, critical for the measurement of polariton polarons, has been developed. Additionally, efforts have been made to synchronize the experiment with the 50 Hz signal from the mains, further enhancing the stability of the magnetic field.

Currently, all necessary arrangements are in place for the demonstration of EIT, with preliminary measurements already conducted on the width of the transparency window. In the near future, there are plans to characterize the EIT width as a function of optical density and real density. Following this, investigations into the realization of polaron polaritons are scheduled for examination. The magnetic field stabilization setup will be a critical ingredient for these experiments.

Additional outcomes

In addition to the main outcomes, several spin-off results emerged from the work with absorption imaging detailed in Chapter 3. These include the development of fitting software, CloudFit, now integrated into daily operations in both laboratories of the research group. Moreover, a fitting approach, including fugacity, is introduced, demonstrating

improved precision and accuracy in temperature determination clouds just above the critical temperature.

An analysis offering insights into mitigating the effects of photon shot noise in absorption imaging is also included. Finally, a simple focusing technique for the imaging setup is described.

Final remarks

This PhD project has revolved around refining the process of detecting ultracold atom clouds using absorption imaging and interpreting the results, achieved through improved calibration and a comprehensive statistical noise analysis. This has significantly contributed to our understanding of atom number fluctuations in Bose-Einstein condensates. Moreover, this PhD laid the groundwork for a new research avenue, namely the exploration of electromagnetically induced transparency, which is ongoing research.

On a personal note, this PhD journey has been a transformation. Reflecting on the remarkable difference between the bachelor's graduate joining the group and the individual writing these final words, the most significant outcome of this PhD project could arguably be the personal development experienced along the way. The work in the lab, the statistical analyses, and the contributions to the field of ultracold atoms have all been extremely satisfactory, particularly within the supportive environment of Jan Arlt's group. However, finally submitting this thesis marks a significant milestone, and I am thrilled to have reached this point.

Bibliography

[1] T. Vibel, M. Christensen, M. Kristensen, J. Thuesen, L. Stokholm, C. Weidner and J. Arlt, 'Spatial calibration of high-density absorption imaging', arXiv, 2402.06514 (2024).

[2] M. Christensen, T. Vibel, A. Hilliard, M. Kruk, K. Pawłowski, D. Hryniuk, K. Rzążewski, M. Kristensen and J. Arlt, 'Observation of microcanonical atom number fluctuations in a Bose-Einstein condensate', Phys. Rev. Lett. **126**, 153601 (2021).

[3] T. Vibel, M. Christensen, R. Andersen, L. Stokholm, K. Pawłowski, K. Rzążewski, M. Kristensen and J. Arlt, 'Atom number fluctuations in Bose gases – statistical analysis of parameter estimation', arXiv, 2403.15047 (2024).

[4] M. Planck, 'Zur Theori des Gesetzes der Energieverteilung im Normalspectrum', Verhandl. Dtsch. phys. Ges **2**, 237 (1900).

[5] A. Einstein, 'Über einen die Erzeugung und Verwandlung des Lichtes betreffenden heuristischen Gesichtspunkt', Ann. Phys. **322**, 132–148 (1905).

[6] N. Bohr, 'On the constitution of atoms and molecules', Philos. Mag. **26**, 476–502 (1913).

[7] J. Bardeen and W. H. Brattain, 'The Transistor, A Semi-Conductor Triode', Phys. Rev. **74**, 230–231 (1948).

[8] T. H. Maiman, 'Stimulated optical radiation in ruby', Nature **187**, 493–494 (1960).

[9] J. P. Dowling and G. J. Milburn, 'Quantum technology: The second quantum revolution', Philos. Trans. Roy. Soc. London **361**, 1655–1674 (2003).

[10] C. L. Degen, F. Reinhard and P. Cappellaro, 'Quantum sensing', Rev. Mod. Phys. **89**, 035002 (2017).

[11] S. Pirandola, S. Pirandola, U. L. Andersen, L. Banchi, M. Berta, D. Bunandar, R. Colbeck, D. Englund, T. Gehring, C. Lupo, C. Ottaviani, J. L. Pereira, M. Razavi, J. S. Shaari, J. S. Shaari, M. Tomamichel, M. Tomamichel, V. C. Usenko, G. Vallone, P. Villoresi and P. Wallden, 'Advances in quantum cryptography', Adv. Opt. Photonics **12**, 1012–1236 (2020).

[12] I. M. Georgescu, S. Ashhab and F. Nori, 'Quantum simulation', Rev. Mod. Phys. **86**, 153–185 (2014).

[13] T. D. Ladd, F. Jelezko, R. Laflamme, Y. Nakamura, C. Monroe and J. L. O'Brien, 'Quantum computers', Nature **464**, 45–53 (2010).

[14] A. Einstein, 'Quantentheorie des einatomigen idealen Gases', SB Preuss. Akad. Wiss. phys.-math. Klasse (1924).

[15] S. N. Bose, 'Plancks Gesetz und Lichtquantenhypothese', Zeitschrift für Physik **26**, 178–181 (1924).

[16] M. H. Anderson, J. R. Ensher, M. R. Matthews, C. E. Wieman and E. A. Cornell, 'Observation of Bose-Einstein condensation in a dilute atomic vapor', Science **269**, 198–201 (1995).

[17] K. B. Davis, M. O. Mewes, M. R. Andrews, N. J. van Druten, D. S. Durfee, D. M. Kurn and W. Ketterle, 'Bose-Einstein condensation in a gas of sodium atoms', Phys. Rev. Lett. **75**, 3969–3973 (1995).

[18] C. C. Bradley, C. A. Sackett, J. J. Tollett and R. G. Hulet, 'Evidence of Bose-Einstein condensation in an atomic gas with attractive interactions', Phys. Rev. Lett. **75**, 1687–1690 (1995).

[19] *Ultracold Atom News*, https://ucan.physics.utoronto.ca/research-groups/ (visited on 06/02/2024).

[20] K. Bongs, M. Holynski, J. Vovrosh, P. Bouyer, G. Condon, E. Rasel, C. Schubert, W. P. Schleich and A. Roura, 'Taking atom interferometric quantum sensors from the laboratory to real-world applications', Nat. Rev. Phys. **1**, 731–739 (2019).

[21] I. Bloch, J. Dalibard and S. Nascimbène, 'Quantum simulations with ultracold quantum gases', Nat. Phys. **8**, 267–276 (2012).

[22] C. Fertig and K. Gibble, 'Measurement and cancellation of the cold collision frequency shift in an 87-Rb fountain clock', Phys. Rev. Lett. **85**, 1622–1625 (2000).

[23] R. Finkelstein, S. Bali, O. Firstenberg and I. Novikova, 'A practical guide to electromagnetically induced transparency in atomic vapor', New J. Phys. **25**, 035001 (2023).

[24] M. T. DePue, S. Lukman Winoto, D. Han and D. S. Weiss, 'Transient compression of a MOT and high intensity fluorescent imaging of optically thick clouds of atoms', Opt. Commun. **180**, 73–79 (2000).

[25] K. Jooya, N. Musterer, K. W. Madison and J. L. Booth, 'Photon-scattering-rate measurement of atoms in a magneto-optical trap', Phys. Rev. A **88**, 063401 (2013).

[26] A. Ramanathan, S. R. Muniz, K. C. Wright, R. P. Anderson, W. D. Phillips, K. Helmerson and G. K. Campbell, 'Partial-transfer absorption imaging: A versatile technique for optimal imaging of ultracold gases', Rev. Sci. Instrum. **83**, 083119 (2012).

[27] M. Pappa, P. C. Condylis, G. O. Konstantinidis, V. Bolpasi, A. Lazoudis, O. Morizot, D. Sahagun, M. Baker and W. von Klitzing, 'Ultra-sensitive atom imaging for matter-wave optics', New J. Phys. **13**, 115012 (2011).

[28] A. Reinhard, J.-F. Riou, L. A. Zundel and D. S. Weiss, 'Dark-ground imaging of high optical thickness atom clouds', Opt. Commun. **324**, 30–33 (2014).

[29] R. Veyron, V. Mancois, J.-B. Gerent, G. Baclet, P. Bouyer and S. Bernon, 'Quantitative absorption imaging: The role of incoherent multiple scattering in the saturating regime', Phys. Rev. Research **4**, 033033 (2022).

[30] R. Veyron, V. Mancois, J. B. Gerent, G. Baclet, P. Bouyer and S. Bernon, 'Effective two-level approximation of a multilevel system driven by coherent and incoherent fields', Phys. Rev. A **105**, 043105 (2022).

[31] G. Reinaudi, T. Lahaye, Z. Wang and D. Guéry-Odelin, 'Strong saturation absorption imaging of dense clouds of ultracold atoms', Opt. Lett. **32**, 3143 (2007).

[32] L. Niu, X. Guo, Y. Zhan, X. Chen, W. M. Liu and X. Zhou, 'Optimized fringe removal algorithm for absorption images', Appl. Phys. Lett. **113**, 144103 (2018).

[33] G. Ness, A. Vainbaum, C. Shkedrov, Y. Florshaim and Y. Sagi, 'Single-exposure absorption imaging of ultracold atoms using deep learning', Phys. Rev. Appl. **14**, 014011 (2020).

[34] B. Song, C. He, Z. Ren, E. Zhao, J. Lee and G.-B. Jo, 'Effective statistical fringe removal algorithm for high-sensitivity imaging of ultracold atoms', Phys. Rev. Appl. **14**, 034006 (2020).

[35] A. Putra, D. L. Campbell, R. M. Price, S. De and I. B. Spielman, 'Optimally focused cold atom systems obtained using density-density correlations', Rev. Sci. Instrum. **85**, 013110 (2014).

[36] W. Muessel, H. Strobel, M. Joos, E. Nicklas, I. Stroescu, J. Tomkovič, D. B. Hume and M. K. Oberthaler, 'Optimized absorption imaging of mesoscopic atomic clouds', Appl. Phys. B **113**, 69–73 (2013).

[37] K. Hueck, N. Luick, L. Sobirey, J. Siegl, T. Lompe, H. Moritz, L. W. Clark and C. Chin, 'Calibrating high intensity absorption imaging of ultracold atoms', Opt. Express **25**, 8670 (2017).

[38] J. W. Mikhail Konnik, 'High-level numerical simulations of noise in CCD and CMOS photosensors: review and tutorial', arXiv, 1412.4031 (2014).

[39] R. M. Ziff, G. E. Uhlenbeck and M. Kac, 'The ideal Bose-Einstein gas, revisited', Phys. Rep. **32**, 169–248 (1977).

[40] H. D. Politzer, 'Condensate fluctuations of a trapped, ideal Bose gas', Phys. Rev. A **54**, 5048–5054 (1996).

[41] V. V. Kocharovsky, V. V. Kocharovsky, M. Holthaus, C. Raymond Ooi, A. Svidzinsky, W. Ketterle and M. O. Scully, 'Fluctuations in ideal and interacting Bose–Einstein condensates: From the laser phase transition analogy to squeezed states and Bogoliubov quasiparticles', in *Advances in atomic, molecular, and optical physics* (Elsevier, 2006), pp. 291–411.

[42] E. Schrödinger, *Statistical thermodynamics* (Dover Publications, New York, 1989).

[43] D. V. Schroeder, *An introduction to thermal physics*, First edition (Pearson, 2014).

[44] P. Navez, D. Bitouk, M. Gajda, Z. Idziaszek and K. Rzążewski, 'Fourth statistical ensemble for the Bose-Einstein condensate', Phys. Rev. Lett. **79**, 1789–1792 (1997).

[45] M. Holthaus, E. Kalinowski and K. Kirsten, 'Condensate fluctuations in trapped Bose gases: Canonical vs. microcanonical ensemble', Ann. Phys. **270**, 198–230 (1998).

[46] J. Szczepkowski, R. Gartman, M. Witkowski, L. Tracewski, M. Zawada and W. Gawlik, 'Analysis and calibration of absorptive images of Bose-Einstein condensate at nonzero temperatures', Rev. Sci. Instrum. **80**, 053103 (2009).

[47] W. Ketterle, D. S. Durfee and D. M. Stamper-Kurn, *Making, probing and understanding Bose-Einstein condensates*, 1999.

[48] D. Genkina, L. M. Aycock, B. K. Stuhl, H.-I. Lu, R. A. Williams and I. B. Spielman, 'Feshbach enhanced s-wave scattering of fermions: Direct observation with optimized absorption imaging', New J. Phys. **18**, 013001 (2015).

[49] M. Horikoshi, A. Ito, T. Ikemachi, Y. Aratake, M. Kuwata-Gonokami and M. Koashi, 'Appropriate probe condition for absorption imaging of ultracold 6Li atoms', J. Phys. Soc. Jpn. **86**, 104301 (2017).

[50] B. Lücke, 'Multi-particle entanglement in a spinor Bose-Einstein condensate for quantum-enhanced interferometry', PhD thesis (Gottfried Wilhelm Leibniz Universität Hannover, 2014).

[51] C. F. Ockeloen, A. F. Tauschinsky, R. J. C. Spreeuw and S. Whitlock, 'Detection of small atom numbers through image processing', Phys. Rev. A **82**, 061606 (2010).

[52] M. Kristensen, M. Christensen, M. Gajdacz, M. Iglicki, K. Pawłowski, C. Klempt, J. Sherson, K. Rzążewski, A. Hilliard and J. Arlt, 'Observation of atom number fluctuations in a Bose-Einstein condensate', Phys. Rev. Lett. **122**, 163601 (2019).

[53] S. E. Harris, 'Electromagnetically induced transparency', Phys. Today **50**, 36–42 (1997).

[54] M. Fleischhauer, A. Imamoglu and J. P. Marangos, 'Electromagnetically induced transparency: Optics in coherent media', Rev. Mod. Phys. **77**, 633–673 (2005).

[55] M. Fleischhauer and M. D. Lukin, 'Dark-state polaritons in electromagnetically induced transparency', Phys. Rev. Lett. **84**, 5094–5097 (2000).

[56] L. V. Hau, S. E. Harris, Z. Dutton and C. H. Behroozi, 'Light speed reduction to 17 metres per second in an ultracold atomic gas', Nature **397**, 594–598 (1999).

[57] M. D. Lukin, 'Colloquium: Trapping and manipulating photon states in atomic ensembles', Rev. Mod. Phys. **75**, 457–472 (2003).

[58] C. Liu, Z. Dutton, C. H. Behroozi and L. V. Hau, 'Observation of coherent optical information storage in an atomic medium using halted light pulses', Nature **409**, 490–493 (2001).

[59] R. G. Beausoleil, W. J. Munro, D. A. Rodrigues and T. P. Spiller, 'Applications of electromagnetically induced transparency to quantum information processing', J. Mod. Opt. **51**, 2441–2448 (2004).

[60] S.-H. Wei, B. Jing, X.-Y. Zhang, J.-Y. Liao, C.-Z. Yuan, B.-Y. Fan, C. Lyu, D.-L. Zhou, Y. Wang, G.-W. Deng, H.-Z. Song, D. Oblak, G.-C. Guo and Q. Zhou, 'Towards real-world quantum networks: A review', Laser Photonic Rev. **16**, 2100219 (2022).

[61] A. Camacho-Guardian, K. K. Nielsen, T. Pohl and G. M. Bruun, 'Polariton dynamics in strongly interacting quantum many-body systems', Phys. Rev. Research **2**, 023102 (2020).

[62] K. K. Nielsen, A. Camacho-Guardian, G. M. Bruun and T. Pohl, 'Superfluid flow of polaron polaritons above Landau's critical velocity', Phys. Rev. Lett. **125**, 035301 (2020).

[63] C. J. Pethick and H. Smith, *Bose-Einstein condensation in dilute gases*, Second Edition (Cambridge, 2008).

[64] J. T. M. Walraven, *Quantum gases lectures*, University of Amsterdam, Oct. 2019.

[65] F. Dalfovo, S. Giorgini, L. P. Pitaevskii and S. Stringari, 'Theory of Bose-Einstein condensation in trapped gases', Rev. Mod. Phys. **71**, 463–512 (1999).

[66] M. Naraschewski and D. M. Stamper-Kurn, 'Analytical description of a trapped semi-ideal Bose gas at finite temperature', Phys. Rev. A **58**, 2423–2426 (1998).

[67] M.-O. Mewes, M. R. Andrews, N. J. van Druten, D. M. Kurn, D. S. Durfee and W. Ketterle, 'Bose-Einstein condensation in a tightly confining dc magnetic trap', Phys. Rev. Lett. **77**, 416–419 (1996).

[68] J. R. Ensher, D. S. Jin, M. R. Matthews, C. E. Wieman and E. A. Cornell, 'Bose-Einstein condensation in a dilute gas: Measurement of energy and ground-state occupation', Phys. Rev. Lett. **77**, 4984–4987 (1996).

[69] M. Kruk, D. Hryniuk, M. Kristensen, T. Vibel, K. Pawłowski, J. Arlt and K. Rzążewski, 'Microcanonical and canonical fluctuations in atomic Bose-Einstein condensates – Fock state sampling approach', SciPost Phys. **14**, 036 (2023).

[70] M. Plischke and B. Bergersen, *Equilibrium statistical physics*, Third edition (World Scientific, 2006).

[71] C. Weiss and M. Wilkens, 'Particle number counting statistics in ideal Bose gases', Opt. Express **1**, 272 (1997).

[72] M. Gajda and K. Rzążewski, 'Fluctuations of Bose-Einstein condensate', Phys. Rev. Lett. **78**, 2686–2689 (1997).

[73] M. Kristensen, 'Atom number fluctuations in Bose-Einstein condensates', PhD thesis (Aarhus University, July 2018).

[74] Y. Castin and R. Dum, 'Bose-Einstein condensates in time dependent traps', Phys. Rev. Lett. **77**, 5315–5319 (1996).

[75] Y. Kagan, E. L. Surkov and G. V. Shlyapnikov, 'Evolution of a Bose-condensed gas under variations of the confining potential', Phys. Rev. A **54**, R1753–R1756 (1996).

[76] R. J. Barlow, *Statistics: a guide to the use of statistical methods in the physical sciences*, edited by D. J. Sandiford, F. Mandl and A. C. Phillips (Wiley, 1997).

[77] D. B. Hume, I. Stroescu, M. Joos, W. Muessel, H. Strobel and M. K. Oberthaler, 'Accurate atom counting in mesoscopic ensembles', Phys. Rev. Lett. **111**, 253001 (2013).

[78] E. Cho and M. J. Cho, 'Variance of sample variance with replacement', Int. J. Pure. Appl. Math **52**, 43–47 (2009).

[79] I. G. Hughes and T. P. A. Hase, *Measurements and their uncertainties: a practical guide to modern error analysis* (Oxford University Press, 2010).

[80] J. F. Bertelsen, 'Ultracold atomic gases, mixtures and molecules', PhD thesis (Aarhus University, Aug. 2007).

[81] H. K. Andersen, 'Bose-Einstein condensates in optical lattices', PhD thesis (Sept. 2008).

[82] P. L. Pedersen, 'Multi-mode spin dynamics of a Bose-Einstein condensate in an optical lattice', PhD thesis (Aug. 2014).

[83] M. Gajdacz, 'Non-destructive imaging and feedback with ultracold gases', PhD thesis (Aarhus University, July 2015).

[84] M. B. Christensen, 'Microcanonical fluctuations in interacting Bose-Einstein condensates', PhD thesis (Aarhus University, July 2020).

[85] T. Esslinger, I. Bloch and T. W. Hänsch, 'Bose-Einstein condensation in a quadrupole-Ioffe-configuration trap', Phys. Rev. A **58**, R2664–R2667 (1998).

[86] M. Gajdacz, A. J. Hilliard, M. A. Kristensen, P. L. Pedersen, C. Klempt, J. J. Arlt and J. F. Sherson, 'Preparation of ultracold atom clouds at the shot noise level', Phys. Rev. Lett. **117**, 073604 (2016).

[87] M. Kristensen, M. Gajdacz, P. Pedersen, C. Klempt, J. Sherson, J. Arlt and A. Hilliard, 'Sub-atom shot noise Faraday imaging of ultracold atom clouds', J. Phys. B: At., Mol. Opt. Phys. **50**, 034004 (2017).

[88] D. A. Steck, *Rubidium 87 D line data*, http://steck.us/alkalidata/, 2019.

[89] K. B. Davis, M.-O. Mewes, M. A. Joffe, M. R. Andrews and W. Ketterle, 'Evaporative cooling of sodium atoms', Phys. Rev. Lett. **74**, 5202–5205 (1995).

[90] W. Ketterle and N. V. Druten, *Advances in atomic, molecular, and optical physics* (Elsevier, 1996).

[91] A. Marte, T. Volz, J. Schuster, S. Dürr, G. Rempe, E. G. M. van Kempen and B. J. Verhaar, 'Feshbach resonances in rubidium 87: Precision measurement and analysis', Phys Rev Lett **89**, 283202 (2002).

[92] C. Chin, R. Grimm, P. Julienne and E. Tiesinga, 'Feshbach resonances in ultracold gases', Rev. Mod. Phys. **82**, 1225–1286 (2010).

[93] G. Camy, C. Bordé and M. Ducloy, 'Heterodyne saturation spectroscopy through frequency modulation of the saturating beam', Opt. Commun. **41**, 325–330 (1982).

[94] V. Negnevitsky and L. D. Turner, 'Wideband laser locking to an atomic reference with modulation transfer spectroscopy', Opt. Express **21**, 3103 (2013).

[95] H. K. Andersen, 'Opbygning af et rubidium MOT lasersystem', MA thesis (Aarhus University, Oct. 2003).

[96] H. J. Metcalf and P. van der Straten, *Laser cooling and trapping* (Springer New York, 1999).

[97] C. J. Foot, *Atomic physics*, Oxford Master Series in Physics (Oxford University Press, Aug. 2011).

[98] H. J. Lewandowski, D. M. Harber, D. L. Whitaker and E. A. Cornell, 'Simplified system for creating a Bose–Einstein condensate', J. Low Temp. Phys. **132**, 309–367 (2003).

[99] E. Hecht, *Optics*, edited by J. Berrisford, Third edition (Addison Wesley Longman, 1998).

[100] R. M. Corless, G. H. Gonnet, D. E. G. Hare, D. J. Jeffrey and D. E. Knuth, 'On the LambertW function', Adv. Comput. Math **5**, 329–359 (1996).

[101] R. Veyron, V. Mancois, J.-B. Gerent, G. Baclet, P. Bouyer and S. Bernon, 'Quantitative absorption imaging of optically dense effective two-level systems', ArXiv, 2110.12505 (2021).

[102] P. W. Milonni and J. H. Ebberly, *Laser physics* (John Wiley and Sons, Inc., 2010).

[103] G. C. Bjorklund, M. D. Levenson, W. Lenth and C. Ortiz, 'Frequency modulation (FM) spectroscopy', Appl. Phys. B **32**, 145–152 (1983).

[104] K. S. Hardman, P. B. Wigley, P. J. Everitt, P. Manju, C. C. N. Kuhn and N. P. Robins, 'Time-of-flight detection of ultra-cold atoms using resonant frequency modulation imaging', Opt. Lett. **41**, 2505 (2016).

[105] C. C. Bradley, C. A. Sackett and R. G. Hulet, 'Bose-Einstein condensation of lithium: Observation of limited condensate number', Phys. Rev. Lett. **78**, 985–989 (1997).

[106] M. R. Andrews, D. M. Kurn, H.-J. Miesner, D. S. Durfee, C. G. Townsend, S. Inouye and W. Ketterle, 'Propagation of sound in a Bose-Einstein condensate', Phys. Rev. Lett. **79**, 553–556 (1997).

[107] R. Meppelink, R. A. Rozendaal, S. B. Koller, J. M. Vogels and P. van der Straten, 'Thermodynamics of Bose-Einstein-condensed clouds using phase-contrast imaging', Phys. Rev. A **81**, 053632 (2010).

[108] V. Savalli, G. Z. K. Horvath, P. D. Featonby, L. Cognet, N. Westbrook, C. I. Westbrook and A. Aspect, 'Optical detection of cold atoms without spontaneous emission', Opt. Lett. **24**, 1552–1554 (1999).

[109] S. Kadlecek, J. Sebby, R. Newell and T. G. Walker, 'Nondestructive spatial heterodyne imaging of cold atoms', Opt. Lett. **26**, 137–139 (2001).

[110] L. D. Turner, K. P. Weber, D. Paganin and R. E. Scholten, 'Off-resonant defocus-contrast imaging of cold atoms', Opt. Lett. **29**, 232–234 (2004).

[111] L. D. Turner, K. F. E. M. Domen and R. E. Scholten, 'Diffraction-contrast imaging of cold atoms', Phys. Rev. A **72**, 031403 (2005).

[112] P. B. Wigley, P. J. Everitt, K. S. Hardman, M. R. Hush, C. H. Wei, M. A. Sooriyabandara, P. Manju, J. D. Close, N. P. Robins and C. C. N. Kuhn, 'Non-destructive shadowgraph imaging of ultra-cold atoms', Opt. Lett. **41**, 4795–4798 (2016).

[113] A. R. Perry, S. Sugawa, F. Salces-Carcoba, Y. Yue and I. B. Spielman, 'Multiple-camera defocus imaging of ultracold atomic gases', Opt. Express **29**, 17029–17041 (2021).

[114] M. Gajdacz, P. Pedersen, T. Mørch, A. Hilliard, J. Arlt and J. Sherson, 'Non-destructive Faraday imaging of dynamically controlled ultracold atoms', Rev. Sci. Instrum. **84**, 083105 (2013).

[115] O. Elíasson, R. Heck, J. S. Laustsen, M. Napolitano, R. Müller, M. G. Bason, J. J. Arlt and J. F. Sherson, 'Spatially-selective in situ magnetometry of ultracold atomic clouds', J. Phys. B: At. Mol. Opt. Phys. **52**, 075003 (2019).

[116] P. van der Straten and H. Metcalf, *Atoms and molecules interacting with light: Atomic physics for the laser era* (Cambridge, 2016).

[117] E. W. Streed, A. Jechow, B. G. Norton and D. Kielpinski, 'Absorption imaging of a single atom', Nat. Commun. **3**, 933 (2012).

[118] A. Hüper, C. Pür, M. Hetzel, J. Geng, J. Peise, I. Kruse, M. Kristensen, W. Ertmer, J. Arlt and C. Klempt, 'Number-resolved preparation of mesoscopic atomic ensembles', New J. Phys. **23**, 113046 (2021).

[119] Y.-C. Chen, Y.-A. Liao, L. Hsu and I. A. Yu, 'Simple technique for directly and accurately measuring the number of atoms in a magneto-optical trap', Phys. Rev. A **64**, 031401 (2001).

[120] H.-W. Cho, Y.-C. He, T. Peters, Y.-H. Chen, H.-C. Chen, S.-C. Lin, Y.-C. Lee and I. A. Yu, 'Direct measurement of the atom number in a Bose condensate', Opt. Express **15**, 12114–12122 (2007).

[121] R. Bücker, A. Perrin, S. Manz, T. Betz, C. Koller, T. Plisson, J. Rottmann, T. Schumm and J. Schmiedmayer, 'Single-particle-sensitive imaging of freely propagating ultracold atoms', New J. Phys. **11**, 103039 (2009).

[122] F. Gerbier, J. H. Thywissen, S. Richard, M. Hugbart, P. Bouyer and A. Aspect, 'Critical temperature of a trapped, weakly interacting Bose gas', Phys. Rev. Lett. **92**, 030405 (2004).

[123] E. A. Burt, R. W. Ghrist, C. J. Myatt, M. J. Holland, E. A. Cornell and C. E. Wieman, 'Coherence, correlations, and collisions: What one learns about Bose-Einstein condensates from their decay', Phys. Rev. Lett. **79**, 337–340 (1997).

[124] A. M. Kaufman, R. P. Anderson, T. M. Hanna, E. Tiesinga, P. S. Julienne and D. S. Hall, 'Radio-frequency dressing of multiple Feshbach resonances', Phys. Rev. A **80**, 050701 (2009).

[125] A. Grosz, M. J. Haji-Sheikh and S. C. Mukhopadhyay, *High sensitivity magnetometers*, Vol. 19, Smart Sensors, Measurement and Instrumentation (Springer International Publishing, 2017).

[126] E. G. M. van Kempen, S. J. J. M. F. Kokkelmans, D. J. Heinzen and B. J. Verhaar, 'Interisotope determination of ultracold rubidium interactions from three high-precision experiments', Phys. Rev. Lett. **88**, 093201 (2002).

[127] M. Erhard, H. Schmaljohann, J. Kronjäger, K. Bongs and K. Sengstock, 'Measurement of a mixed-spin-channel Feshbach resonance in 87-Rb', Phys. Rev. A **69**, 032705 (2004).

[128] A. Widera, O. Mandel, M. Greiner, S. Kreim, T. W. Hänsch and I. Bloch, 'Entanglement interferometry for precision measurement of atomic scattering properties', Phys. Rev. Lett. **92**, 160406 (2004).

[129] R. Grimm, M. Weidemüller and Y. B. Ovchinnikov, 'Optical dipole traps for neutral atoms', in *Advances in atomic, molecular, and optical physics* (Elsevier, 2000), pp. 95–170.

[130] A. L. Gaunt, T. F. Schmidutz, I. Gotlibovych, R. P. Smith and Z. Hadzibabic, 'Bose-Einstein condensation of atoms in a uniform potential', Phys. Rev. Lett. **110**, 200406 (2013).

[131] L. N. Stokholm, 'Implementing two laser based traps for cooling to quantum degeneracy', MA thesis (Aarhus university, Sept. 2022).

[132] Y.-J. Lin, A. R. Perry, R. L. Compton, I. B. Spielman and J. V. Porto, 'Rapid production of Bose-Einstein condensates in a combined magnetic and optical potential', Phys. Rev. A **79**, 063631 (2009).

[133] A. Farolfi, D. Trypogeorgos, G. Colzi, E. Fava, G. Lamporesi and G. Ferrari, 'Design and characterization of a compact magnetic shield for ultracold atomic gas experiments', Rev. Sci. Instrum. **90**, 115114 (2019).

[134] X.-T. Xu, Z.-Y. Wang, R.-H. Jiao, C.-R. Yi, W. Sun and S. Chen, 'Ultra-low noise magnetic field for quantum gases', Rev. Sci. Instrum. **90**, 054708 (2019).

[135] K. Shibata, A. Torii, H. Shibayama, Y. Eto, H. Saito and T. Hirano, 'Interaction modulation in a long-lived Bose-Einstein condensate by rf coupling', Phys. Rev. A **99**, 013622 (2019).

[136] R. Thomas and N. Kjærgaard, 'A digital feedback controller for stabilizing large electric currents to the ppm level for Feshbach resonance studies', Rev. Sci. Instrum. **91**, 034705 (2020).

[137] J. Appel, A. MacRae and A. I. Lvovsky, 'A versatile digital GHz phase lock for external cavity diode lasers', Meas. Sci. Technol. **20**, 055302 (2009).

[138] J. J. Thuesen, 'Konstruktion af en Raman laser', B.S. Thesis (Aarhus University, 2017).

[139] R. M. F. Andersen, 'Progress report', Progress report (Aarhus University, Feb. 2024).

[140] K. T. Skalmstang, 'Microwave transitions of Rb-87 hyperfine structure through Direct Digital Synthesis', B.S. Thesis (Aarhus University, 2014).

[141] M. L. F. Baron, 'Dynamic radio-frequency sources for atomic state preparation', MA thesis (Gottfried Wilhelm Leibniz University of Hannover, 2022).